



Fused Silica Ion Trap Chip

**Philippe Bado
TRANSLUME INC ANN ARBOR MI**

**01/22/2015
Final Report**

DISTRIBUTION A: Distribution approved for public release.

**Air Force Research Laboratory
AF Office Of Scientific Research (AFOSR)/ RTB
Arlington, Virginia 22203
Air Force Materiel Command**

REPORT DOCUMENTATION PAGE

*Form Approved
OMB No. 0704-0188*

The public reporting burden for this collection of information is estimated to average 1 hour per response, including the time for reviewing instructions, searching existing data sources, gathering and maintaining the data needed, and completing and reviewing the collection of information. Send comments regarding this burden estimate or any other aspect of this collection of information, including suggestions for reducing the burden, to the Department of Defense, Executive Services and Communications Directorate (0704-0188). Respondents should be aware that notwithstanding any other provision of law, no person shall be subject to any penalty for failing to comply with a collection of information if it does not display a currently valid OMB control number.

PLEASE DO NOT RETURN YOUR FORM TO THE ABOVE ORGANIZATION.

1. REPORT DATE (DD-MM-YYYY) 01-12-2015		2. REPORT TYPE Final		3. DATES COVERED (From - To) 09-01-2012 to 08-31-2014	
4. TITLE AND SUBTITLE "Fused silica ion trap chip with efficient optical collection system for timekeeping, sensing, and emulation"				5a. CONTRACT NUMBER FA9550-12-C-0074	
				5b. GRANT NUMBER	
				5c. PROGRAM ELEMENT NUMBER	
				5d. PROJECT NUMBER	
				5e. TASK NUMBER	
6. AUTHOR(S) Dr. Philippe Bado 734.528.6330 pbado@translume.com				5f. WORK UNIT NUMBER	
7. PERFORMING ORGANIZATION NAME(S) AND ADDRESS(ES) Translume, Inc. 655 Phoenix Drive Ann Arbor, MI 48108				8. PERFORMING ORGANIZATION REPORT NUMBER	
9. SPONSORING/MONITORING AGENCY NAME(S) AND ADDRESS(ES) USAF, AFRL AF Office of Scientific Research 875 N. Randolph Street. Room 3112 Arlington VA 22203				10. SPONSOR/MONITOR'S ACRONYM(S) USAF/AFRL	
				11. SPONSOR/MONITOR'S REPORT NUMBER(S)	
12. DISTRIBUTION/AVAILABILITY STATEMENT Unlimited Distribution					
13. SUPPLEMENTARY NOTES					
14. ABSTRACT The objective of this program was to demonstrate a cost-effective, scalable, rapid manufacturing system to produce advanced semi-custom and custom atom/ion chips for the scientific and defense communities. Specifically, we fabricated three-dimensional ion microtraps whereby the ion trap platform and the optical interface platform are integrated within a single glass substrate. The integration of optics with a chip trap pursued in this program has the potential to critically transform the use of ion traps for the collection of atomic fluorescence for motion/force sensors through Doppler velocimetry; and for the efficient collection of single photons from trapped ions for applications in fast single photon sources, quantum repeater circuitry, and high fidelity remote entanglement of atoms for quantum information protocols. We delivered to our academic partners, several three-dimensional ion microtraps of a type, geometry, and capability not previously available in a small form factor. Oblate Paul microtraps that will be used for the creation of two-dimensional coulomb crystals of ions for quantum simulations were fabricated for UCLA					
15. SUBJECT TERMS Ion trap, atom chip, optical interface, Paul trap, Penning trap, electrodes, three-dimensional electromagnetic trap, fused silica micro-machining, quantum sensing, quantum computing					
16. SECURITY CLASSIFICATION OF:			17. LIMITATION OF ABSTRACT	18. NUMBER OF PAGES	19a. NAME OF RESPONSIBLE PERSON Sharon Stemple
a. REPORT U	b. ABSTRACT U	c. THIS PAGE U			19b. TELEPHONE NUMBER (Include area code) 734.528.6371

Fused silica ion trap chip with efficient optical collection system for timekeeping, sensing, and emulation

Dr. Philippe Bado

**Translume, Inc.
655 Phoenix Drive
Ann Arbor, MI, 48108**

5 January 2015

Final Technical Report

Table of Contents

1. Introduction.....	4
Team	4
Program Objectives.....	4
Summary Program Achievement.....	4
2. Methods, Assumptions, and Procedures	7
Microtraps: Material Selection and Platform Fabrication	8
Microtraps: Electrode Design and Fabrication	11
A. Patterning 3-D Electrodes with 3-D Masks	11
B. Electrode Formation by Laser-Ablation	12
C. Creating 3-D Electrodes Using In-Substrate High-Aspect Features.....	14
Electrode Fabrication: Material Selection	16
Electrodes: Metal Deposition.....	17
Trap Metallization and Electrode Patterning	19
Fabrication of Optical Ports and Access Ports.....	28
Fabrication of Ancillary Sub-Systems	33
3. Future Works	35
4. Literature Cited	36
5. Appendixes	37
Appendix A: Summary of ion trap simulations based on Translume’s ion trap platforms	38
Introduction.....	38
Simulation Model.....	38
Comparing Two Trap Platform Geometries	39
The Effect of In-plane Optical Access Port(s).....	44
Symmetrical Ports.....	45
Appendix B: Creation of two-dimensional coulomb crystals of ions in oblate Paul traps for quantum simulations.....	47

List of Figures

<u>Figure 1:</u>	3D Micro Paul Trap	5
<u>Figure 2:</u>	FemtoEtch Process	9
<u>Figure 3:</u>	Platform support for an oblate disc RF trap	9
<u>Figure 4:</u>	Array of beveled slot traps with support features for optical components	10
<u>Figure 5:</u>	Support platform for a Penning trap	10
<u>Figure 6:</u>	Fabricating 3-D electrodes using 3-D mask	12
<u>Figure 7:</u>	Formation of electrodes using laser ablation	12
<u>Figure 8:</u>	Three-dimensional ion micro-trap with laser-defined electrodes	13
<u>Figure 9:</u>	Cleaning laser-defined electrodes	13
<u>Figure 10:</u>	A partial view of a 3-D RF Paul trap	14
<u>Figure 11:</u>	Comparing evaporation to sputtering	14
<u>Figure 12:</u>	Fabrication of electrodes using undercuts	15
<u>Figure 13:</u>	Penning microtrap with a cylindrical geometry	16
<u>Figure 14:</u>	Electroplating	19
<u>Figure 15:</u>	Formation of electrodes in electroplated platforms using laser ablation	21
<u>Figure 16:</u>	Microscope images of the top surface of a microtrap with electrical vias	23
<u>Figure 17:</u>	Examples of oblate Paul traps fabricated in this work	25
<u>Figure 18:</u>	RF feedthrough structures with varying tunnel dimensions, shown prior to electroplating	26
<u>Figure 19:</u>	Test piece with three RF feedthrough structures shown after partial electroplating	27
<u>Figure 20:</u>	Test piece with three RF feedthrough structures shown after full electroplating	27
<u>Figure 21:</u>	Electroplating boundary migration	27
<u>Figure 22:</u>	Collecting optical signal from surface microtrap can be challenging	28
<u>Figure 23:</u>	A Paul microtrap with seven integrated sub-surface ports	29
<u>Figure 24:</u>	A 3D Paul trap in the UCLA experimental UHV chamber	30
<u>Figure 25:</u>	3D trap with integrated optics	32
<u>Figure 26:</u>	Linear Paul Trap	33
<u>Figure 27:</u>	Integration of an electron source with a microtrap	34

List of Tables

<u>Table A:</u>	Physical material properties relevant to atom chip fabrication	8
<u>Table B:</u>	Machining properties for common trap platform materials	8
<u>Table C:</u>	Metals commonly used to fabricate trap electrodes	16
<u>Table D:</u>	Table D: Breakdown test results	20

Cumulative list of people involved in and publications stemming from the research effort

Personnel

Translume:

- Dr. Philippe Bado (PI)
- Dr. Mark Dugan
- Mr. Chris Schenck

University of Maryland, Joint Quantum Institute:

- Professor Chris Monroe

University of California at Los Angeles, Dept. Physics and Astronomy

- Professor Wesley Campbell
- Mr. Danilo Dadic
- Dr. Sylvi Haendel

Publication

- B. Yoshimura, M. Stork, D. Dadic, W. C. Campbell and J. K. Freericks “Creation of two-dimensional coulomb crystals of ions in oblate Paul traps for quantum simulations”, ArXiv 1406.5545 (2014).

1. Introduction

Team

This Phase II is a collaboration between Translume, Inc. (Ann Arbor, MI), Professor Chris Monroe, and Professor Wes Campbell. Professor Chris Monroe holds the Zorn Chair of Physics at the University of Maryland as a Full Professor. He is a Fellow in the Joint Quantum Institute (JQI). Professor Wes Campbell joined the University of California Los Angeles (UCLA) Physics and Astronomy Department in 2013.

Program Objectives

For some time it has been recognized that atomic ions held in radio frequency electromagnetic traps are one of the more promising physical systems for large-scale quantum information processing, and for ultra-sensitive quantum metrology. In order to take advantage of these opportunities, many in the community postulated that one needed to develop scalable means to fabricate high-quality ion traps with an integrated optical interface. The two objectives of our program addressed this requirement.

Our first objective was to develop a compact, chip-based system capable of producing and optically manipulating ultracold ions. Specifically, we intended to fabricate an elementary quantum processing unit (QPU), whereby the ion trap platform and the optical interface platform are integrated within a single glass substrate. Such a QPU, solely or through a scalable multi-unit scheme, will provide the foundation for chip-based devices for quantum metrology, quantum sensing, and applications in quantum information science. The integration of optics with a chip trap pursued in this program has the potential to critically transform the use of ion traps for the collection of atomic fluorescence for motion/force sensors through Doppler velocimetry; and for the efficient collection of single photons from trapped ions for applications in fast single photon sources, quantum repeater circuitry, and high fidelity remote entanglement of atoms for quantum information protocols.

Our second objective was to demonstrate a cost-effective, scalable, rapid manufacturing system to produce advanced semi-custom and custom atom/ion chips for the scientific and defense communities.

Summary Program Achievement

We successfully accomplished the Phase II objectives delivering to our academic partners, several three-dimensional ion microtraps of a type, geometry, and capability not previously available in a small form factor. Specifically oblate Paul microtraps that will be used for the creation of two-dimensional coulomb crystals of ions for quantum simulations were fabricated for UCLA

Numerous enhancements to the trap micro-fabrication process and component integration were uncovered and qualified during this work. While starting this program with a solid glass micromachining technology base, we had very limited metal coating experience. Obtaining the relevant know-how was a crucial part of this program and an essential requirement to fabricate micro-traps. Over the course of this program various standard metal deposition techniques were

unconventionally implemented in order to develop a capability for fabricating complex three-dimensional micro-electrodes.

This capability to fabricate three-dimensional electrodes on 3D platform is prominently featured in some of the trap platforms delivered to our UCLA partners (See Figure 1).

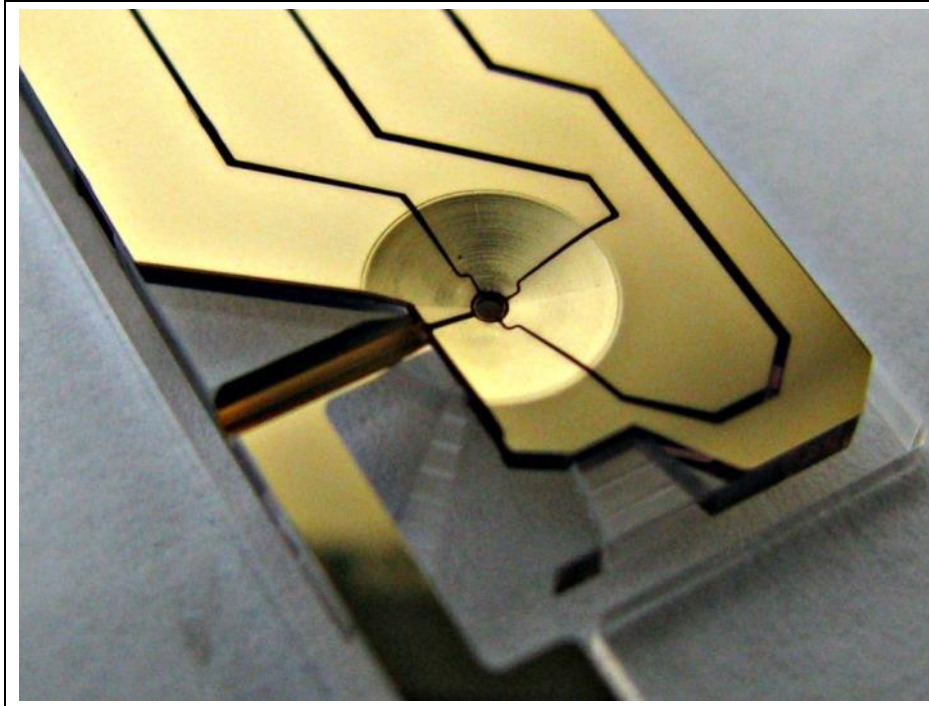


Figure 1: 3D Micro Paul Trap. A micro Paul trap designed by the Campbell group and fabricated by Translume.

This 3D trap, built from a fused silica slab, incorporates seven sub-surface access ports, including several optical ports, a RF feed tunnel (seen at 8 o'clock), and an ion-loading port (5 o'clock).

The 3D electrodes (RF and DC) are fabricated using a combination of mask and laser-ablation. The central bore has a 0.5-mm diameter.

As part of this program we demonstrated a cost-effective, scalable, rapid manufacturing system to produce advanced semi-custom and custom atom/ion chips for the scientific and defense communities. In many ways, this may well be where AFOSR get the largest “return on investment” associated with this program. As a result of the development pursued during this Phase II STTR program, Translume now has revenues generated from commercial activities associated with the fabrication of microtraps (including revenues from overseas). Albeit commercial revenues are presently modest, they will undoubtedly grow and will ultimately provide a significant return on the investment made by AFOSR. In parallel with this program, using fabrication processes (partially) developed during this STTR, we have fabricated traps for the in-situ coating and testing by the Haeffner group (UC Berkeley, CA), as well as for the University of Mainz (Germany) and the University of Innsbruck (Austria). We also had microtrap fabrication discussions with several members of the Wineland group (Boulder, CO), and discussed electron accelerators microfabrication using Translume capability with Dr. Peter Homelhoff (Max Planck Institute of Quantum Optics, Garching, Germany). We are discussing Penning microtrap designs and fabrication activities with a European group working at the FAIR facility in Germany.

The technology and knowledge acquire in this AFOSR-funded program was also essential in obtaining a Department of Energy grant to demonstrate the fabrication of a high-precision magnetometer designed to operate in high-radiation environments. This magnetometer is based on a Penning microtrap. It is being develop in collaboration with the group of Dr. Georg Bollen and will be tested at the Facility for Rare Isotope Beam (FRIB) located on the Michigan State University (MSU) campus. Ultimately, it will be used to continuously monitor the various

magnets used to control the FRIB beamline. (Presently NMR probes are providing this function. However, their lifetime is very limited in the high radiation environment of the beamlines.) Development of such a magnetic field probe represents a significant milestone in term of technology deployment: This microtrap based device will not be used as an academic research instrument; rather it is designed to operate as a sensor providing an essential function, and expected to be deployed at numerous scientific, industrial, and medical facilities.

Thus, it is reasonable to say that our fabrication capability is generating growing interest from the ion trapping community, serving a need that is not otherwise addressed. This said there is still a long way to go before Translume microfabrication capability is valued beyond a few (world-known) research groups. We need to pursue development of trap platforms with significantly more capabilities. This is discussed in some details below.

2. Methods, Assumptions, and Procedures

During the course of this STTR Phase II program we developed a significant capability to fabricate small-scale ion traps made from fused silica blanks.

For over half-a-century, electromagnetic traps have been used to study charged and neutral particles in a setting where they are shielded from unwanted perturbations. Such traps permit the observation, manipulation, or storage of isolated particles or small groups of particles over long time periods, a feat that was not possible before their invention. Numerous ion trap geometries have been proposed and demonstrated. The Penning trap and the Paul trap are two of the most frequently used designs, although other trap designs are often preferred in applications, such as mass spectrometry.

It has been proposed that these types of traps be used as the foundation for various ultra-sensitive sensors. However, with very few exceptions this vision has yet to be achieved: Most ions and neutral particle traps are physically quite bulky. They are designed to operate inside large ultra-high vacuum (UHV) vessels, which are difficult to operate and extremely expensive. To operate these traps necessitate complex optical systems, which are used to manipulate and monitor the trapped particles. Precise positioning is required between the various optical components (lasers, modulators, photo-detectors, *etc.*) that are outside the evacuated chamber and the trap, which is located inside the chamber. This arrangement is susceptible to misalignment.

As a result, the use of such traps is limited. Since the 1990's, there has been a broad-based effort to eliminate these shortcomings, developing what is referred to as "microchip-scale trap" or simply "microchip trap". The fabrication of these microchip traps is typically based on photolithographic techniques. Critical features, such as electrodes, range in size from one hundred nanometers to tens of microns. Due to the fabrication process, these microchip traps typically have a planar geometry. The trapped species (ions or neutral atoms) are suspended a few microns to a few tens of microns above the surface of the trap electrode substrate in relatively shallow traps (small difference between local field extremes). This situation is in sharp contrast to experimental 3D devices where the trapped particles are generally found, not above, but rather between the electrode surfaces in comparatively deeper trapping potentials. While these 2D microchip-scale traps have simplified the electromagnetic part of the trapping process, they have done little to simplify the optical addressing (*i.e.* cooling, encoding, and read out).

For many applications, non-planar (*i.e.* three dimensional) microtraps may provide significant benefits over planar microtraps (deeper trapping potential, much easier optical access, reduced sensitivity to surface defects, *etc.*). During the course of this program, we developed processes to fabricate three-dimensional microtraps.

In the following sections, a review of the method, assumption, and procedures used to fabricate these three-dimensional microtraps is presented. More specific consideration is given to:

- a) Fabrication of fused silica trap platforms
- b) Three-dimensional electrodes fabrication
- c) Fabrication of optical and access ports
- d) Design, Fabrication and Integration of ancillary sub-systems

Microtraps: Material Selection and Platform Fabrication

Our microtrap platform fabrication is based on processes developed over the last decade at Translume. Basically, a combination of material patterning with femtosecond laser pulses and wet etching is used to precision machine microtrap bodies from fused silica glass substrates.

Fused silica is used as the foundation material having characteristics that are generally considered highly desirable for microtraps (See Table A).

Fused silica is an extremely good electrical insulator, well into the microwave. It has a dielectric loss factor of under 0.0004 at 1 MHz. Fused silica is also an excellent optical material that is transparent from the UV to the mid-infrared. It has virtually no self-fluorescence.

Fused silica has a near-zero coefficient of thermal expansion (0.55 ppm/°C over the 20-320°C range), which accounts for its remarkable ability to undergo large, rapid temperature changes without cracking, and to provide the basis for the fabrication of mechanically-stable interferometric platforms.

Fused silica is also an extremely inert material compatible with materials used in typical ion trap applications (Alkali ions for example). Moreover, fused silica has excellent elastic properties making it a desirable material for micro-mechanical components (this is one of its less well-known characteristics).

Until recently it was difficult to precision machine fused silica (See Table B). While the microelectronics industry had developed various means to structure thin-film of SiO₂, these processes do not provide much in term of high-aspect 3D machining.

However this situation has been changing: Over the last decade Translume has developed direct-write processes to (i) locally change the index of refraction of fused silica, and (ii) locally enhance the chemical susceptibility of fused silica to various liquid etchants (chemical

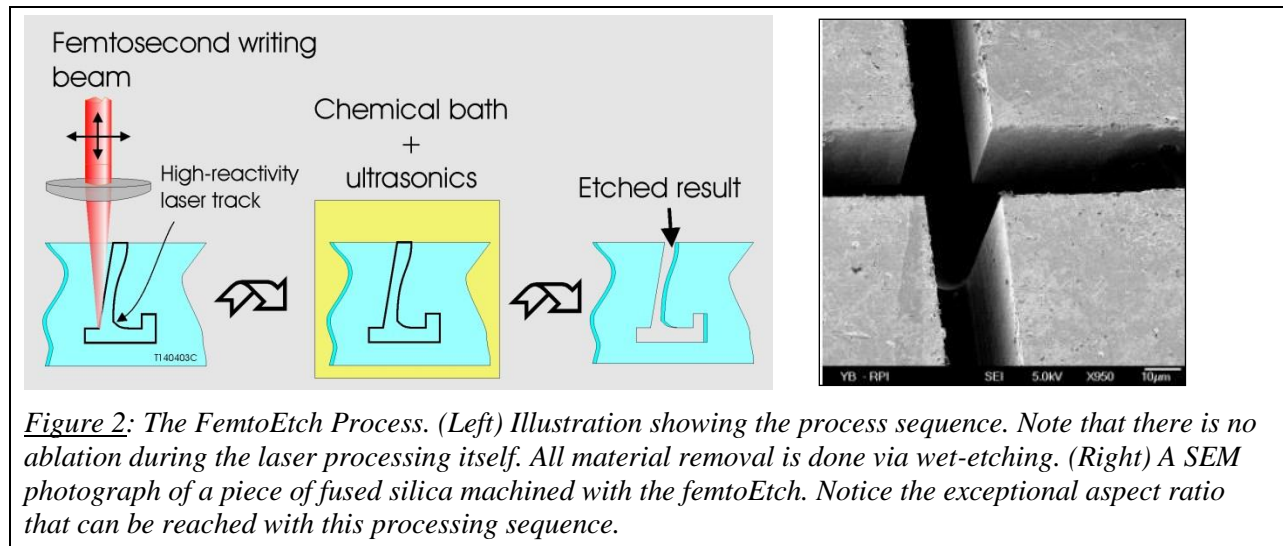
etching rates can be increase one-hundred-fold over that of unaltered fused silica). The former process (*femtoWrite*TM) is used to create sub-surface optical waveguides; the latter process (*femtoEtch*TM) is used to micromachine complex three-dimensional structures (See Figure 2). Note that there is no laser ablation involved in *femtoEtch*. Rather the material is laser-activated and then chemically etched away.

We have used the index change process to fabricate, among other devices, monolithic optical interferometric waveguided array sensors that were delivered to the Air Force. We have used the chemical susceptibility process to produce scores of devices, including microfluidic flow cells

<i>Table A: Physical material properties relevant to atom chip fabrication for common trap platform materials</i>				
Material / Features	Silicon	Alumina (ceramic)	Sapphire	Fused Silica
Transparency (visible)	No	No	Excellent	Excellent
Transparency UV	No	No	Good	Excellent
Dielectric loss factor	Good	Excellent	Excellent	Excellent

<i>Table B: Machining properties for common trap platform materials</i>				
Material / Machining	Silicon	Alumina (ceramic)	Sapphire	Fused Silica
2D precision micromachining	Outstanding	Limited	Limited	Good
3D precision micromachining	Limited	Limited	Limited	Good

used onboard the International Space Station; and of course the microtraps that were fabricated as part of this program.



Judiciously combining laser-modified and unmodified zones, one can fabricate high-aspect three-dimensional small structures from fused silica blanks using these unconventional fabrication processes. Utilizing inherent alignment registration within the substrate, precision-machined platforms can be fabricated to support numerous functionalities including optical subsystems (through direct waveguides or structures for micro-optic component and fiber positioning), electrical pathways (through sub-surface routing between the 3D electrode surfaces and their individual lead access), sample loading (through micro channel featuring), *etc.* The typical size scale (a few microns to a few centimeters) associated with our fabrication processes is appropriate for most ion chip applications. Three examples of trap platforms that exemplify this microfabrication capability are shown below.

Figure 3 shows a platform support for an oblate disc RF trap fabricated during the course of this program for the Wes Campbell group. Eight in-plane ports are seen leading to the center trap bore. The seven through-ports with openings on the platform edge are used for free space optical access. Two of them have dual roles: The one leading directly off to the left will support the RF lead electrode to the center ring, and the asymmetrical tapered hole leading off the bottom platform edge will also be used to load the trap with the neutral atoms for ionization.

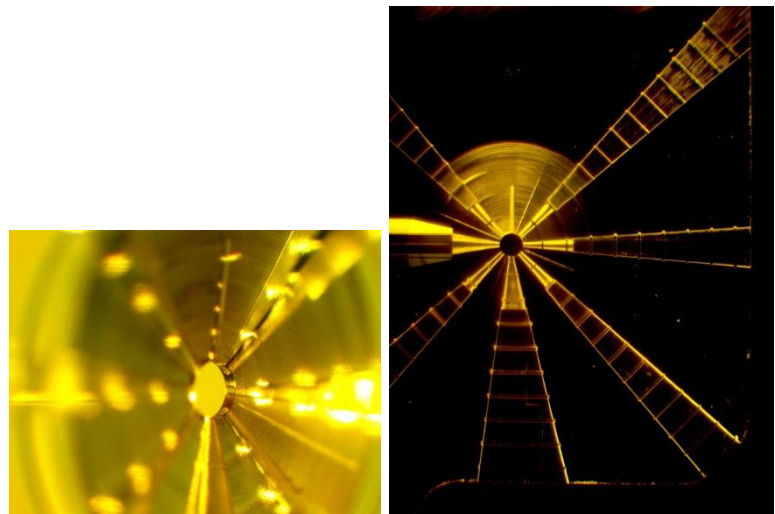


Figure 3: Platform support for an oblate disc RF trap (Shown prior to coating)

Directly across the center bore from this port is a blind hole used to collect the non-trapped atoms/ions.

Figure 4 shows another 3D trap platform fabricated during the course of this program. This platform structure consists of an array of beveled slot traps with support features for optical components. Apposing structures consisting of optical fiber holes, recessed cavities for micro-lenses, and large-angle tapered access hole to the trap center can be seen. Not obvious in the image are glue/epoxy ports for component attachment.

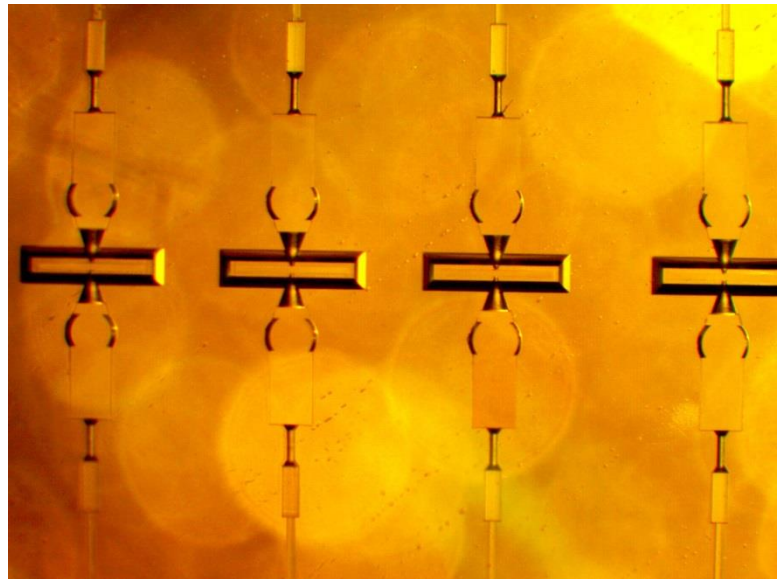


Figure 4: Array of beveled slot traps with support features for optical components

Figure 5 shows a support platform for a Penning trap fabricated for a different project but included here because it

demonstrates an electrode fabrication approach developed, in part, through the work supported in this Phase II STTR. In this structure a center cylindrical bore (1mm diameter and 1mm deep) is segmented into eleven separated (with 25 μm to 50 μm gaps) surfaces. These surfaces, defining the trap electrodes, are each continuous to a separate recessed channel floor. The three support platforms exemplify the initial elements in the fabrication sequence of 3D trap electrodes and associated ancillary components.

Note that others have recognized the value of fused silica (sometimes called fused quartz, or amorphous quartz) and have pursued the development of advanced traps using photolithographic processes combined with ion milling. For example, Jeffrey Wineland and his coworkers at NIST fabricated a quartz-based ion trap which is a planar version (surface-electrode trap) of a radio-frequency (RF) Paul trap.¹

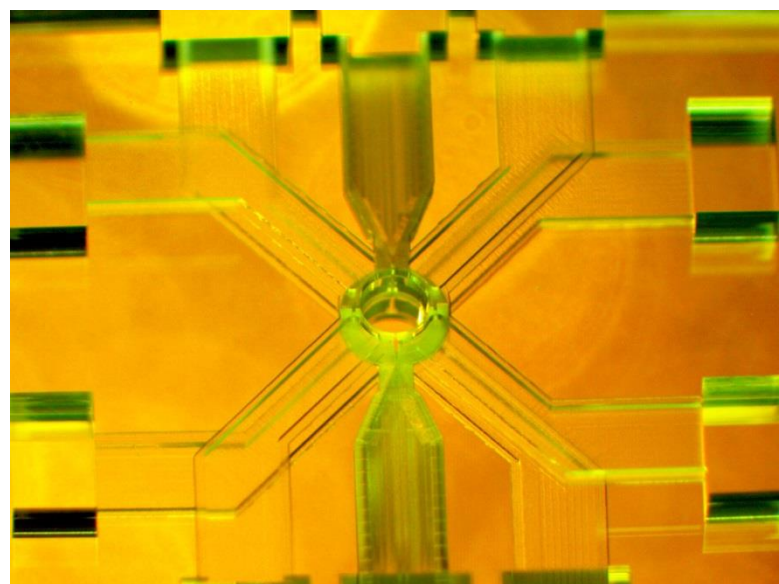


Figure 5: Support platform for a Penning trap

Microtraps: Electrode Design and Fabrication

Electrodes are an essential element of all atom and ion traps. Used primarily to confine and position the particles, electrodes can be configured in certain trap designs as voltage controlled gates and sensing elements to monitor the motion of trapped particles. Electrodes are also arranged to define a ground reference, and to cover dielectric surfaces preventing unwanted charge build-up.

It should be recognized that a trap's ability to perform its function is defined primarily by the electrode design, and ultimately, by the electrode fabrication processes (with their associated limitations). Material properties also need to be taken into consideration.

The ability to contour and section electrode surfaces over small dimensions allow for tailoring of larger field gradients (even at relatively low supply voltages). Furthermore, utilization of all three dimensions enhances the functional integration of multiple interrogation modalities, sample input, and environmental access.

Several mature techniques are available to fabricate planar (2-D) electrodes on small ion and atom trap platforms. For example, well-established photolithographic processes are routinely used to produce complex electrodes patterns on flat surfaces, including some with sub-micron features.

Fabricating 3-D electrodes on small trap platforms is, by far, more challenging. The micro-electronics industry has been struggling for years trying to develop processes to mass-produce 3-D structures in general. This effort is still on-going.

Several research groups have demonstrated photolithographic-based approaches that provide a limited three-dimensional fabrication capability. These techniques (sometimes referred to as “two and a half dimensional”) are incapable of producing the deep (*i.e.* high depth-to-width aspect ratio) three-dimensional geometries required for many trap applications. In contrast, we have pursued another path, and during the course of this program have developed several unconventional procedures for the manufacturing of complex 3-D electrode geometries on fused silica substrates. Common to all our approaches, the fused silica substrate is first shaped via our *femtoEtch* process into a 3-D platform defining the electrode surfaces and other possible functions (e.g. electrical lead access, sample loading, and optical ports). Depending on the platform design, the surfaces to be coated may have a range of orientations relative to a coating axis, and therefore, require an angularly distributed initial coating technique (e.g. sputter coating or angled evaporative coating with sample rotation). Discussed below are three approaches used at Translume to fabricate 3-D electrodes, pointing out their applicability range and their respective attributes.

A. Patterning 3-D Electrodes with 3-D Masks

Metal coating through a planar stencil mask to pattern 2-D electrodes on flat surfaces has been extensively used. For 3-D structures, however, sputter coating through such masks results in poorly define electrode boundaries in the areas where a gap is present between the 3-D platform surfaces and the planar mask. The mask ability to control the metal deposition is strongly affected by this gap, resulting in a tapered and diffuse coating boundary that makes electrode positioning difficult.

We have extended this stencil mask approach to the coating of electrodes on contoured recessed surfaces through the use of 3-D stencil-type masks made from fused silica (See Figure 6). These

stencil masks are fabricated with the same *femtoEtch* processes used to produce the trap platform. Having a shaped body complimentary to that of the platform, the mask features (shaped slits, through holes, *etc.*), through which the metal atomic flux transits, are extended down to the platform surface. Depending on the thickness of the mask substrate, the aspect ratio of these through features can be changed with depth to either reduce or pass the maximum angular spread of the coating beam along selected axis. Stencil masks can be used multiple times and provide a cost-effective way to pattern electrodes. There are some limitations associated with the geometry of the 3-D openings: Their minimum width is dependent on the thickness of the mask substrate and can be limited to several microns or larger. Further, if the surfaces to be coated are strongly angled relative to the metal source-substrate path and the mask features are of high aspect ratio, the deposition will be diminished and this may result in an overly thin coating.

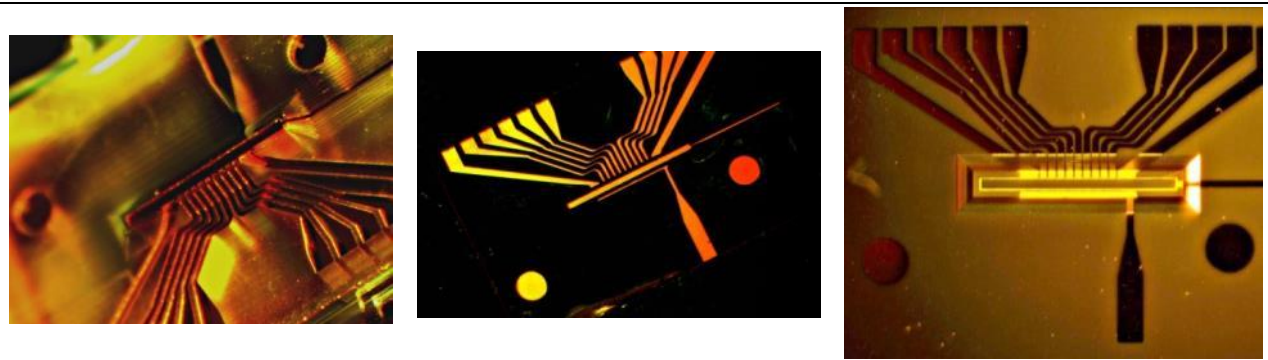


Figure 6: Fabricating 3-D electrodes using 3-D mask. (Left) 3-D stencil mask fabricated in fused silica using our femtoEtch process. (Center) 3-D stencil mask mated to 3-D substrate - shown after gold sputtering. (Right) The resulting three-dimensional ion trap with 3-D RF and DC electrodes, shown after mask removal.

Offering limited alignment precision in comparison to our other electrode fabrication approaches, coating through a 3-D mask can be used in conjunction with these complementary procedures for establishing a relatively coarse pattern metal coverage. This approach is compatible with all metals commonly used to fabricate electrodes.

B. Electrode Formation by Laser-Ablation

Electrode patterns can also be written directly into previously coated surfaces through direct-write femtosecond laser ablation (See Figure 7). The electrode boundary gaps can be formed by focusing the writing laser from either the coated side of the surface or through the transparent silica body, offering flexibility in accessing 3-D surfaces.

Note that this direct-write process is compatible with both flat and non-flat surfaces; it can be used directly with

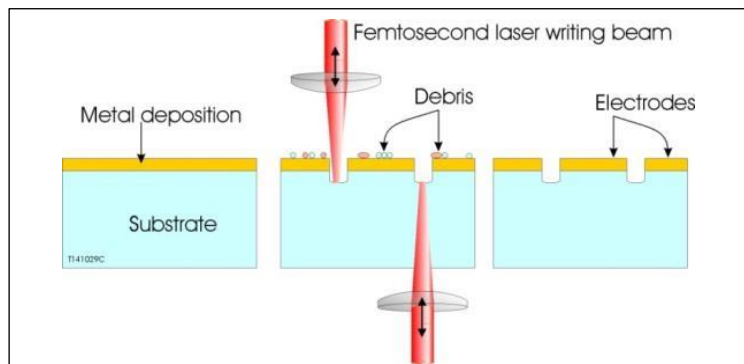
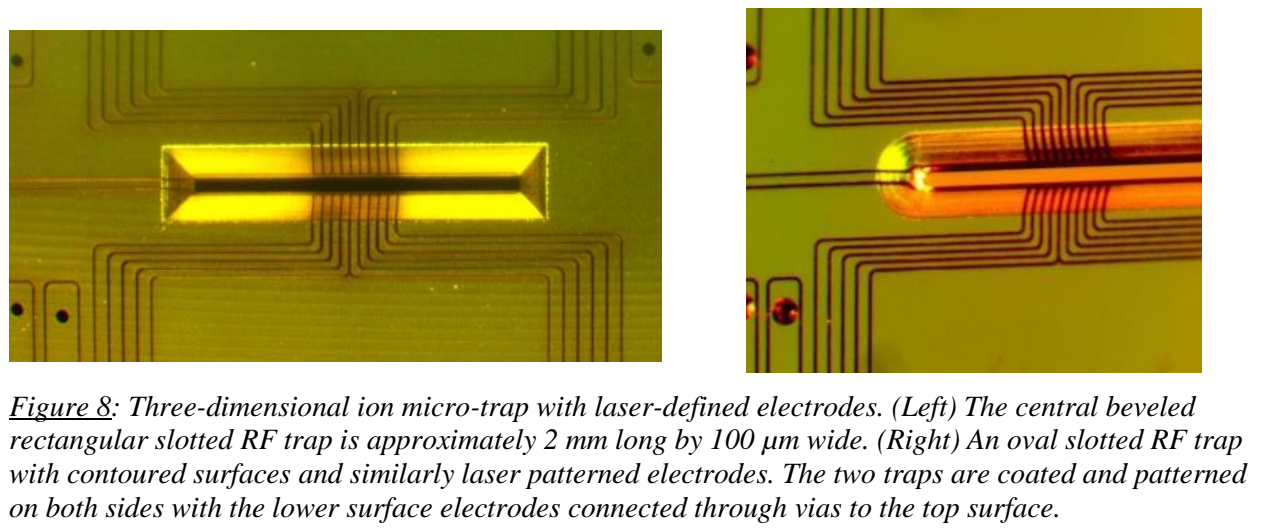
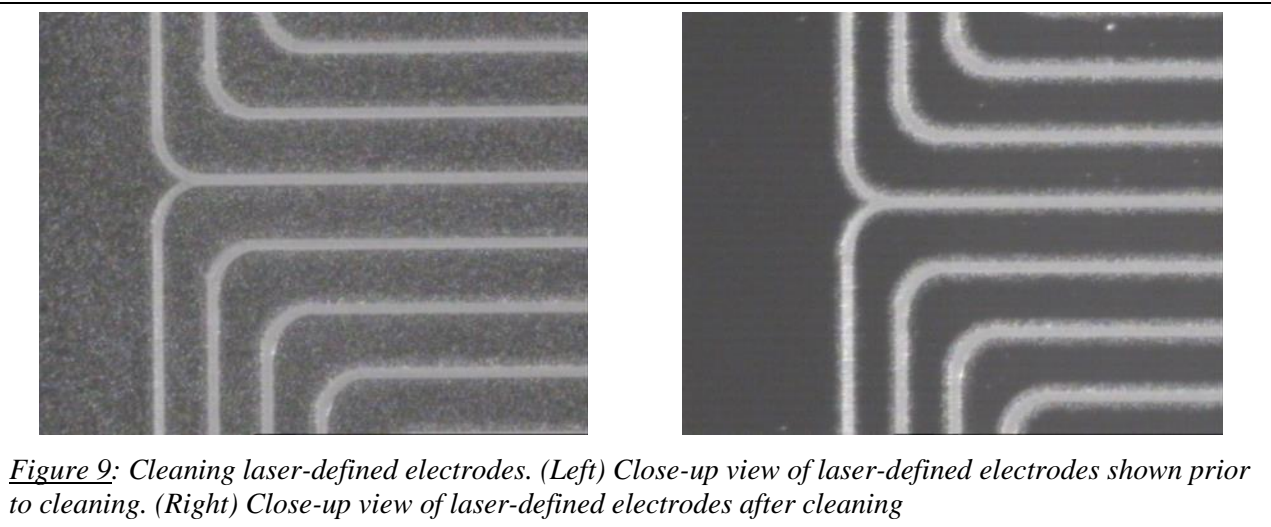


Figure 7: Formation of electrodes using laser ablation. (Left) Metal deposition (Center) Electrodes defined through laser ablation. (Right) Post-processing cleaning

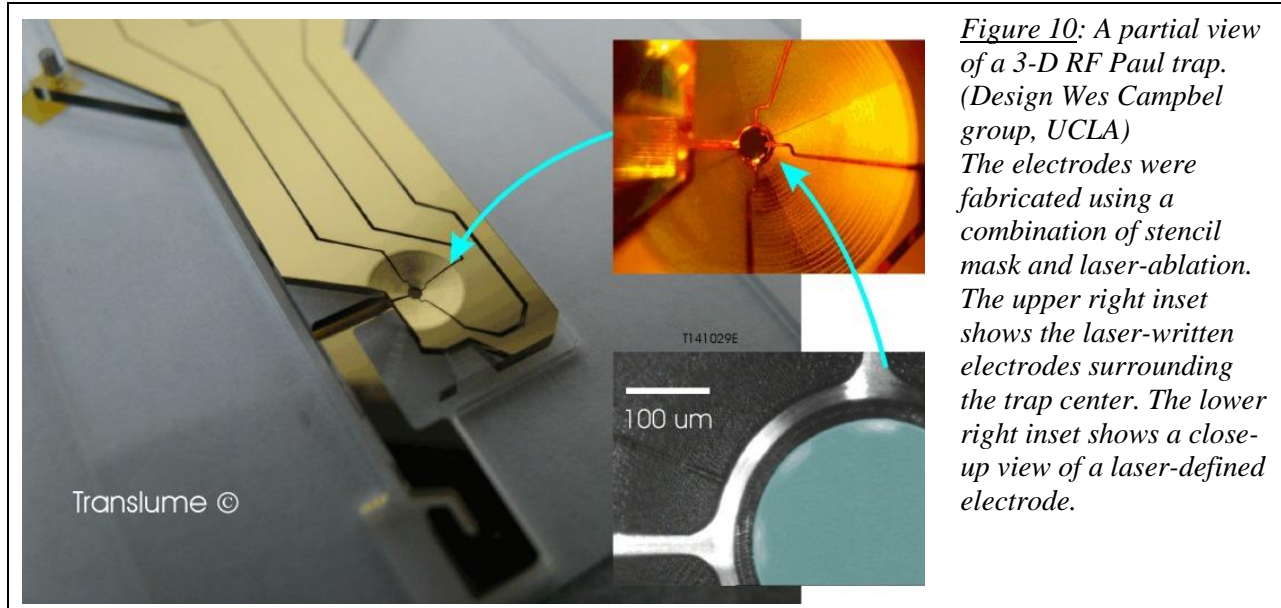
surfaces that are contoured (See Figure 8 and Figure 10). Its applicability to vertical surfaces is limited to geometries that allow for lateral laser access.



While this approach is compatible with all metals commonly used to fabricate electrodes, the associated surface cleaning procedure (See Figure 9) is somewhat metal-specific.

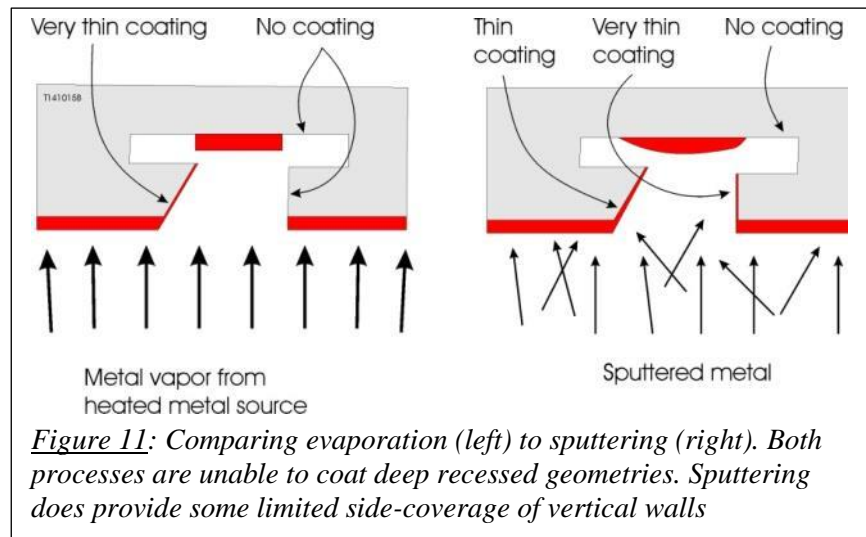


The extensive scattering of ablation debris in the vicinity of the electrode gaps could form trigger points for RF/DC breakdown. However, with the appropriate surface cleaning procedures the voltage threshold for RF/DC breakdown can be significantly increased. Tests on ablative electrodes with gaps ranging from 10 to 30 microns have been shown to withstand RF voltages of several hundred Volts (>850V & 20W RF power).



C. Creating 3-D Electrodes Using In-Substrate High-Aspect Features

Electrode deposition is most often done using an evaporator or a sputter coater. These tools work best when coating flat surfaces that are held approximately perpendicular to the source-substrate path. Surfaces that are angled from perpendicular and even, depending on the aspect ratio, parallel surfaces to the coating axis can be covered uniformly albeit with a thinner coating (See Figure 11).



Surfaces whose view of the metal source-substrate path is obstructed (recessed cavities for example) will not be coated by an evaporator, and will be, at most, marginally coated through sputtering. Open-through structures have the advantage of coating from both top and bottom side, which will result in a more uniform coverage.

While this deposition physics is often restrictive, it can be used to form electrodes: High-precision 3-D electrode patterns can be generated by machining high aspect slots and undercuts into the silica during the trap platform manufacturing. When placed judiciously, these recessed elements form isolated electrode boundaries after evaporative or sputter metal coating. The

undercuts can be simple straight trenches, or can be shaped to provide additional isolation, as shown in Figure 12.

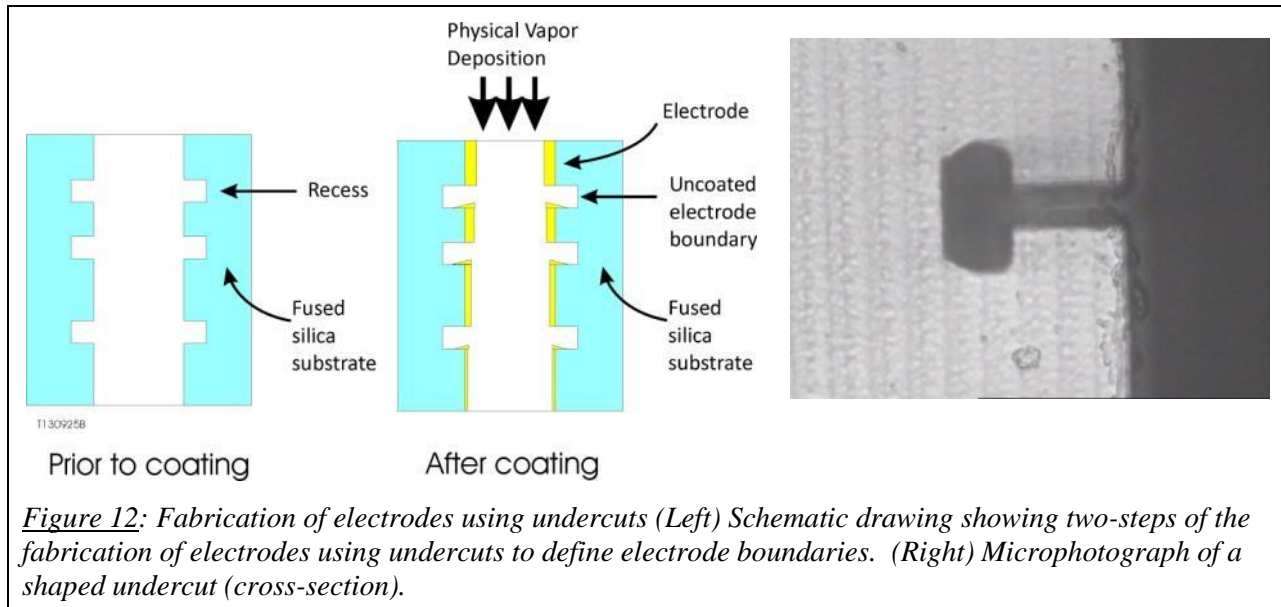


Figure 12: Fabrication of electrodes using undercuts (Left) Schematic drawing showing two-steps of the fabrication of electrodes using undercuts to define electrode boundaries. (Right) Microphotograph of a shaped undercut (cross-section).

This electrode fabrication process is compatible with both surface (2-D) traps and three-dimensional traps. The size (width and height) of the undercuts can be optimized to provide very high-voltage isolation. These undercuts are for the most part air gaps. The uncoated dielectric surface (glass surface) is substantially removed from the working electrode surface, and in fact, can be machined in such a way that there is minimal dielectric surface area with a direct line of site to the trapping volume, thus minimizing the effect of stray fields from surface charge.

Besides laying out the main electrode geometry, high-aspect features fabricated into the silica platform can serve other purposes from routing lead access to tuning the electrical characteristics of the device. With respect to the former feature, electrode leads initially in recessed channels at various depths can be brought to a common surface via vertically tapered channels or holes to an array of wire bonding pads. Alternatively, wire ports through the glass directly to the lead channels can be made to accommodate solder flux or paste for mechanically robust wire attachment.

Secondary structuring of the silica platform can provide further tuning of the electrical characteristics of the final metallized configuration. As an example, stray capacitance can arise from closely spaced surface regions between different electrodes and can be problematic for RF sourcing, or in some ion trap applications, RF resonant detection. The walls of the high aspect slots and undercuts used to establish electrode boundaries through blocking or shadowing of the metal deposition beam can themselves be partially coated establishing capacitance. (This partial surface coating can be quite extensive if a second metallization via electroplating is implemented.) The region of the electrode surface in question, albeit not directly important to the trapping potential geometry, can be minimized by incorporating a secondary transverse slot (*i.e.* normal to the parallel surfaces). Isolation between the working electrode surface and the parallel conductive portions of the electrode gap surfaces will be established where the latter surfaces can be grounded preventing floating potentials. These features were used to configure the electrodes of a small Penning trap (See Figure 13): The secondary transverse isolation slot runs along both sides of the vertical slot just behind the curved electrode surface. These isolation

features were fabricated along all four vertical slots on both quad-sectioned rings. For the Penning trap, the two quad-sectioned rings are used, in part, for ion orbit excitation and image current detection. Therefore, parasitic capacitance potentially becomes problematic. A similar feature was incorporated in the disc RF trap along the RF tunnel port (see below). Such secondary features as well as various primary electrode geometries are readily incorporated into the silica platform fabrication and allow for significantly enhanced design flexibility for 3D electrode patterns.

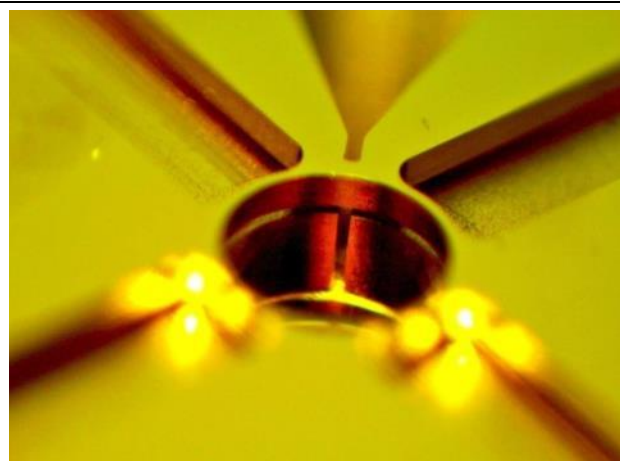


Figure 13: Penning microtrap with a cylindrical geometry. The top end cap, two surfaces of a quad-electrode section, and the center ring electrode are clearly visible in this close-up view.

This demonstrator uses high-aspect features fabricated into the silica platform that are used for routing lead access to the electrodes of interest. The center channel seen at the top of the figure is electrically connected through a low resistance metalized pathway to the corresponding bottom surface channel via the center ring. All inner electrodes and associated lead channels are electrically isolated from one another.

(Figure 5 shows a similar Penning trap platform prior to coating)

Electrode Fabrication: Material Selection

Gold is the most commonly used metal to fabricate ion micro-trap electrodes, but other metals (such as, aluminum, platinum, and copper) may also be used (See Table C). All of these metals are excellent electrical conductors, a material quality that is obviously a pre-requisite for an electrode.

Table C: Metals commonly used to fabricate trap electrodes

Metal	Electrical Resistivity ρ (Ohm m) at 20°C	Electrical Conductivity ρ (Siemens/m) at 20°C
Aluminum	2.82×10^{-8}	3.50×10^7
Chromium	1.25×10^{-7}	8.00×10^6
Copper (annealed)	1.68×10^{-8}	5.96×10^7
Gold	2.44×10^{-8}	4.10×10^7
Nickel	6.99×10^{-8}	1.43×10^7
Platinum	1.06×10^{-7}	9.43×10^6
Silver	1.59×10^{-8}	6.30×10^7
Titanium	4.20×10^{-7}	2.38×10^6

Gold and platinum are extremely inert and will not react when exposed to air or humidity. On the other hand, Aluminum will react immediately with atmospheric oxygen and a very thin (typically 4-nm thickness) oxide layer will form on the exposed surface. This oxide layer protects the base metal from further oxidation. Copper also reacts with atmospheric oxygen, but at a slower speed, and it forms a layer of brown-black copper oxide which protects the

underlying copper from more extensive corrosion. To sum up, both Aluminum and Copper form oxide layers that are electrically non-conductive. Static charges can build up on them, a process that is disruptive to the operation of most traps. Consequently, when fabricating ion traps, one typically selects an electrode material that does not oxidize, Gold being the most common choice. Note that there has been some recent work² where ion micro-traps were metalized in-situ and never exposed to oxygen. Under these conditions, a broader range of metals can be considered for electrode fabrication.

While Gold is an excellent electrical conductor and does not oxidize, it does have a few shortcomings. Gold electrodes are usually thin and soft. As a result, they are subject to damage by scratching; this is likely to occur either during chip handling or during probing. In the microelectronics industry, in order to minimize the scratching, the gold electrodes/leads are often overcoated with a thin layer of a hard material such as SiO₂. This dielectric protection option is undesirable when fabricating ion traps, and therefore, ion trap electrodes are generally not overcoated; they must be handled carefully in order to prevent damage. The ductility of Gold does have a positive side: it helps reduce the internal stress that would normally build-up during the metal deposition process, or when the trap is subjected to temperature changes resulting in coefficient of expansion mismatch (between the metal and the trap substrate).

Due to its chemical inertness, Gold does not adhere very strongly to many materials, including glass. Thus, prior to the formation of an Au electrode layer on a smooth glass substrate, a transition metal film (such as Titanium or Chromium), is usually deposited to strongly bind the glass and the gold together. This thin (tens of nanometers at most, much less in many cases) intermediary layer has a much higher adhesive strength than Gold and binds very well to surfaces such as glass. This intermediary layer also bonds well to Gold.

Gold has an extremely low outgassing rate, it can be baked to 120 °C or more, and it does not react strongly with the alkalis that are commonly used in ion trap experiments.

Electrodes: Metal Deposition

Several techniques are used to form metal electrodes on ion- or atom-trap platforms. In almost all cases, the electrodes are created by first depositing a thin (sub-micron) layer of the desired metal onto the trap platform. This deposition can be done either by evaporation or sputtering. (These processes are collectively referred to as “Physical Vapor Deposition”). If desired, in a subsequent phase, a much thicker metal layer can be formed by electro-deposition.

Evaporation

Vacuum evaporation is carried out at a pressure of 10⁻⁵ Torr or lower. The metal, from which the coating is to be formed, is heated to a sufficiently high temperature to cause it to vaporize at the pressure of the chamber. The substrate to be coated is positioned at some distance from the heated metal source. It is held at a temperature that allows for the condensation of the vaporized metal onto it. The pressure in the vacuum chamber must be sufficiently low for the mean free path of the evaporated atoms to exceed the source-substrate distance; otherwise the metal will tend to nucleate before reaching the substrate, which can produce a rough deposit. If this pressure requirement is observed, excellent films can be formed by this method, which is applicable to most metals (some refractory metals have melting points so high that they may be too difficult to evaporate).

Evaporative coating is highly directional, and therefore works well when coating flat surfaces that are held approximately perpendicular to the source-substrate path. With evaporative deposition, increasingly angled surfaces from perpendicular will have a thinner coating as parallel surfaces will not be coated in any continuous manner. Surfaces whose view of the source-substrate path is obstructed (recessed cavities for example) will not be coated with this evaporative process. The utility of evaporative coating for general 3D electrode structures is very limited. We have found it most useful for coating the floors of deep recessed (width to depth ≤ 0.05) blind holes, or for covering electrode surfaces mildly contoured from the perpendicular orientation. With respect to the latter, a simple straight channel can provide enough of a coating shadow to establish an electrode boundary.²

Sputtering

Sputtering is another physical deposition process commonly used to fabricate electrodes. It too takes place in an evacuated enclosure. Atoms are ejected from a solid metal target by subjecting the target to a flow of energetic positive ions. These ions are generated from a low pressure plasma of inert gas (usually argon). The gas ions are accelerated towards the metal target by a potential of several kilovolts. As the gas ions collide with the metal target, their kinetic energy is transferred to the target, giving sufficient energy for some of its atoms to leave the surface.

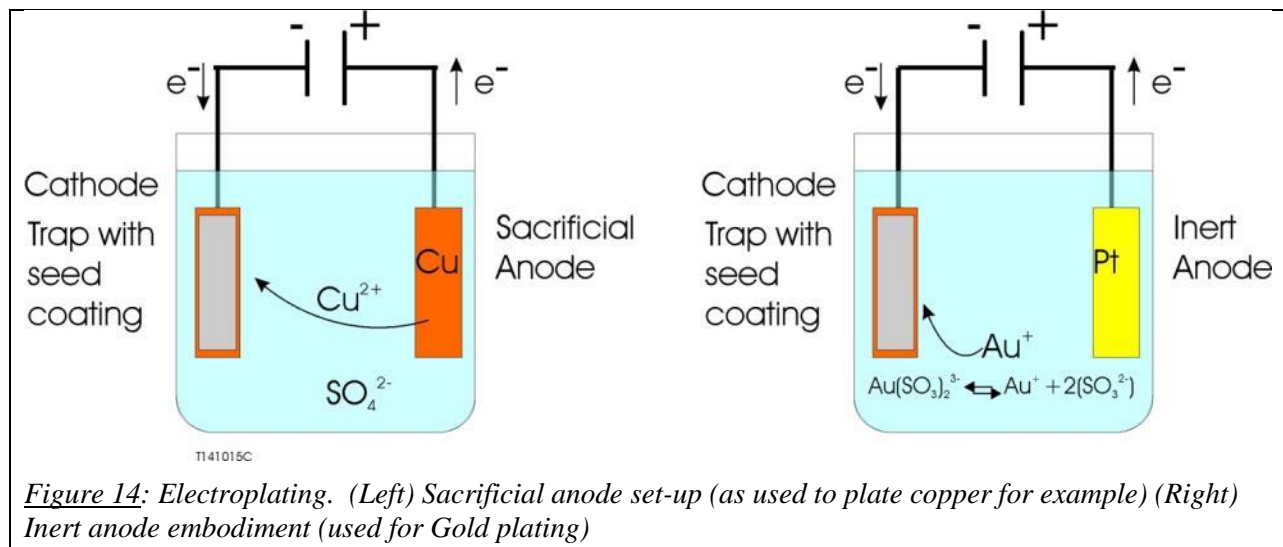
Sputtered atoms ejected into the gas phase deposit on all surfaces in the vacuum chamber. Any substrate placed in the chamber will be coated with a thin film. The sputtered metal atoms have much greater kinetic energy than thermally volatilized atoms, and they can undergo collisions while traveling to the substrate without nucleation occurring. Thus relatively high pressures in the 10^{-3} to 10^{-2} Torr range can be used. As the sputtered atoms arrive at the substrate, with much higher energies than evaporated atoms, the adhesion between this coating and the substrate is often improved. Contaminants, such as water vapor molecules, adsorbed on the substrate surface are displaced by the sputtered atoms, which embed themselves in the surface layer of the substrate. During transit from the metal source to the substrate to be coated, the metal atoms undergo multiple collisions with the gas ions, causing them to stray from a straight path and effect diffusive spreading at the substrate. Consequently sputtering, unlike evaporation, can provide a certain degree of lateral and around corner coating. This effect can be used, for example, to side-coat through-holes, whose length-over-diameter ratio is not too excessive. Typically we would deposit Au on Ti or Cr of normal surface thickness 5000 Å (Au) and 200 Å (Ti or Cr) using a Kurt J. Lesker Lab 18 sputter coater at the University of Michigan Lurie Nanofabrication Facility. Using the facility set sputtering parameters (as we were not permitted to experiment with the instrument) and sputtering on both top and bottom surfaces, we obtained uniform continuous coating of through-hole side walls with depth to width aspect ratio of 3.5:1. For features above this aspect ratio, the resistance between the top and bottom surface, by means of the through hole, significantly increases as the wall coverage loses continuity. Similarly, features (*e.g.* undercuts, port holes, *etc.*) fabricated into the walls of recessed structure will have its lower surface coated to a limited extent underneath an overhang. The coating boundary on such restricted surfaces is not sharp but becomes diffuse and discontinuous. These coating restrictions are incorporated into the design of the silica trap platform. One disadvantage of sputtering, in comparison with thermal evaporation, is that the deposition rate is typically lower. With both evaporation and sputtering, one generally rotates the substrate during deposition, in order to obtain a more even coating. The thickness of the deposited layer is limited by the amount of strain which can be accommodated in the coating.

Electro-deposition

Evaporation and sputtering are best suited to the production of thin coatings, with thickness ranging from a few atomic layers up to a fraction of a micrometer. If a thicker metal layer is desired, it is generally created by electro-deposition (also called electroplating).

The electroplating process is performed in a liquid bath, which contains a conducting solution and two electrodes (see Figure 14). The part to be coated forms one of the two electrodes (the cathode). A differential potential is applied between the two electrodes, which drives the metallic cations towards the cathode, where they accumulate to form a (thick) coating layer. The metallic ions are created from a sacrificial electrode (anode). (In an alternative embodiment, the anode is non-consumable, and the metallic ions are produced from a salt dissolved in the bath.)

Typically the part to be coated (cathode) must be electrically conductive, either naturally or through a previous coating process. However, we have experimented in this project with the electroplating of sputter coated restricted surfaces and have noted extensive migration of the electroplated boundary over the diffuse and disconnected sputter coated borders. A series of short and shallow side tunnels (lengths 0.1mm to 0.4mm) connecting two open recessed cavities or through holes were sputter coated (perpendicular to the tunnel axis) yielding either a high resistance (10's to 100 Ohm) electrode path or two isolated electrodes leading in from each port along the tunnels lower surface and forming a diffuse boundary gap. After electroplating this test structure (to $\sim 3 \mu\text{m}$ thickness measured on open flat surface), the originally high resistance electrodes measured less than 1 ohm resistance and the shorter of the originally open electrode paths showed continuity with a 1.3 Ohm resistance. We are further testing this secondary electroplating process particularly the "border migration" effect and its resulting coating quality.



Trap Metallization and Electrode Patterning

The trap prototypes fabricated in this Phase II project primarily utilized ablative electrode writing of sputter coated silica platforms. Platforms consisting of either the beveled slot (Figure 8 left), contoured slot (Figure 8 right), or oblate disc (Figure 10) trap structures were coated from both substrate surfaces with an Au on Cr combination (typically 1000-5000 Å on 50-200 Å). This patterning approach allowed incorporating more extensive ground planes in close

proximity to the active electrodes than would be allowed for using 3-D stencil masks. Utilizing an inverted T-slot fabricated into the silica as the electrode gap was also investigated. For extended electrode patterns, particularly on non-flat surfaces, it was difficult to get reproducible results with this approach. Residual debris from the etching process was difficult to remove and ultimately formed electrical shorts after metallization. A simple flat stencil mask was used during sputtering for coarse peripheral patterning to prevent coating of the substrate edges. For the oblate disc platforms, stencil masks also patterned the simpler coarse electrode gaps near the card connector end as well as isolating the RF connector key (see Figure 1).

Earlier in the project it was not obvious if ablative writing of the electrode gaps would result in a smooth enough edge structure to withstand breakdown under RF and DC applied voltages. Therefore many tests were performed to investigate the effect of the laser ablation parameters on the breakdown voltage of simple electrode structures. At Translume we were able to test holdoff at ambient pressures up to 210 V DC, whereas our collaborators at UCLA tested RF and DC holdoff under vacuum up to 800V.

Ablation parameters such as laser power, polarization, writing speed, and retrace pattern had a direct effect on the visual quality of the electrode edges. The retrace pattern is characterized by the vertical and horizontal step size and extent of rastering of the laser focus. Regardless of edge quality, the breakdown voltage was always low (<100 V) if the ablation debris was not removed as thoroughly as possible. To achieve this end, samples were aggressively sonicated in polar solvents. Also it was noted that using Cr as the attachment layer resulted in ablation debris that was more easily removed compared to using Ti for the attachment layer. This could be due to Ti readily forming oxides in the ablation process as noted by the resulting white coloration of the metal surface. Ti oxides may readily bond to the exposed silica surface in the gaps.

Once a suitable cleaning procedure was followed, the laser ablation and gap writing parameter dependence on the breakdown voltage could be investigated. Some of the data is presented in Table D. Obviously, wider gaps will holdoff discharging to higher voltages, but not as obvious is the dependence on retrace offset and laser polarization. An ablating laser polarization fixed along the laser track and a finer retrace offset yields a higher quality electrode gap. In many cases the UCLA team measured breakdown voltage in excess of 500 V (RF voltage) with a 30- μm (or narrower) electrode gaps (also see data from oblate trap tests below). This is significantly higher than previously reported values for semiconductor microtraps.

<i>Table D: Breakdown test results. Test device reference # AOT 2754</i>			
Electrode Number	Voltage breakdown [Volts]	Lateral offset (retrace separation) (micron)	Electrode Boundary Gap
1	481	2	10
2	405	2	10
3	439	2	30
4	345	2	30
5	466	1	10
6	584	1	10
7	575	1	30
8	596	1	30
9	407	0.5	10
10	679	0.5	30

Later in the project electrode patterning of electroplated platforms was investigated. Anticipating that an overly thin sputter coating on restricted surfaces may lead to excessive resistance, we tested two approaches to address this issue.

In the first case, the sputter coated surfaces of test samples were electroplated to increase the metal thickness from $\sim 0.5 \mu\text{m}$ to $5\text{-}10 \mu\text{m}$. For these initial tests, electroplating of Cu on sputtered Au on Cr surfaces was chosen due to its availability in the plating bath. Ideally Au plating would be done but other metals could be used with similar or better electrical and thermal conductivity. To offset its tendency to oxidize, a final layer of Au could be sputtered onto the Cu surface. Similar to the previous tests, a series of simple electrode patterns were written to investigate the dependence of the resultant gap quality on the laser ablation parameters. After adjusting the vertical raster to account for a thicker coating, the parameters that resulted in high quality gaps for the sputter coated samples did not yield isolated electrode gaps. That is the metal was not removed down to the silica layer but a channel was ablated into the metal coating. Increasing the laser power from 11.8mW into the $38\text{-}72 \text{mW}$ range resulted in isolated electrodes though a typically rougher gap edge was noted through microscope inspection (See Figure 15).

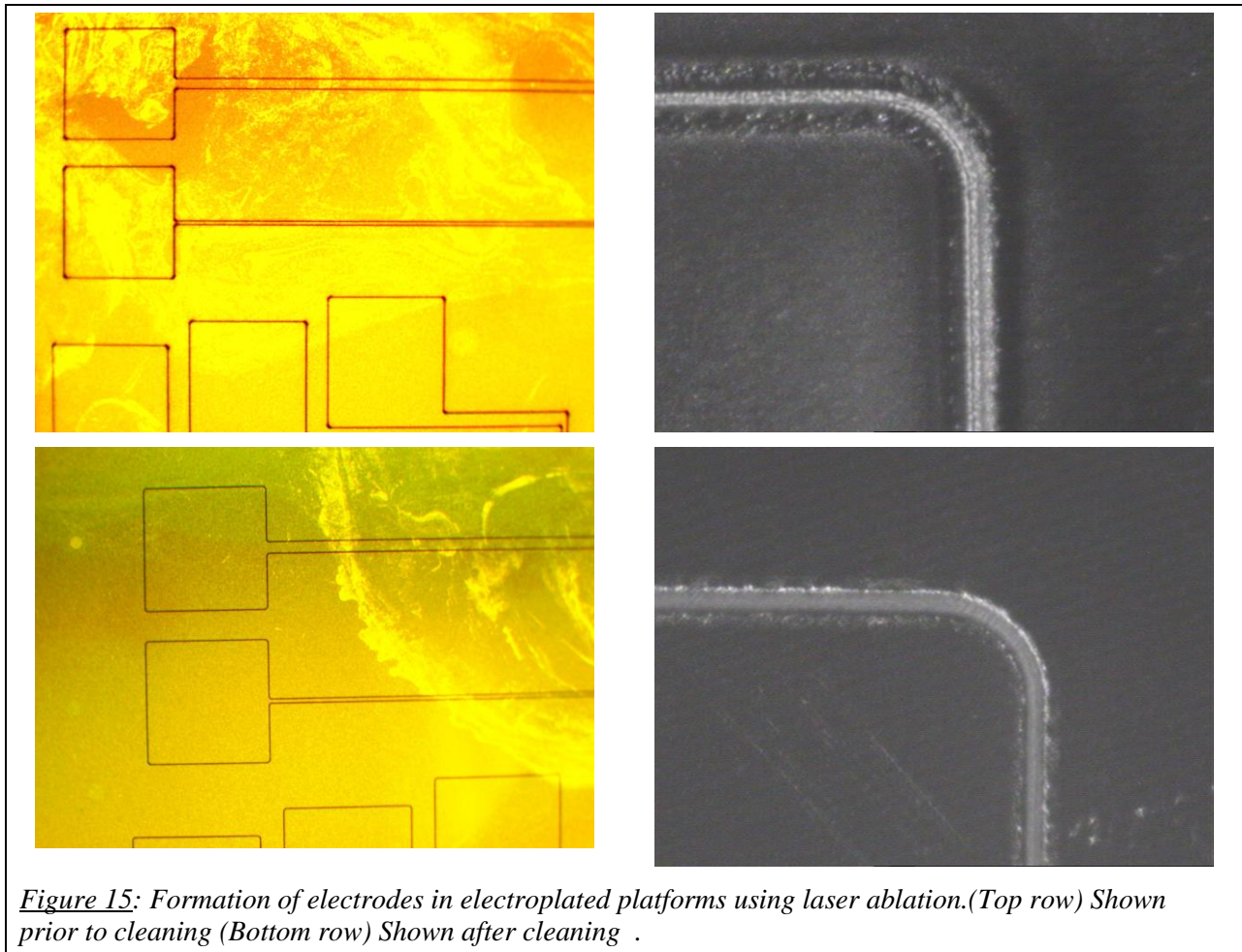


Figure 15: Formation of electrodes in electroplated platforms using laser ablation. (Top row) Shown prior to cleaning (Bottom row) Shown after cleaning .

Similarly the ablation debris, which was quite extensive here, could be removed through sonication in polar solvents. These samples were tested for DC holdoff in house (up to 210V). For a given retrace pattern, the lowest laser power that resulted in electrode isolation typically discharged at voltages lower than 210V . All electrodes ablated at higher laser powers did not break down at the equipment limit of 210V . Generally patterning at finer raster steps resulted in isolation at lower writing powers and a higher breakdown holdoff voltage. Apparently, complete

metal removal (*i.e.* no metallic micro-islands) within the gap is more important to breakdown resiliency than smoother gap edges.

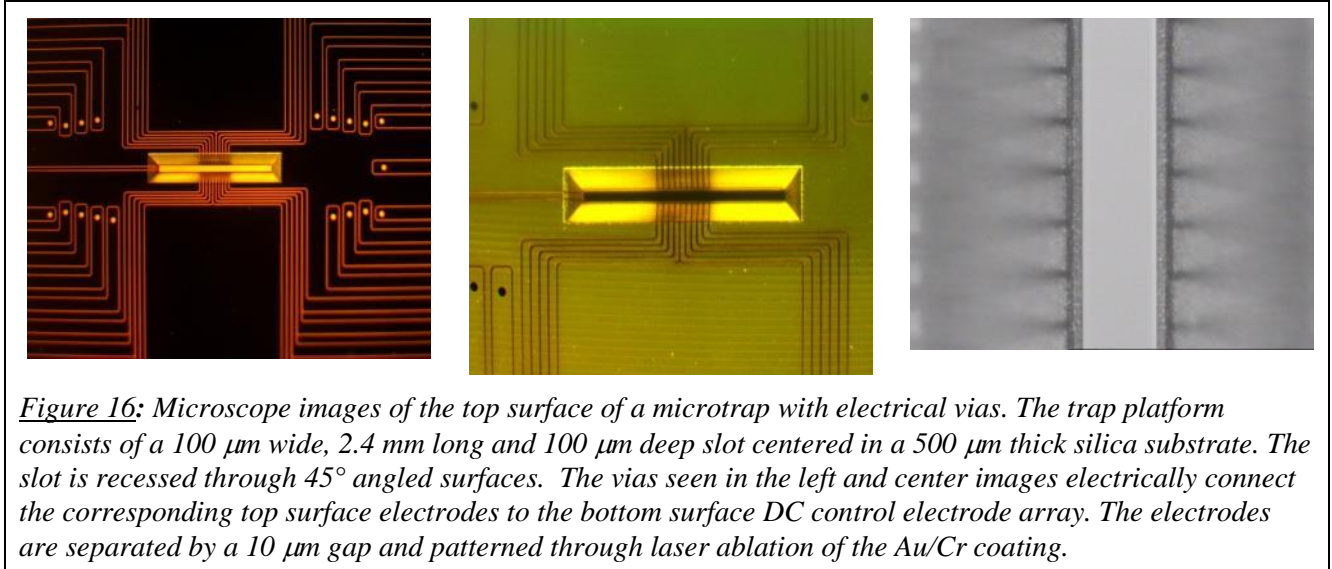
A second approach for increasing electrode thickness through electroplating involves starting with a test sample that has been sputter-coated, followed by ablative electrode patterning and cleaning. Either all electrodes (*i.e.* all coated surfaces) or a select number of individual electrodes will be electroplated in parallel, while maintaining inter-electrode isolation and, to some extent, the gap quality of the original ablated border. Here, to prevent unwanted electrode migration or short formation, the original gap quality has to be high and devoid of residual metallic islands from un-ablated regions or un-removed recast during cleaning. To implement this approach, each electrode will have to be connected to the cathode lead, and depending on the total area of each electrode, they may electroplate at different rates. We have considered during the sputtering step to coat a common bus for all electrodes with a neck region adjusted in attempt to compensate for the different electrode areas. After the electroplating process is completed, the individual electrodes would be disconnected from the bus with laser ablation. Similarly, a common lead bus can be made with a coated mask overlay. To the extent that we have tested the electroplating of existing electrodes, concern was not given to the differing plating rates, but more so, to the integrity of the original electrode gaps. Gaps written with a fine side by side raster step size of 1 μm or less will generally maintain isolation unless their total widths are smaller than 5 μm . For smaller gap widths, even when the silica floor is as clean and devoid of metal as possible, protrusions in the metal edge near the top of the gap can initiate bridging. It should be noted that though preventing the formation of shorts during electroplating is ideal, they can be eliminated afterwards through laser ablation if necessary.

All three trap platform types (all are RF Paul traps) had electrodes patterned over both polished-flat and machined-contoured surfaces. The space between adjoining electrodes is bare of the conductive Au/Cr coating exposing the SiO_2 dielectric substrate where charges could accumulate. However, this dielectric zone is slightly recessed below the surface, which reduces noise from the resultant stray fields. In addition, one can use the three-dimensional trap geometry to minimize direct line-of-sight between most uncoated dielectric areas and the trapped ions. Furthermore, because we achieved high RF breakdown values, we can work with relatively large RF traps, which place the trapped ions far-away from any potential electric field noise sources.

Generation I : Recessed slot traps

Other issues associated with patterning of electrodes on the 3D trap surfaces are concerned with coating uniformity of the vertical or angled machined surfaces. The trap platform initially proposed (1st Generation) consists of a slot 100 μm wide, ~2.4mm long, and 100 μm deep centered in a 500 μm thick fused silica substrate. The centered slot is recessed from the top and bottom surfaces of the substrate through either a constant slope at 45° angle or a contoured machined surface. The angle or contour of this depression can be readily varied in the manufacturing process. As simulation has shown, the resultant electrode orientation can influence the extent to which the DC control fields penetrate into the trap center (*i.e.* center of slot or RF ring electrode). Microscope images of the top surface of a completed trap (recessed at 45°) with a full complement of electrodes can be seen in Figure 8 and Figure 16. Here, the laser ablated pattern outlines 9 DC control electrodes on the four sloped surfaces leading to the RF ring electrode bordering the slot perimeter on both the top and bottom surfaces. The electrode gap was machined to be 10 μm wide with a 60 μm wide DC control electrode at the

trap center. The RF ring electrode consists of the center slot vertical walls 100 μm deep and ~ 15 μm perimeter fillet around the slot on both top and bottom sloped surfaces. The holes in the images in Figure 16 are vias for electrical continuity from the bottom surface set of 18 DC control electrodes to the corresponding top surface leads allowing wire bonding from one surface.



Several test pieces were manufactured with one of the two trap platform variations along with a series of test vias in the form of holes and slots. The samples were sputter coated on both top and bottom surfaces with an Au on Cr covering of different thicknesses (e.g. 1000 \AA /50 \AA , 1000 \AA /200 \AA , 5000 \AA /50 \AA , 5000 \AA /200 \AA). The trap electrode pattern and the electrodes for the test vias were then laser ablated on the top surface where isolation and through surface continuity test were performed prior to writing the bottom surface electrode pattern. Electrical isolation between electrodes was verified before and after cleaning the ablation debris off the electrode surface and gaps. Electrical continuity between the surfaces is depended on both the via size (hole diameter and slot width) and the morphology of the machined surface (*i.e.* roughness of a vertical wall compared to a sloped or flat surface). Independent of the coating thickness, a via of less than 70 μm diameter through the 500 μm substrate resulted in electrical isolation between surfaces. Several via diameters where tested using the same top surface test electrode dimensions. For via diameters of 180 μm , 220 μm , and 260 μm a resistivity of 3.3 Ω , 2.7 Ω , and 2.1 Ω respectively were measured between the top surface electrode and the bottom surface (coating thickness Au/Cr: 5000 \AA /200 \AA). Electrical continuity through slots of widths 100 μm , 120 μm , and 140 μm , all of length 2.4mm (500 μ depth), had measured resistivity of 2.8 Ω , 2.7 Ω , and 2.4 Ω , respectively. This is to be compared with the resistivity measured between the top surface RF lead through the trap center to the bottom surface. Here a higher measured resistivity of 13.6 Ω is due to coating over the rougher 45° sloped surface leading down to the trap slot despite its shallower vertical wall (100 μm compared to 500 μm for the test slots). A Gold layer of 5000 \AA resulted in a 70% lower resistivity compared to a 1000 \AA coating for a given electrode geometry regardless of the surface type (*i.e.* polished, vertical machined, or sloped machined surface). A thinner Chromium attachment layer (50 \AA compared to 200 \AA) resulted in lower resistivity on the polished surfaces and vertical machined walls but did not show a change when measured across the rougher angled wall. All 36 DC electrodes, plus the

RF ring electrode, showed breakdown holdoff up to 210V (instrument limit) against the adjacent electrodes and ground plane. It was shown through selected electroplating with Cu of the RF ring electrode (involving machined surfaces and vertical walled slot) that the resistances could be brought down under 1 Ohm.

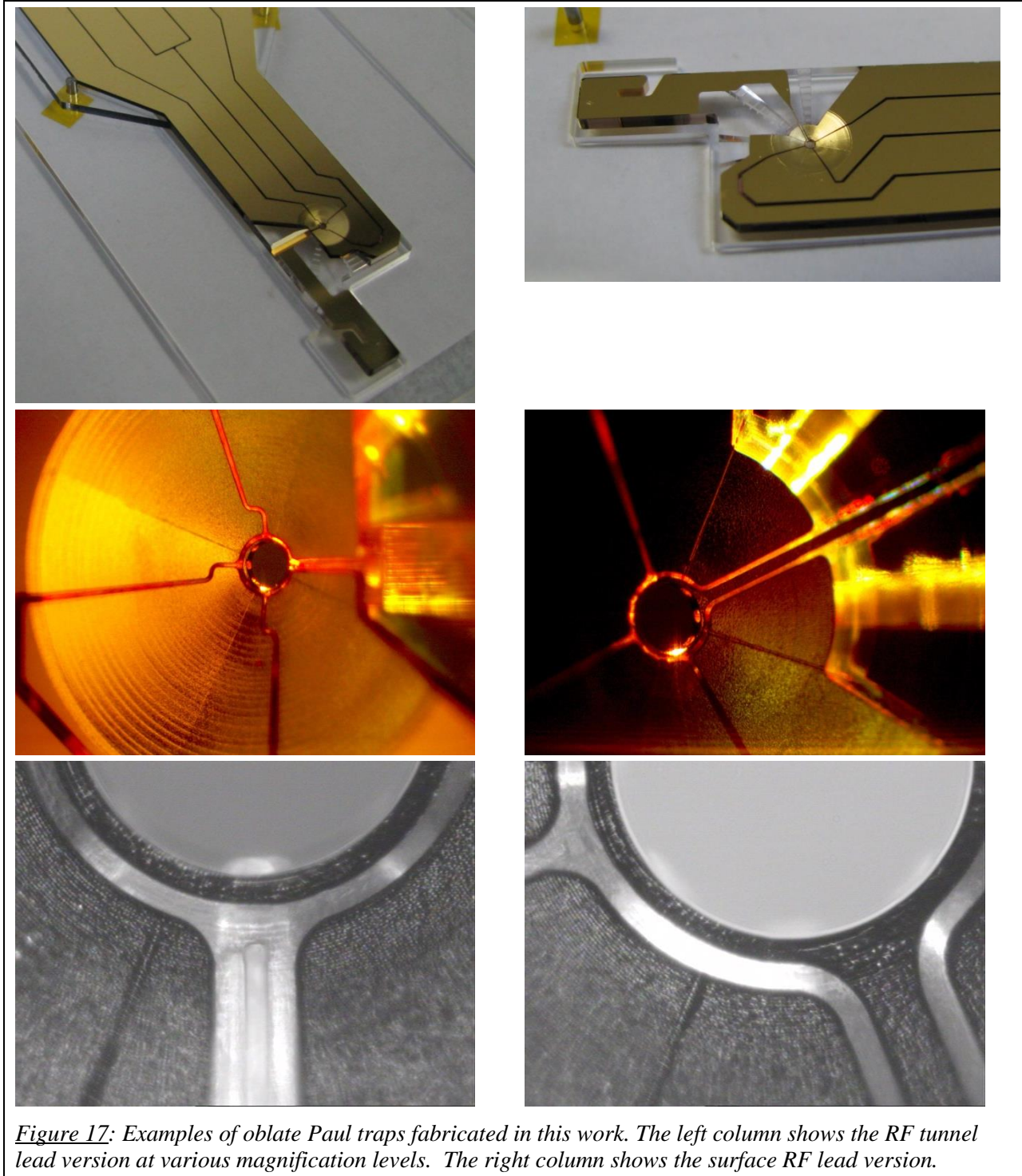
The original intent of the 1st generation slot RF traps was to interface it to the so-called standard Sandia chip carrier. Hence, the through vias allows for wire bonding of all DC control, RF ring, and ground electrodes from one side of the trap substrate. Also a mechanical interface was designed to seat the trap above the chip carrier for accessing the optical ports. Due to the difficulty in procuring these chip carriers and the lack of a compatible test jig, most subsequent effort went to the Campbell group oblate RF trap where the lead interface was simplified through their “card connector” design.

Generation II: Oblate RF disc trap

The motivation for this generation II design from the Wes Campbell group at UCLA is to generate an oblate ellipsoidal like effective potential favoring the trapping of ions in a two dimensional array with triangular lattice symmetry. Such a potential can be generated in a Paul trap of azimuthal symmetry with dominant axial confinement. Figure 17 shows examples of the particular oblate Paul traps fabricated in this work. A 1mm thick fused silica substrate is selected to fabricate the device. The trap proper is composed of the 5mm outer diameter disc which tapers down to a through hole of 0.5mm diameter and 0.1mm long side wall. These surfaces will support the electrodes with the DC control endcaps residing on the upper and lower disc faces and the RF electrode occupying the surface regions constituting the wall and rim of the center hole. The outer frame is such that the DC control electrodes are interfaced through a card connector type clip on the wider end, while the RF is source through the key like structure on the opposite end. This latter RF lead is routed through to the center ring via a subsurface pathway (RF tunnel lead) or as a narrow path on one of the disc faces (surface RF lead). The overall frame size is designed to fit into the UCLA test jig and can be made considerably smaller, of different shape, or fabricated to contain multiple traps.

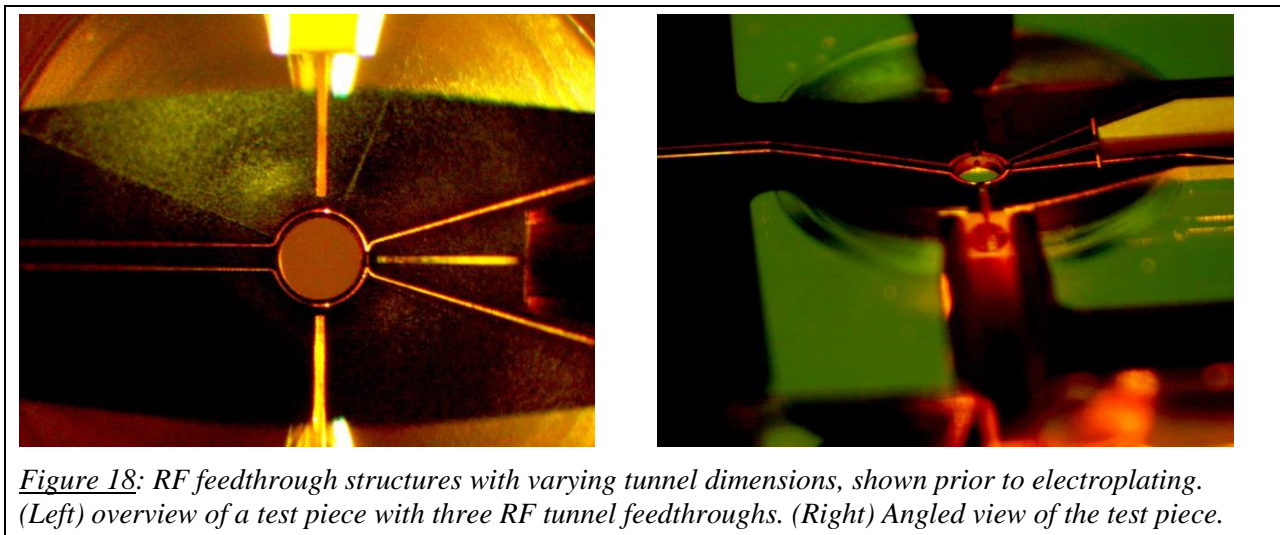
Uniquely, the UCLA oblate Paul trap design incorporates numerous subsurface ports, including one port used in part as a RF feedthrough. Any asymmetry in the trapping field due to a surface lead feeding the RF ring would be minimized by burying it in a subsurface channel beneath the surface DC control electrodes. The obvious constraint of having this port be electrically conductive throughout posed a unique fabrication challenge. As discussed above simple sputtering or evaporation could not provide the desired coating continuity through such a deep tunnel. Therefore, the RF pathway geometry was engineered to provide the desired electrical connectivity while accommodating the coating process limitations. The section further away from the central RF ring electrode is an open channel that can be coated using standard sputtering. This channel geometry cannot be extended all the way to the central RF ring, as this would introduce significant distortions of the trapping field. Thus the channel extends a little beyond the outer edge of the disc surface where it enters a tunnel with a tapered cross section opening at the RF ring wall. The tunnel length is still several millimeters in length, and consequentially, too long to sputter coat through. Therefore a slot is fabricated along the upper most region of the tunnel ceiling, up through the disc surface, and extending from the channel down to ~0.15mm from the center ring edge. This slot opening will be incorporated as part of the gap between two adjacent DC surface electrodes. For fabrication purposes, it allows a

sputtering metal beam to coat along the bottom tunnel floor extending into the enclosed part to overlap with the coating deposited from the center ring port.



Several test platforms were fabricated each consisting of three RF feedthrough structures with varying tunnel dimensions. After sputter coating (only from the top surface), electrode patterns

were ablatively written to allow convenient measuring of electrical continuity between the inner RF ring (via a surface probe electrode) and each of the RF open channel leads (Figure 18 and Figure 19). Through a trial and error process, the length of the fully enclosed tunnel was maximized while insuring that a continuous conductive path was present along the lower tunnel surface. For those structures showing electrical continuity, the resistance of this tunnel electrode was relatively high (typically 15-20 Ohm). Not knowing how this may affect performance, a secondary coating through electroplating was investigated. In the meantime, fabrication of two traps of the RF tunnel lead version were completed and delivered to our UCLA collaborators for testing. For comparison, two traps of the second version involving a surface RF lead were fabricated and sent for testing. Here the surface lead will not have as thin of a coating as the RF tunnel lead, but being routed down the disc surface, may perturb the azimuthal symmetry of the trap potential. However, simulation results suggest that the near center trapping potential should not be significantly affected by this surface lead.



Initial RF voltage test of these prototypes under vacuum did not result in any trace of breakdown (*i.e.* no observation of sparks or resonance jumps) even after coupling as much as 20W (estimated 850V) of RF power (51 -53 MHz range). However, after 2W-3W (220 - 280 V) of applied RF power was coupled to the device, a radiant glowing was noted either from the middle of the RF tunnel, or for the traps with a surface RF lead, from the RF ring. Noteworthy is that no electrode surface was damage even at significantly higher RF powers than that for the onset of the glow. A considerable range of workable trapping depths can be generated at lower RF levels lower than 2W.³

A possible cause of this radiant noise is resistive heating due to a thinner metal coating on these restricted electrode surface regions. To address this in hope of extending the operational range of these traps, the metal thickness of the electrodes were increased through electroplating. As alluded to previously (Electrodes: Metal Deposition section), the optimal approach for the electro-deposition of these 3-D structures is not straight forward and perhaps specific to the type of electrode gaps. To increase the metal coating thickness along the bottom surface of the RF tunnel and side wall of the RF ring, the Au sputtered test pieces describe above (Figure 18) were used. Here the resistances of the different tunnel electrodes (noting some were electrically isolated from the ring) were previously measured and used as a baseline for the deposition progress. Cu metal was chosen to be plated due to its different color and sheen than the Au

surface aiding in microscope inspection. Attaching the electroplating lead to the RF connector key will cause Cu to deposit on all electrically connecting pathways. In Figure 19 a test piece can be seen after electro-depositing 1.8 μm Cu showing plating of the RF key, two lead channels, ring, and the surface ring probe electrode.

The resistance measured between either of the two plated RF surface leads and the ring probe electrode was under 0.5 Ω , representing considerable improvement. The third RF feedthrough structure failed to plate with Cu because it was isolated from the ring after sputter coating (see Figure 19). Here a small gap in the coating existed due to its enclosed tunnel length being too long.

A second electroplating process was done on the same piece resulting in a 3.3 μm thickness of Cu. Besides a small decrease in the resistance of the two tunnel electrodes, the third initially isolated RF feedthrough showed continuity with the ring probe electrode ($\sim 1.4\Omega$). The apparent bridging, or edge merging, over the gap in the sputter coated tunnel can significantly extend the deposition coverage of such restricted access surfaces. Again, for this effect to occur a diffusely coated electrode border is needed. One such border in the metal coating can be seen in Figure 18 (Left) crossing the disc near the two RF channels located at the top and bottom of the image. A simple flat mask was used across the disc during sputtering where a gap existed between the bottom mask surface and disc surface. An under-coating resulted from the mask edge reaching further up the disc surface where the gap is larger.

Electroplating after shorting the middle RF electrode (opposite the ring probe electrode) between the outer disc and channel regions resulted in the coverage seen in Figure 20.

The Cu has now plated the right portion of the disc surface bordered by the ablated electrode gaps along the RF tunnel slots (at 5 and 11 o'clock) and V-shaped electrode of the center RF channel. The outer coating border defined by the mask shows the Cu electro-deposition extended further up the disc surface than the limit of the sputter coating on the left side of the disc (the side bracketing the ring probe electrode). Here, the

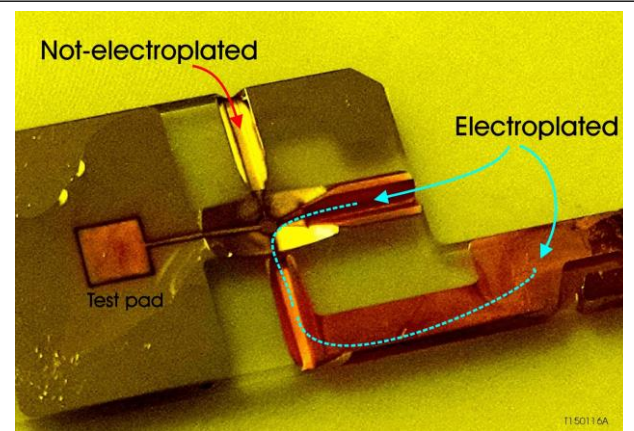


Figure 19: Test piece with three RF feedthrough structures shown after partial electroplating.

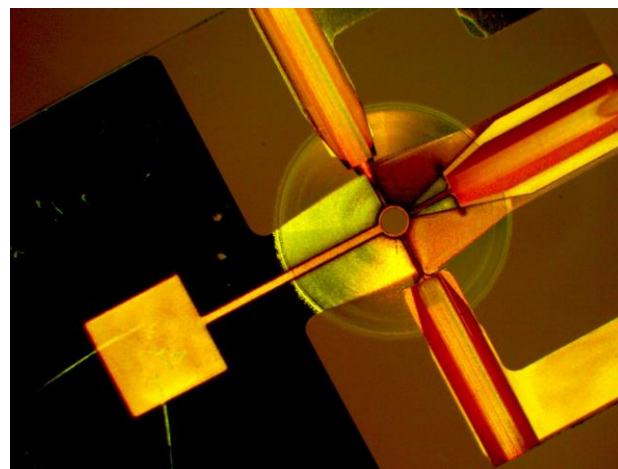


Figure 20: Test piece with three RF feedthrough structures shown after full electroplating.

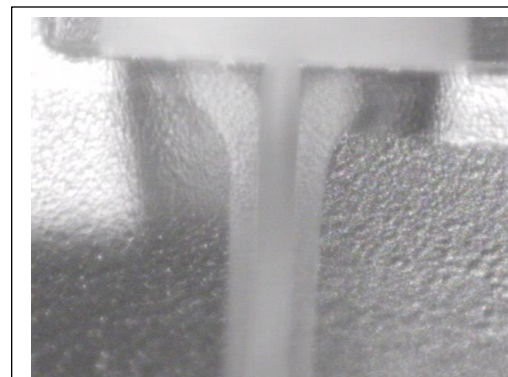


Figure 21: Electroplating boundary migration.

electroplated border is more defined and has extended some 80 to 100 μm beyond the sputtered edge (See Figure 21). Utilizing this compliment between physical deposition techniques enhances the 3-D micro-electrode fabrication potential and continues to be an active area of our process development.

Fabrication of Optical Ports and Access Ports

In a typical ion trap experiment, the trap is located in an UHV chamber, which is typically surrounded by a large external optical system that performs a variety of functions (ionization, cooling, addressing, monitoring, etc.). The spatial separation between the trap and the optics limits the efficiency of the optical system and degrades the overall system stability. Furthermore, in this traditional setting, optical access is most often limited to the direction (near-) perpendicular to the plane of the trap

The situation is not better with the recent development in surface microtraps. There, trapped particles are held a few tens of microns (or closer) above the trap surface, an especially difficult geometry for optical accessing (See Figure 22). This is especially problematic when one wants to use large numerical aperture (NA) optics to, for example, capture fluorescence signals.⁴ In particular a better optical interface, let alone a more flexible multi-function interface, would be of use to all working in this field, and clearly is needed for trap-based quantum devices to move beyond bulky experimental arrangements into more sensor-based platforms.

An ideal optical system needs to provide means to route all of the optical signals into and out of the trapping region (or trap assembly) as well as on and off the chip using optical fibers or waveguiding structures that are not susceptible to misalignment. It should provide individual ion addressing, as well as collective addressing of the trapped ion array. While numerous parties acknowledged the need for better optical system interfacing, or even for on-chip optical systems, we have not found evidences of substantial efforts dedicated to achieving this goal.

In these 3-D microtraps the species of interest is held beneath the surface of the device in recessed structures as deep as half the substrate thickness (typically a 0.5mm-2mm). This offers a considerable degree of in-plane platform real estate to fabricate monolithic access pathways to the inner trapping volume. Utilizing all three dimensions allows a higher degree of functional integration. Optical routing is a key component needed for cooling, excitation, and detection which can be distributed between the in plane (e.g. cooling and excitation) and perpendicular (high NA detection) or supported all in plane leaving the perpendicular axis for other functions (e.g. sample load or in situ surface cleaning).

While our trap substrate is transparent, the various metal electrodes, including the RF ring electrode that is found at the core of many Paul traps are not. In order to provide for an unobstructed optical path one needs to somehow eliminate any obstruction associated with

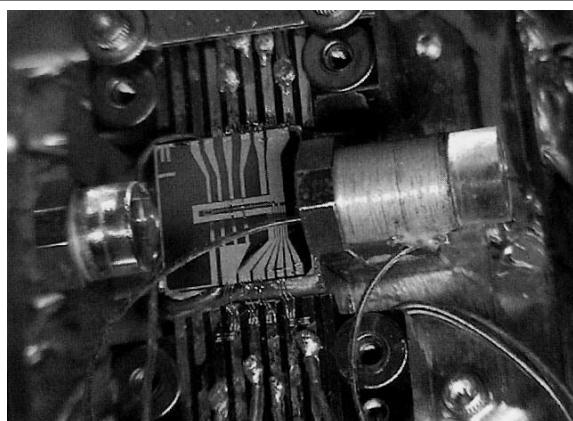


Figure 22: Collecting optical signal from surface microtrap can be challenging. This photograph shows a system where the trapped species are optically accessed in a plane parallel to the trap surface using micro-optics. (Source: Ref. 4).

electrode coating. This can be done in several ways: One could use a transparent electrode. Indium tin oxide (ITO) electrodes are commonly used in the manufacturing of flat-panels. However ITO is not transparent in the UV /blue region, which is a serious restriction in many trap applications. Further, ITO is not a very good RF material. It has high tangential losses at the RF frequencies used for ion trapping. Thus, for many trapping applications ITO is not a viable electrode material. Alternatively, one could avoid coating the electrode on the optical path of interest (using a photomask of some sort), but this approach would leave an uncoated dielectric surface in the close proximity of the trapped ions.

A third approach was adopted utilizing *femtoEtch*'s unique capabilities for fabricating high aspect open structures in the silica platform. Here unobstructed optical paths in the form of open through-holes (*i.e.* tunnels and channels) connecting the trap center (RF ring) to the periphery of the substrate were fabricated. Simulations show that portals through the center electrode surfaces, arranged in a symmetric manner, will not adversely perturb the effective trapping potential near the trap center (See Appendix A and B). Therefore, open air cavities leading from the trap center were shaped for the alignment and anchoring of optical fibers and micro-optical components, as well as for access to direct written waveguides.

This capability for shaping side access ports was used extensively in some of the traps fabricated during the course of this program. For example the oblate Paul trap designed by our UCLA partner for quantum simulation studies contains no less than eight access ports (see Figure 23), with one port used to electrically access the central RF ring, one port (asymmetric taper) used to load the ion (with the opposing blind port used for an ion dump), and six ports reserved for optical routing (the RF port can double as an optical port). All the ports are located mid-plane through the 1-mm thick substrate (*i.e.* centered 500-micron below the surface). Apparent from Figure 23, the outer ~ 2.5 mm of these in plane holes have a rectangular cross section that is down tapered toward the disc center. At a radius of ~ 2.5 mm, the hole transitions to a round cross section that continues its down taper to an opening of 0.085mm diameter at the center ring.

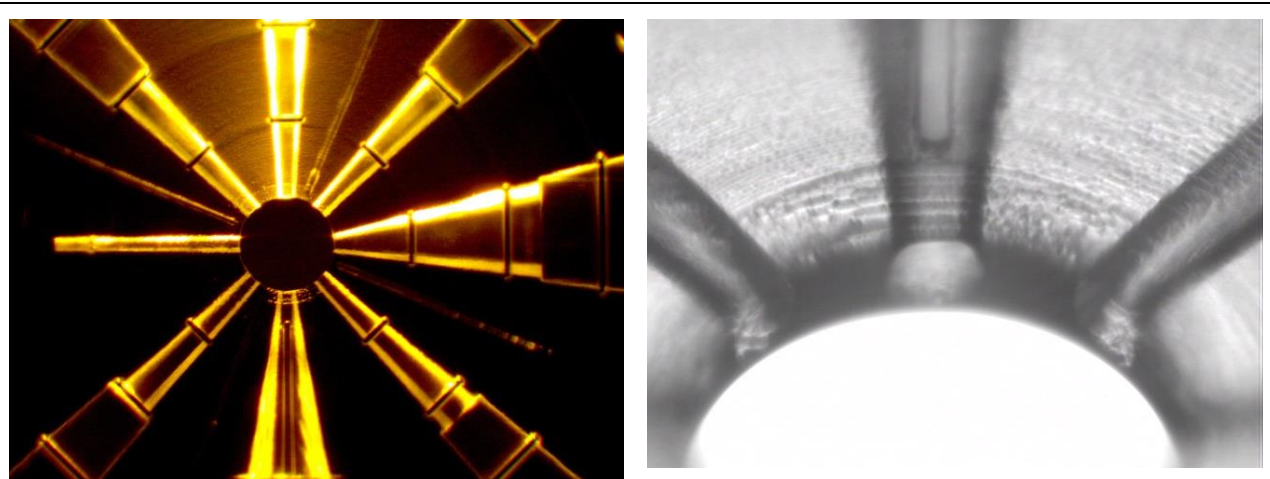


Figure 23: A Paul microtrap with eight integrated sub-surface ports. (Left) Shown prior to electrode coating. A RF feed is at 6 o'clock (also an optical port), an ion loading port is at 3 o'clock, six optical ports are on the diagonal and center vertical axes. (Right) The RF port seen at the junction with the RF ring electrode.

For testing in the UCLA experimental setup (Figure 24), open air ports were desired for free space optical routing from outside of the vacuum system. However, assemblies consisting of

fiber alignment holes and epoxy channels (See Figure 4 and Figure 25) are readily fabricated in place of the rectangular shaped hole sections.

Utilizing open ports for optical routing between fiber or waveguide terminals and the trapping center requires some means of limiting beam divergence. The fiber or waveguide end face, being a dielectric, is offset from the trap at a distance where stray fields from surface charging is not an issue. Therefore optical components for focusing, collimating, or light collecting are required. Three approaches for optical component integration were investigated to varying degrees.

The first approach is to shape the end of the fiber tip to effect a lens. Typically this is done by pulling down (down tapering) the fiber diameter leaving a small radius rounded tip over the core cross section. Several commercial companies (LaseOptics, Oz Optics, *etc.*) fabricate fiber tips for such purposes and will engage in custom design. Potentially offering a simple solution requiring only alignment and anchoring features in the silica platform, these shaped fiber tips seem to be limited for high NA light gathering and perhaps focusing over several mm distance. We have attempted to round the end of a fiber by rapidly melting the fiber tip under a controlled electric arc. Only relatively mild curvatures could be obtained with little effect on the emitted light. However, fusing a coreless fiber onto a single mode fiber to allow guided divergence of the beam followed by focusing with our larger area lens face is in testing.

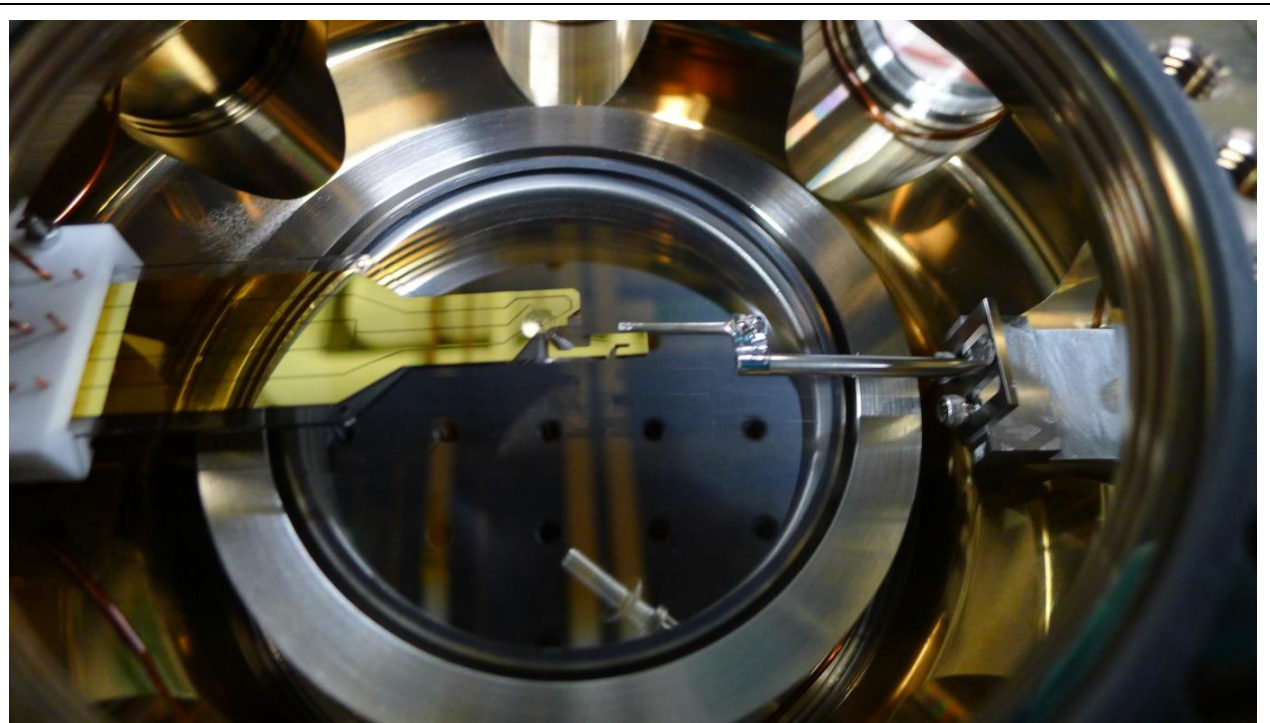


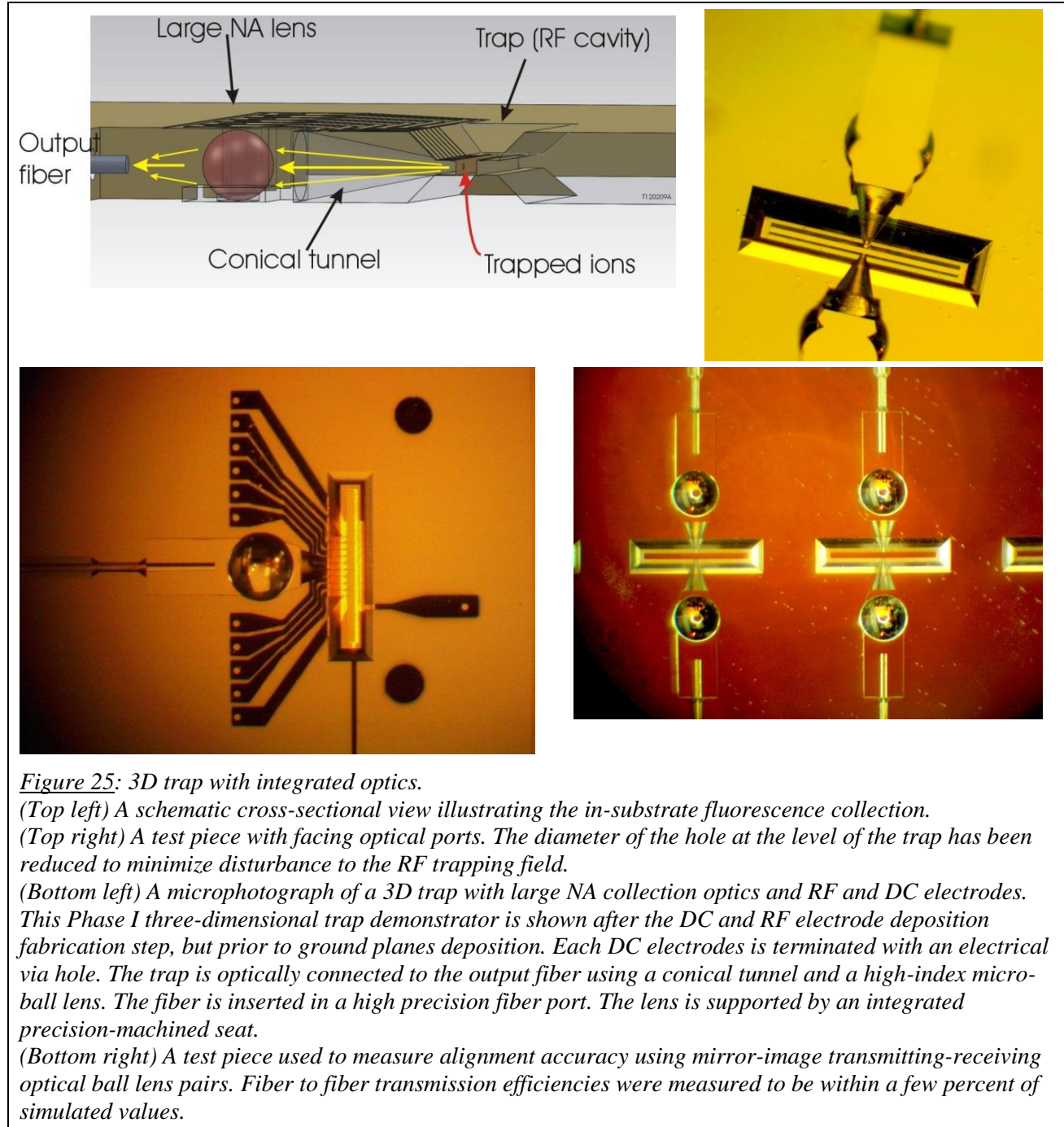
Figure 24: A 3D Paul trap in the UCLA experimental UHV chamber

A second approach for optical beam control is to fabricate portions of lensed surfaces directly into the silica platform and positioned to focus or collimate light from a fiber or embedded waveguide. We routinely fabricate such assemblies (sometimes multiple lens surfaces) as part of microfluidic chips. This approach allows for efficient utilization of the substrate since only the useable portion of a lens surface need be fabricated. These lens structures are inherently indexed to the remaining platform structure (particularly when using directly written waveguides). The lens curvature can be made aspherical minimizing aberrations typically affecting micro-optical

assemblies. The disadvantage with this monolithic approach is associated with the relatively low index of refraction of fused silica and the roughness of the machined surfaces. The former makes for relatively long focal distances and limited NA, while the latter tends to introduce scattering loss, especially at the short wavelengths used to probe the ions. Concerning the surface roughness, we have had some success smoothing these surfaces through local heating with a CO₂ laser. However, this requires open access to these surfaces which can limit optical design. The coating of these lens surfaces with certain epoxies has also been tested showing positive results. Certain UV curable epoxies are vacuum-compatible and index matched to fused silica. They can come with different viscosities of the resins to optimize surface wetting with the glass and surface tension forming a smooth outer surface.

The third approach involves fabricating a socket in the silica platform matched to the shape of an optical element that can be aligned with other platform features and epoxied or locally welded to the substrate. These optical elements can be, for example, simple small ball lenses, microlens arrays, or diffractive elements. In a separate trap, we demonstrated the fabrication of large NA fluorescence collection optics using this method (See Figure 25).

Large NA optics can be used to efficiently collect optical signals, such as fluorescence, emitted by the trapped ions. Testing alignment accuracy of this optical platform was done on several test samples where mirror image transmitting-receiving pairs were machined along with small precision apertures at their common focus. Fiber to fiber transmission efficiencies were measured to be within a few percent of simulated values (limited primarily from spherical aberrations associated with large beam area coverage of small radius of curvature optics). For lower NA applications such as cooling (Doppler or side band pumping) or excitation, transmitter and receiver fiber attachment assemblies incorporating lens structures were fabricated directly into the silica platform. Similar to the structures seen in Figure 25, these assemblies were positioned on opposite sides of the trap platforms for alignment tests. In order to reduce disturbance to the RF trapping field we generally minimize the diameter of the hole at the level it enters the trap. These through-holes are characteristically conical. This geometry provides two benefits: it minimizes any limitation to the numerical aperture of the optics, and it reduces direct line-of-sight between the trapped species and any stray charges that may be present on the tunnel sidewalls. Note that the through-holes can be (at least) partially coated if so-desired and that at the level of the RF ring they are typically fully coated.



Fabrication of Ancillary Sub-Systems

Many traps have subsystems (oven, loading guide, getter, *etc.*) that provide functions that are required for the trap to operate, but that are not considered part of the core design. These ancillary subsystems may or may not be physically part of the trap.

The UCLA trap (See Figure 10) does not incorporate much in term of sub-systems: it has one port for loading ions, but it does not have an on-board reservoir of ions (or the equivalent neutral atom stock). However, we have, either in the context of this program or in other programs, fabricated demonstrators that incorporate more substantial ancillary subsystems. For completeness we briefly discuss here two ancillary sub-systems, which we have partially demonstrated using our glass microfabrication capability. These subsystems have not yet been integrated with our traps, although it is our intent to do so in the future.

Ion Loading

One can use a set of quadrupole rods to which an RF signal is applied to confine ions radially and a static linear electrical potential to control the ions axially. This linear form of an ion trap is commonly used as a component of a mass spectrometer, either as a loading pathway or a selective mass filter (or both). Surface microtraps often incorporate two-dimensional electrode structures that provide a similar guiding (loading or shuttling) function.

During the course of this program we fabricated quadrupole rod assembly demonstrators (See Figure 26) that could provide this type of function. Note that with the *femtoEtch* fabrication process, one is not limited to straight guide geometries; curved guides can be fabricated. The spacing between the rods can be maintained (or adjusted if so desired) independently of the overall geometry, a capability that has not been explored to date.

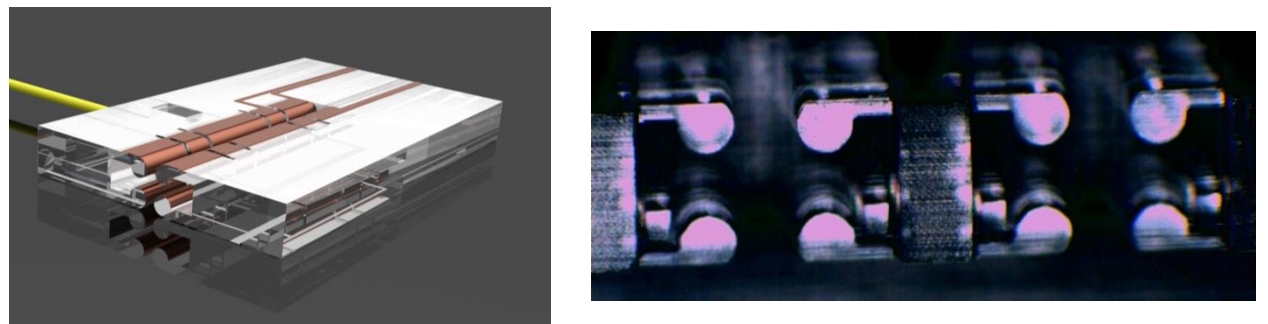


Figure 26: Linear Paul Trap. (Left) Model showing the rod geometry. (Right) Test piece with two sets of rods positioned side-by-side. This demonstrator was fabricated in a 500-micron thick fused silica blank. The length of the rod is approximately 10-mm.

Electron Impact Ionization

All ion traps require some mechanisms to generate the ions of interest. Most often an optical source of the appropriate wavelength is used to photo-ionize incoming neutral atoms. However for some applications, where an appropriate optical source is not readily available, electron impact may be used as a substitute ionization mechanism. In a context of a DOE-sponsored program⁵ we recently started exploring integrating thermal electron emitter with three-dimensional micro-trap (See Figure 27).

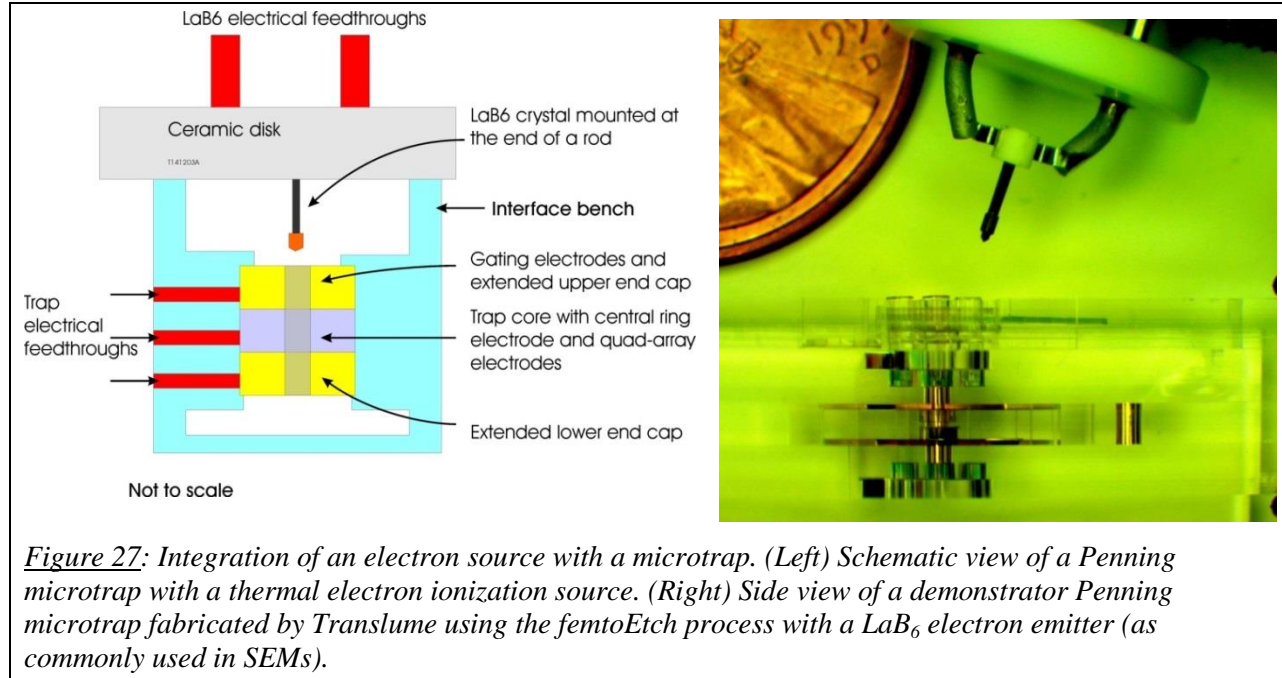


Figure 27: Integration of an electron source with a microtrap. (Left) Schematic view of a Penning microtrap with a thermal electron ionization source. (Right) Side view of a demonstrator Penning microtrap fabricated by Translume using the femtoEtch process with a LaB₆ electron emitter (as commonly used in SEMs).

Here, a commercial LaB₆ emitter (from Kimball Physics) is shown next to a micro Penning trap where it can be seen that the thermal emitter rod alone is about the size of the entire trap. Though the technical staff at Kimball Physics suggests a substantial size reduction and a fused silica mounting is doable for custom designs, the overall mounting maybe limited by the current/thermal load. A promising technology for electron impact ionization is through the use of carbon nanotube field emitters.⁶ This material has shown great potential for compact, robust electron source with low turn on fields and high stable current densities. Furthermore they can be readily assembled on silica substrates.

Trap Simulations

Appendix A discusses in details earlier simulation results (including the effect optical ports on the RF field)

Appendix B discusses design and simulation results associated with the UCLA oblate Paul microtrap fabricated by Translume

3. Future Works

Over the last few years several basic research advances have been made in ion-trap quantum systems that have significantly improved the performance of these systems. These research advances include among others (a) micro-fabricated surface ion traps⁷; (b) micro-fabricated three-dimensional traps^{8,9}, (c) cryogenic traps that have significantly reduced anomalous ion heating; (d) all glass optical cells for atomic systems; (e) all glass ion traps; (f) in-situ ion trap surface cleaning techniques^{10,2}; (g) integration of optical ports; (h) elimination of traditional large vacuum systems; (f) high-density ion trap chip wiring.

In combination, these advances provide the opportunity to develop high-performance integrated ion-trap quantum systems. In turn, such integrated systems could significantly speed the development of applications of atom and ion-based quantum technology by reducing the design-develop-deploy cycle execution time, providing a robust chip interface, and simplifying system design. This would provide greater access to this emerging technology and, therefore, allow for an expansion of explorations of quantum information processing, quantum computing and applications for quantum science.

Translume has already shown that, using direct-write processes one can fabricate (in a relatively short-time and with a modest budget) three-dimensional traps characterized by an exceptionally high degree of optical access covering a range of wavelengths spanning the near ultra-violet to the near infra-red.

Our direct-write precision machining processes incorporate large amount of flexibility, as clearly demonstrated in this program, and should be able to accommodate most existing and future ion chip trap technologies. For example we are discussing fabrication of a tandem Penning microtrap for the European TRAPSENSOR project.

There are, however, several technical challenges facing the practical integration and miniaturization of the recent advances that must be addressed. Most significantly we have not yet attempted to develop permanently sealed traps that can provide and maintain for extended periods an ultra-low pressure environment. We have also not attempted to show means to integrate ovens (but we are integrating an electron impact ionization source in a DOE-funded program to develop a magnetic field probe based on a Penning microtrap).

Further research and development is needed before potential solutions can overcome these challenges to integration.

4. Literature Cited

- ¹ J. M. Amin, H. Uys, J. H. Wesenberg, S. Seidelin, J. Britton, J. J. Bollinger, D. Leibfried, C. Ospelkaus, A. P. VanDevender and D. J. Wineland. "Toward scalable ion traps for quantum information processing", *New Journal of Physics*, **12**, 033031, (2010).
- ² N. Daniilidis, S. Gerber, G. Bolloten, M. Ramm, A. Ransford, E. Ulin-Avila, I. Talukdar, and H. Häffner., "Probing surface electric field noise with a single ion", *Phys. Rev. B*, **89**, 245435 (2014), arXiv:1307.7194
- ³ B. Yoshimura, M. Stork, D. Dadić, W. C. Campbell and J. K. Freericks "Creation of two-dimensional coulomb crystals of ions in oblate Paul traps for quantum simulations", *ArXiv* 1406.5545 (2014).
- ⁴ J. Reichel and V. Vuletic, "Atom Chips", (2011) ISBN 978-3527407552
- ⁵ DE-SC0011313 Micro Penning Traps for Continuous Magnetic Field Monitoring in High Radiation Environments
- ⁶ A. Saha, C. Jianga, and A. A. Martíá , "Carbon nanotube networks on different platforms", *Carbon*, **79**, pp 1-18, (2014).
- ⁷ S. Seidelin, *et al.*, "Microfabricated Surface-Electrode Ion Trap for Scalable Quantum Information Processing," *Phys. Rev. Lett.* **96**, 253003, (2006).
- ⁸ D. Stick, W. K. Hensinger, S. Olmschenk, M. J. Madsen, K. Schwab, and C. Monroe, "Ion trap in a semiconductor chip," *Nature Phys.* **2**, pp36-39, (2006).
- ⁹ S. Schulz, U. Poschinger, F. Ziesel, and F. Schmidt-Kaler, "Sideband cooling and coherent dynamics in a microchip multi-segmented ion trap", *New Journal of Physics*, **10**, (2008), 045007
- ¹⁰ D. Hite, Y. Colombe, A. Wilson, K. Brown, U. Warring, R. Jordens, J. Jost, K. McKay, D. Pappas, D. Leibfried, D. Wineland, "100-fold reduction of electric-field noise in an ion trap cleaned with in situ argon-ion-beam," *Physical Review Letters*, **109**, 103001, (2012).

5. Appendixes

Appendix A: Summary of ion trap simulations based on Translume's ion trap platforms

Appendix B: Creation of two-dimensional coulomb crystals of ions in oblate Paul traps for quantum simulations

Appendix A: Summary of ion trap simulations based on Translume's ion trap platforms

Note: This Appendix was included in a progress report. It is included again here for completeness.

Author: Dr. Mark Dugan, Translume

Introduction

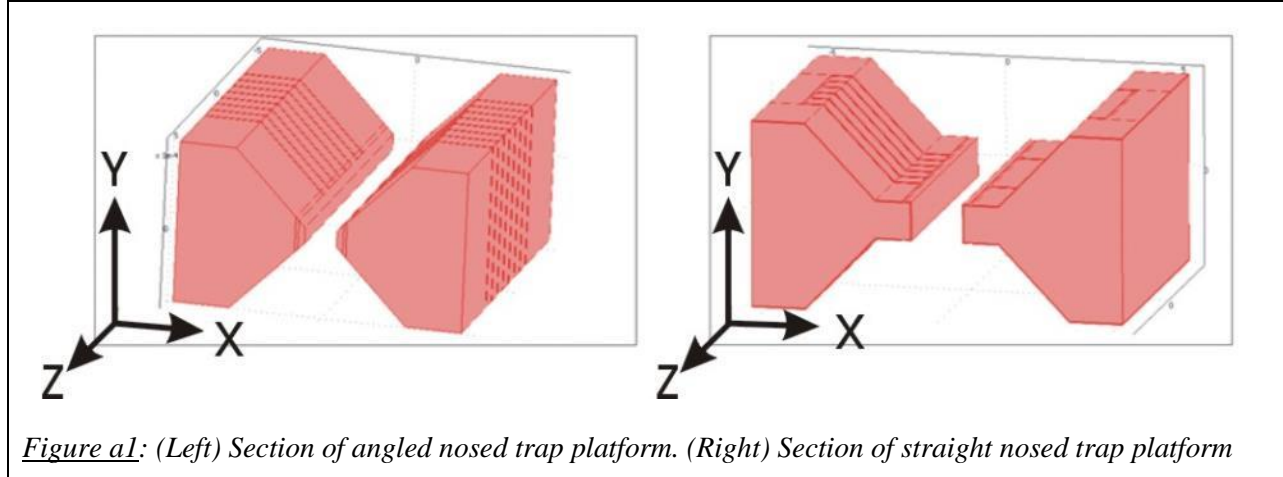
Using Translume's *femtoWrite* and *femtoEtch* processes we have manufactured several platform geometries used as a silica bench to integrate optical and electrical assemblies into a three-dimensional ion trap quantum processing unit (QPU). The flexibility in manufacturing offered by our processes raises the question of which geometries, should all be equally coated with surface electrodes, offer better performance. The performance metrics are determined by the generated trapping fields and reflect characteristic such as the trap depth, symmetry, and efficiency with respect to the sourced potentials.

To this end, simulations of the trapping fields for the various platforms efficiently aid in optimizing the design. Furthermore, additional features needed to accommodate functionality beyond direct field generation like the inclusion of open air ports through the trap structure for optical addressing are investigated for their perturbative effects on the trapping potential.

Simulation Model

The commercial finite element modeling software, COMSOL Multiphysics, is used to simulate the ion trap fields dependence on platform geometry. In all geometries considered, the platform consisted of a symmetric structure recessed in from both surfaces of an assumed 0.5 mm thick (fused silica) substrate to a vertical through slot defining the trap center.

In the actual device, surface coating of a metal (Au) is done through a patterned mask establishing a connected ring electrode around the perimeter of the through slot consisting of the vertical walls and a narrow rim (20 μm) on the adjacent top and bottom surfaces. This is the RF electrode used to generate the radial trapping fields when driven by an oscillating voltage source. Axial confinement is established through an array of DC control electrodes coated from the top (and bottom) substrate surface down the tapered walls terminating at 10 μm from the RF ring. These electrodes are 60 μm wide and are separated by a 10 μm gap. The simulated structure consists of a section of the top and bottom surface (0.5mm thick substrate), the tapered walls, level lower plane (if required), and the through slot. Sections of these surfaces are either a perfect conductor and assigned an electric potential, or an insulator with a zero or non-zero surface charge (the later to simulate stray albeit static fields from a dielectric surface). Two example platform cross sections are given in Figure a1 where the X represents the substrates in-plane axis, Y represents the substrates out-of-plane axis, and Z represents the axial dimension of the trap. The aspect ratio of the through slot along with the taper angle of the recessed walls and electrode and electrode gap widths are important design parameters in defining the trapping secular potential.



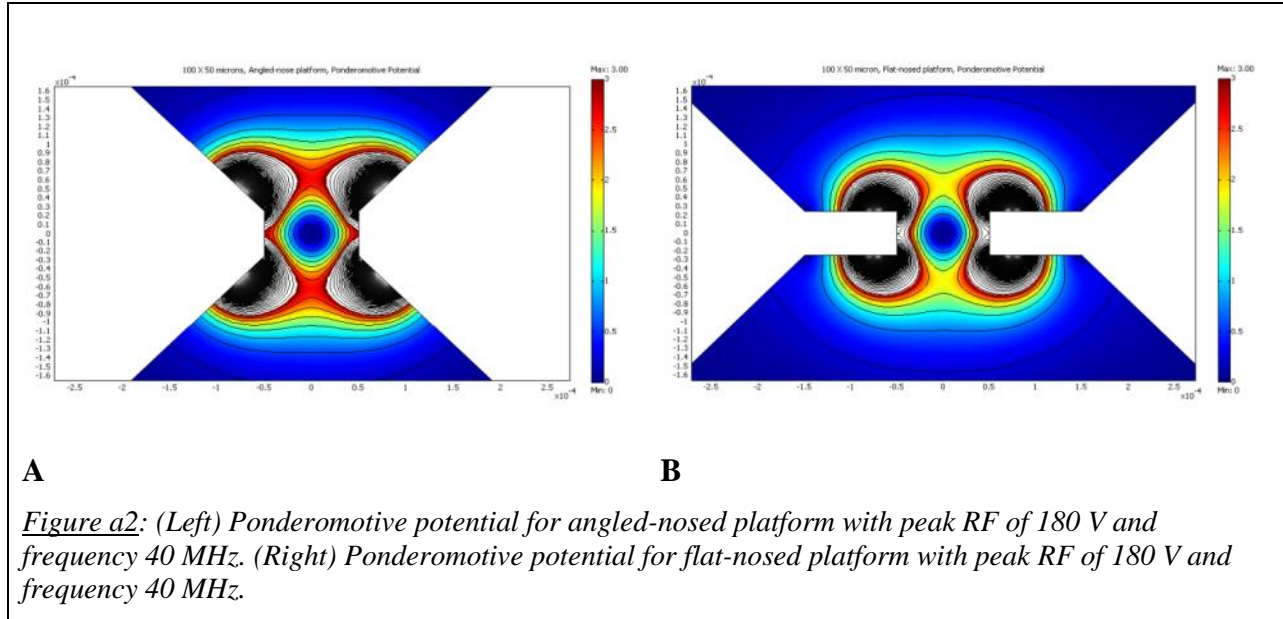
The radial time-dependent trapping potentials is simulated within the pseudo-potential approximation where the effect of the cycle averaged RF field on the ions secular motion is subsumed in a static potential well proportional to the square magnitude of the RF generated electric field. This radial (XY) confinement is further modified along the axial (Z) direction through static potentials applied to the DC control electrode surfaces. The simulation is simplified to a combination of two electrostatic models where the electric potential is directly used in one and the gradient of the electric potential is used in the other. The trap secular potential is the following some of static potentials from the DC control electrodes plus the pseudo-potential from the RF electrode.

$$U_{secular} = U_{DC} + U_{PP} = q \theta_{DC} + \frac{q^2}{4m\omega_{RF}^2} |\nabla\theta_{RF}|^2$$

Here q is the elementary charge, m is the ion mass, ω is the RF frequency / 2π , and Θ_{DC} (Θ_{RF}) is the electric potential from the DC (RF) electrode surface. The RF pseudo-potential approximation is valid only in the parameter regime where the ions are trapped in stable trajectories.

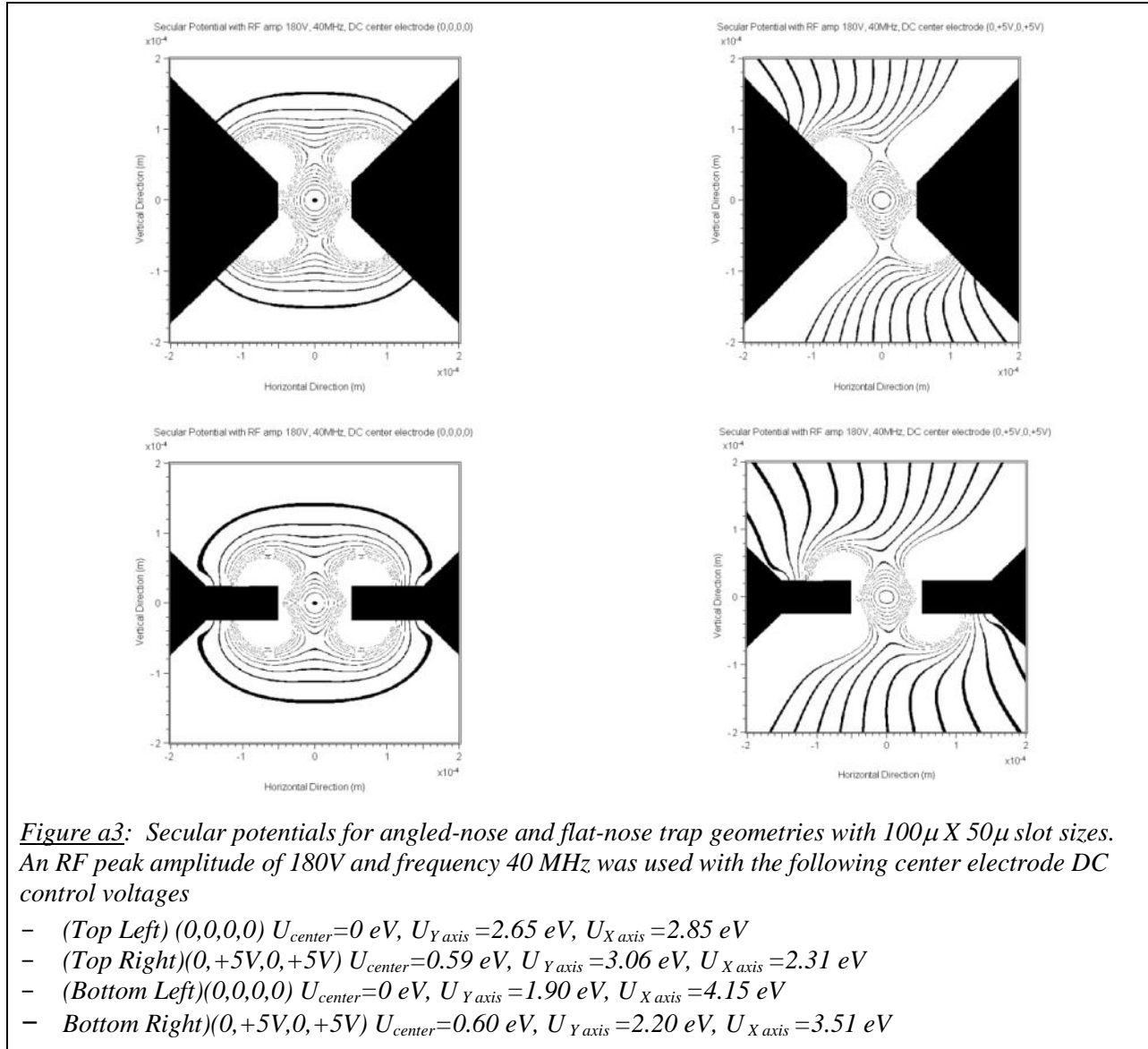
Comparing Two Trap Platform Geometries

The two trap platform sections shown in Figure a1 are examples of structures that have been fabricated with the direct write technique in a fused silica block. A 45° wall taper and slot dimensions of width $100\mu\text{m}$ and depth $50\mu\text{m}$ orient the DC control and RF electrode relative to the trap center. Using a DC control potential of 0 V, an RF frequency of 40 MHz and RF amplitude of 180 V, the simulated pseudo-potentials for trapping $^{171}\text{Yb}^+$ is shown in Figure a2.



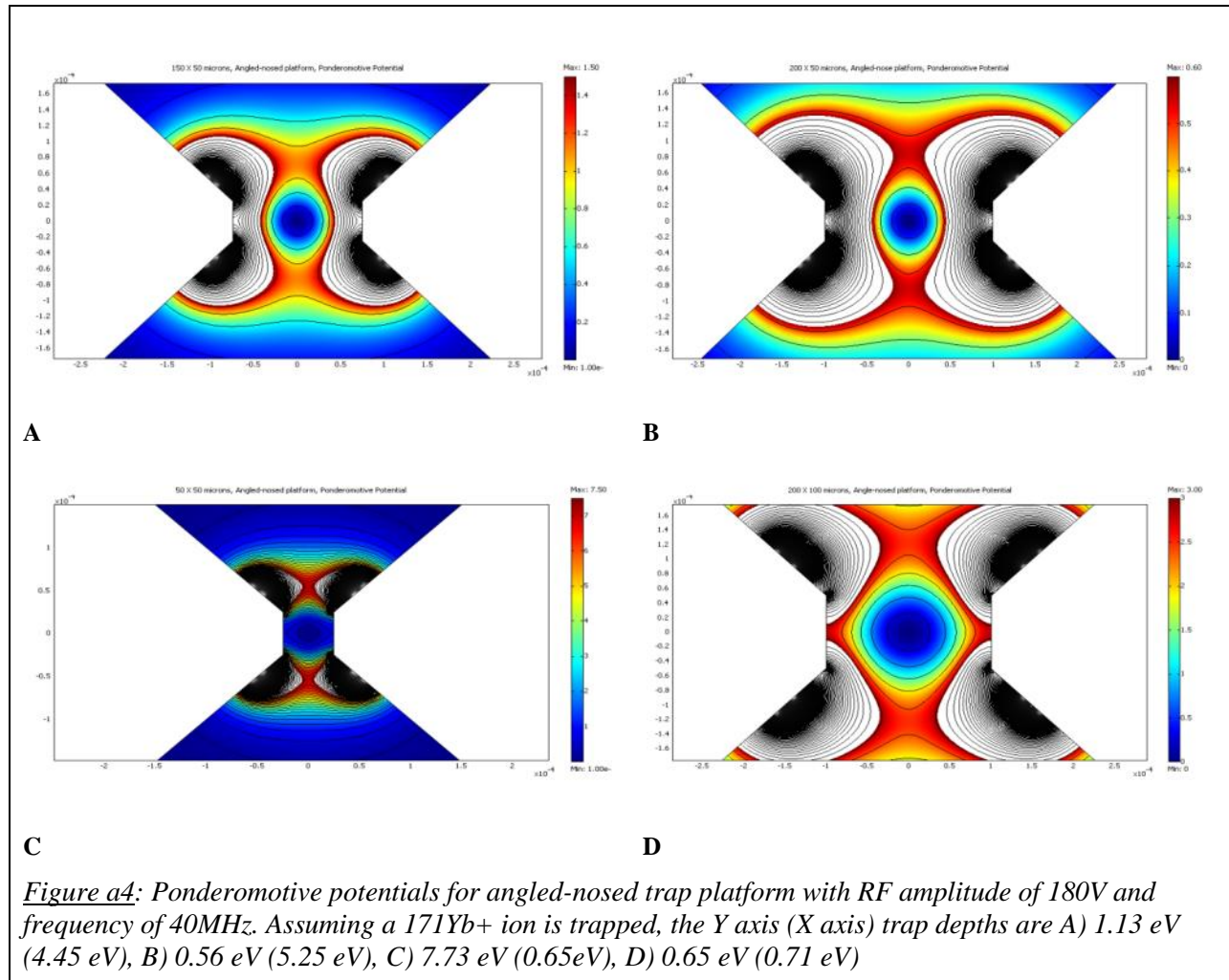
The pseudo-potential, or ponderomotive potential, from the angled-nosed platform / electrode geometry is more symmetric than that for the flat-nosed platform. It has a trap depth of 2.65 eV in the Y direction and 2.85 eV in the X direction, compared to a respective trap depth of 4.15 eV and 1.90 eV for the flat-nosed platform. The equal potential lines (Figure a2 A) are circular or quadrupolar over a larger portion of the slot cross section than that in the flat-nosed platform, which shows a quadrupole-like potential only near the trap center. Both geometries produce ponderomotive potentials of significant depth and can be perturbed by static DC control potentials of moderate voltages. Figure a3 shows plots of equal potential lines for both platform traps with, and without, +5V applied to the center DC control electrode on 2 opposite surfaces (top right and bottom left) while the DC electrodes on the 2 remaining surfaces (top left and bottom right) are at 0 V. In both cases the potential minimum at the trap center is raised ~ 0.6 eV and the symmetry of the upper bounds of the potential well appear skewed or rotated from the diagonal DC control field. The positive control voltages changes the trap depth from 2.65 eV to 3.06 eV (2.85 eV to 2.31 eV) and 1.9 eV to 2.20 eV (4.15 eV to 3.51 eV) in the X (Y) direction for the angled-nose and flat-nose platforms respectively. Assigning +5 V (+10 V) to the center electrode for all 4 surfaces will result in a 0.95 eV (1.85 eV) rise in the secular potential center minimum over that in just the ponderomotive potential alone. Axial confinement of the ions is achieved through manipulating the radial potential down the long axis of the trap by assigning different voltages to 7 DC control electrodes on all four surfaces. Simulation results for the angle-nosed platform are shown below.

Both platform/electrode geometries produce confining potential wells near the slot center that can be used to trap ions.



We are interested in integrating into the silica platform the ability to deliver optical fields to and collect fluorescence from the trapped ions. Incorporating more of the optical reading and addressing functionality in the plane of the substrate will allow for on-chip access to optical fibers through micro-lenses, micro-mirror, and/or direct written waveguides. Most of these optical assemblies require an open hole through the slot wall (*i.e.* RF electrode) to access the trapped ions. To maximize the collection angle, the hole will have to be larger than a minimum diameter, located close enough to the trap center, and connected to the collection optics via a minimum angle conical tunnel. The cone shaped open channel will also minimize the dielectric surface area within direct line of site of the trap center. The angled-nose platform, having more useable space between the tapered surfaces, is less limiting in regard to these constraints than the flat-nosed platform. Therefore we limit our consideration to this geometry and test the field dependence on the slot aspect ratio, wall taper, and on the presence of a hole in the slot (RF electrode) wall.

As a basis for comparison we use the ponderomotive potential from the angle-nosed trap with slot dimensions $100\mu\text{m} \times 50\mu\text{m}$ (Figure a2 A). It can be seen that increasing the slot aspect ratio (width / depth) reduces the trap depth with respect to the Y axis while increasing the X axis potential barrier (Figure a4 A and B). The equal potential lines show the potential well to elongate in the Y direction and resemble a quadrupole field over a reduced area near the trap minimum.



The trap depth associated with the geometry in Figure a4 B can be increased from 0.56 eV to 1.1 eV and 2.4 eV (Y direction) by increasing the RF voltage to 250V and 375V, respectively.

Decreasing the trap slot aspect ratio causes the potential well to elongate in the X direction where the potential barrier is reduced relative to that in the Y direction (Fig. a4 C). For this 45° angled slope and rectangular slot geometry an aspect ratio near 2 results in a more symmetric circular potential well over a larger area of the slot. The relative shape of the ponderomotive potential is preserved when scaling all dimensions of the platform involved in the RF field generation. This involves not only the slot dimensions at a fixed aspect ratio but also the width of the rim portion of the RF electrode on the angled surfaces and the gap between the RF electrode and the DC control electrode. This can be seen in Figure a4 D where the slot dimensions, the rim width of the RF electrode, and the electrode gap have been increased by a factor of 2 over that in Figure

a2 A. (From 100 μm by 50 μm , 20 μm wide rim electrode, 10 μm gap scaled up to 200 μm by 10 μm , 40 μm wide rim electrode, 20 μm gap.) The reduction in the trap depth with the 2X scaling is 2.65 eV to 0.65 eV in the Y direction and 2.85 eV to 0.71 eV in the X direction, which can be made up with a 2X increase in the RF voltage.

The two components of the secular potential, the static control field and the ponderomotive potential, are influenced to a degree by the angle of the wall above and below the trap slot. On these surfaces lie the ends of the DC electrodes and the rim portion of the RF ring electrode. A steeper wall angle exposes the trap center in a more direct, or less fringing, manner to the fields originating on the electrode surfaces. The effect is more pronounced on the trap depth along the Y axis (normal to the substrate plane) where a change in wall angle from 30 $^\circ$ to 45 $^\circ$ to 64 $^\circ$ at fixed aspect ratio and electrode widths, increases the barrier from 2.15 eV to 2.65 eV to 3.65eV. Confinement along the X axis is relatively independent over this angle change. Axial confinement is also stronger at larger angles from the horizontal of the DC control electrodes. Figure a5 shows the potential along the center axis of the trap platforms with wall angles of 45 $^\circ$ (A) and 64 $^\circ$ (B).

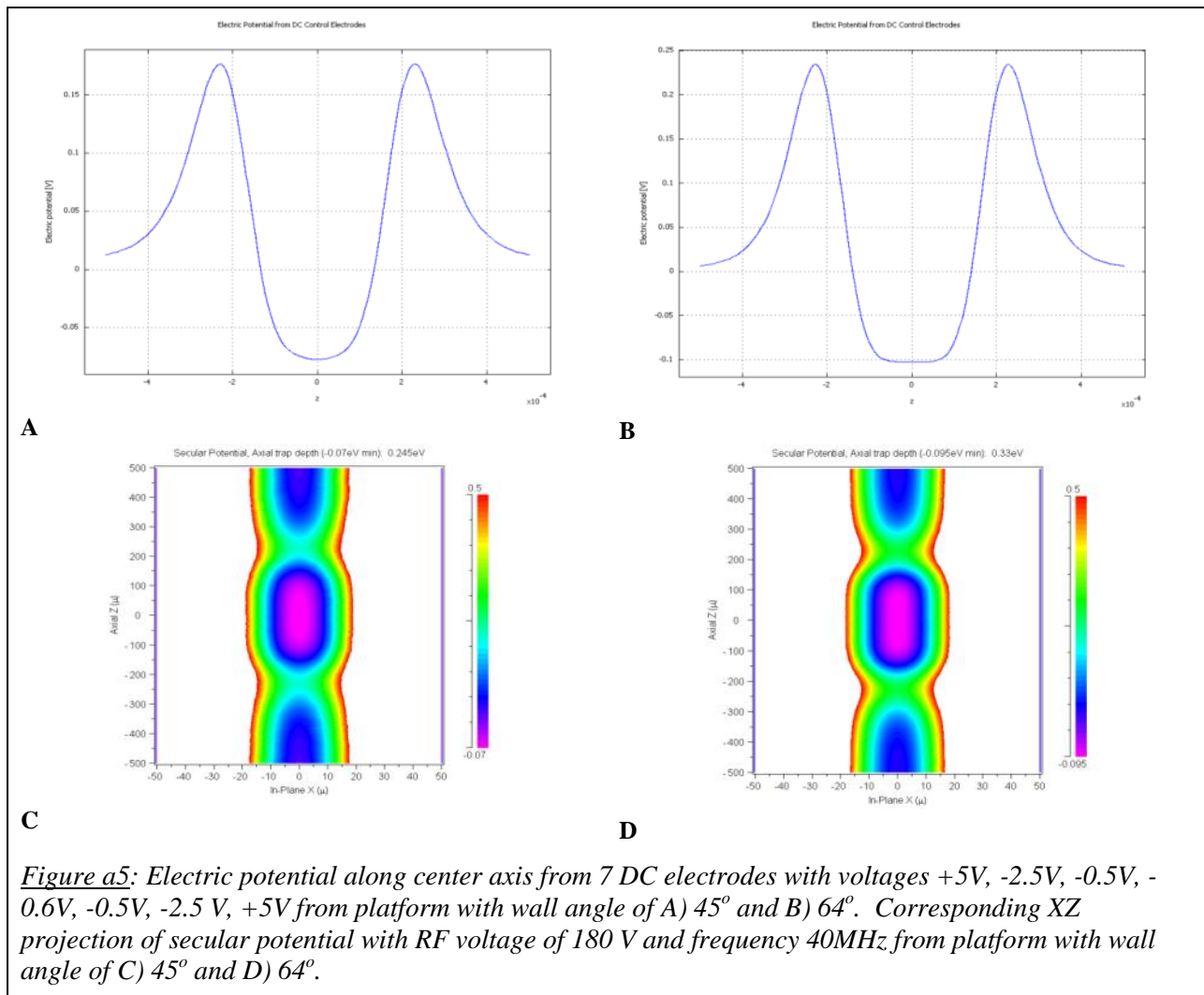
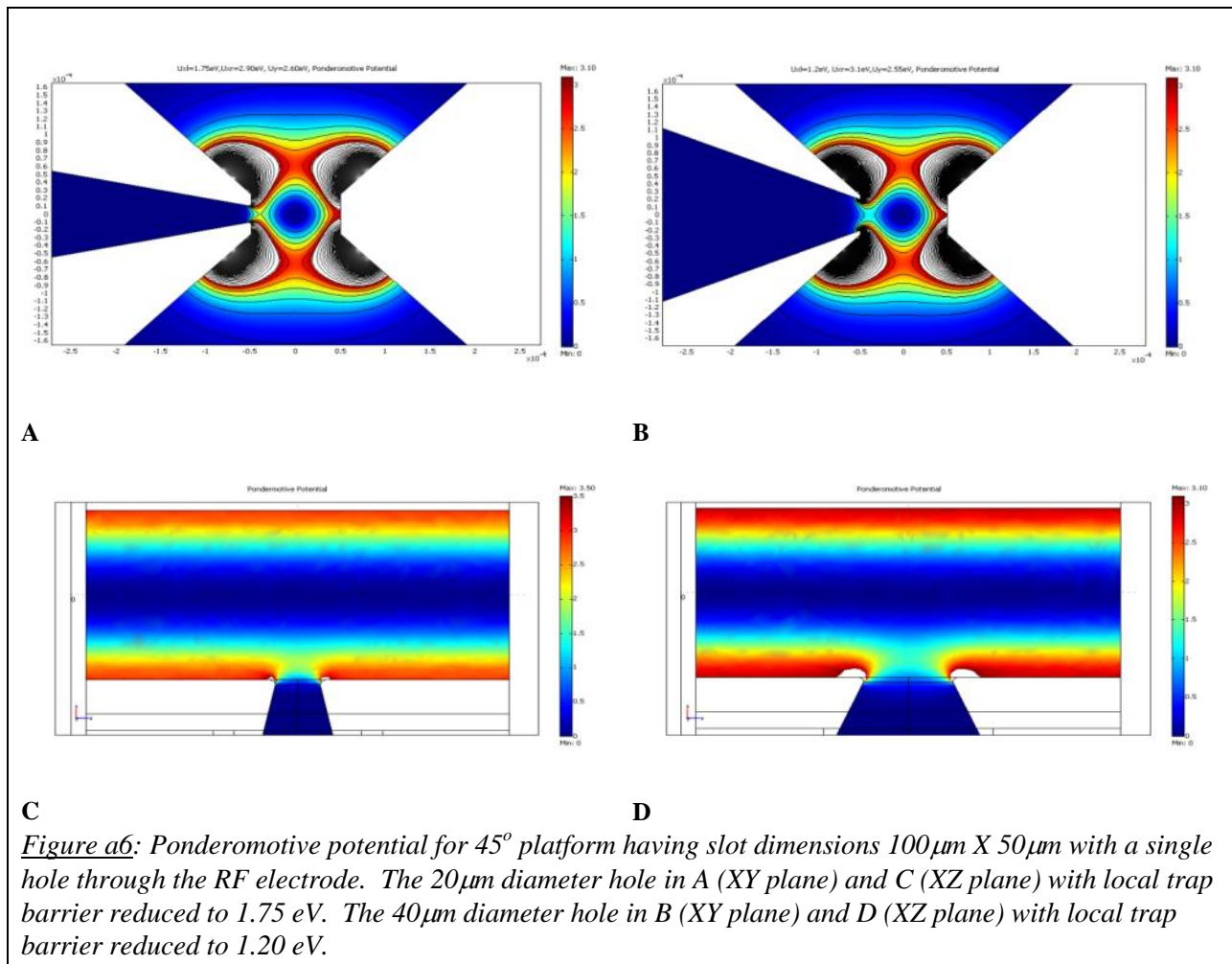


Figure a5: Electric potential along center axis from 7 DC electrodes with voltages +5V, -2.5V, -0.5V, -0.6V, -0.5V, -2.5 V, +5V from platform with wall angle of A) 45 $^\circ$ and B) 64 $^\circ$. Corresponding XZ projection of secular potential with RF voltage of 180 V and frequency 40MHz, from platform with wall angle of C) 45 $^\circ$ and D) 64 $^\circ$.

While providing larger trap depths for a given RF and DC voltage, the larger angle-nosed platforms allow positioning of micro-optical assemblies closer to the trap center for greater flexibility in light collection and delivery. However steeper walls of the silica substrate are more difficult to accurately and uniformly metal coat.

The Effect of In-plane Optical Access Port(s)

Optical access to the trapped ions from within the plane of the platform requires a hole or series of holes in the slot wall through the RF ring electrode. The continuity of the ring is maintained as long as the hole does not span the width of the electrode. The ability to side coat vertical walls during metal sputtering will result in part of the inner surface of the hole to be coated. Therefore for these simulations a width of 10 μ m to 20 μ m of the hole inner surface is considered part of the RF electrode.



The degree to which a hole perturbs the trapping fields depend on its size and placement relative other ports. This perturbation amounts to lowering of the trap potential barrier in the vicinity of the hole itself. Figure a6 (top left and top right) show the ponderomotive potential centered in front of a 20 μ m and 40 μ m hole, respectively in one side of the RF electrode wall. This platform

geometry otherwise is the same as that used to generate the result in Figure a1 A. A reduction in the barrier of the trap potential well from 2.65 eV (without hole) to 1.75 eV (20 μ m) and 1.20eV (40 μ m) occurs in the vicinity of the hole with some distortion of the equal potential lines extending along the X axis towards the trap center. The trap barrier and shape along the Y-axis or on the opposite side along X are little changed from the corresponding platform without the hole (Figure a1 A).

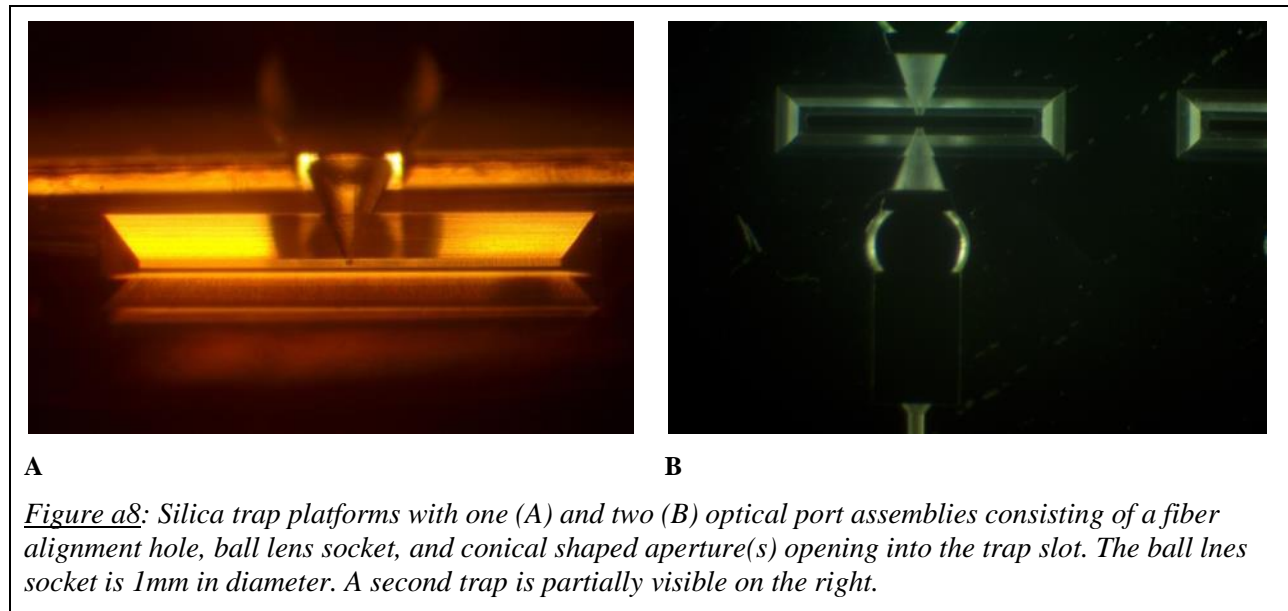
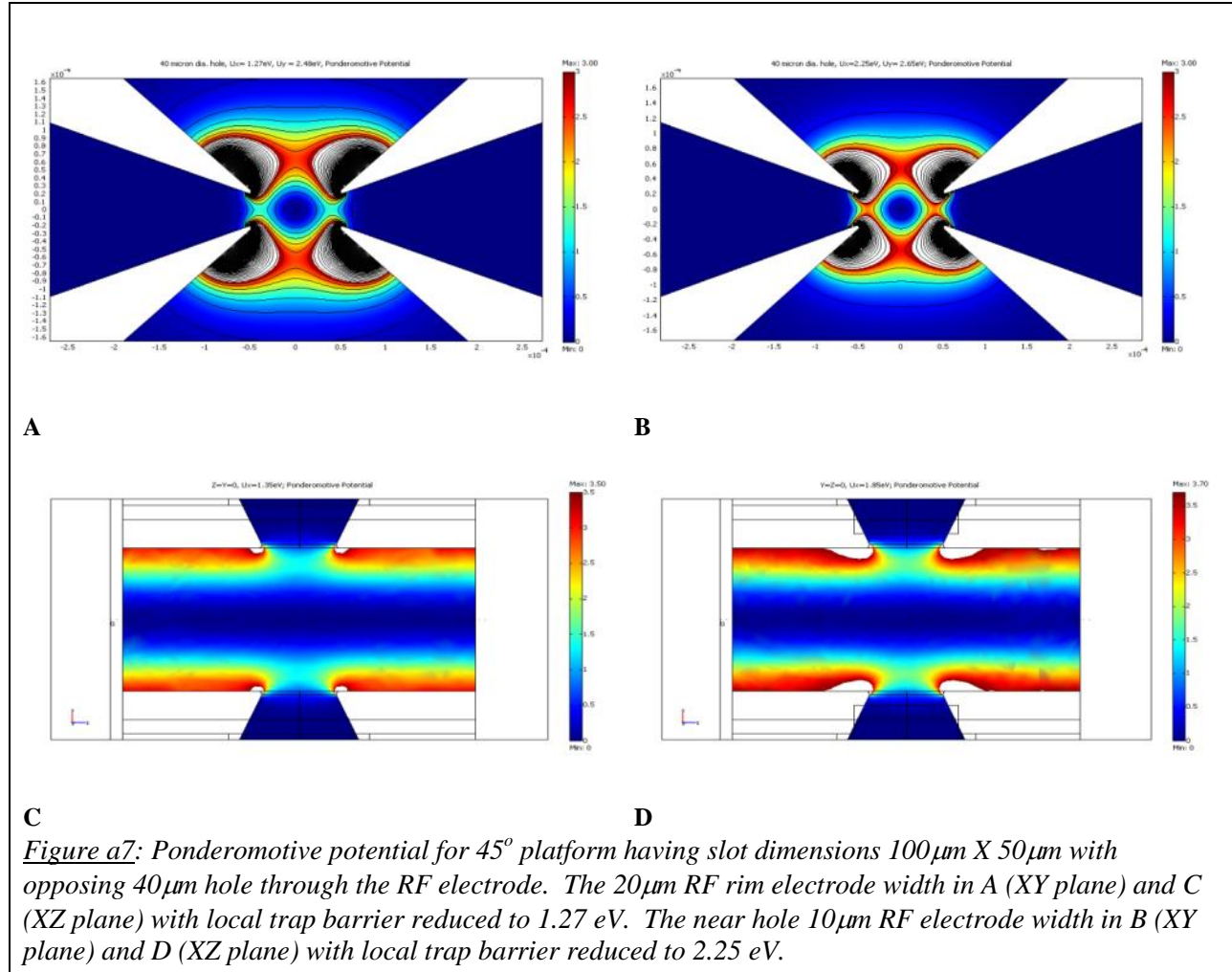
For trap platforms with larger aspect ratios (Figure a4) where the confinement is stronger in-plane (X) and weaker out of plane (Y), the presence of the hole does not perturb the equal potential surfaces that define the trapping well. For example, a 20 μ m hole through one side of the 150 μ m X 50 μ m platform in Figure a4 A reduces the X barrier on that side from 4.45 eV to 2.85 eV which is still greater than the Y potential barrier of 1.12 eV. Furthermore part of the trap distortion caused by the hole can be offset by selective biasing of the DC control electrodes or, to a greater extent, by locally modifying the platform to create a stronger in-plane confinement barrier on the hole side of the structure. However, this asymmetry in the electrode structure typically comes with an associated offset of the minimum in the potential well from the trap center.

Symmetrical Ports

Symmetry in the ponderomotive potential can be maintained despite the optical ports or local field enhancing modifications in the platform by having opposing holes on both side walls of the RF electrode. Increase in the in-plane confinement barrier in the vicinity of the holes can be obtained by decreasing the width of the rim portion of the RF electrode. For opposing 40 μ m diameter holes in Figure a7, A and C have RF rim widths of 20 μ m along the Z direction where B and D have the same 20 μ m RF rim widths which taper down to 10 μ m only over the hole dimension. In Figure a7 A and B the XY projection of the ponderomotive potential is shown where the X axis barrier is reduced from 2.85 eV for the structure without a hole (Figure a1) to 1.27 eV in A to 2.25 eV in B. The corresponding XZ projections spanning the center three DC electrodes are displayed in Figure a7 C and D. A 40 μ m diameter hole is a considerable deformation in the 50 μ m parallel electrode surfaces, yet by manipulating the electrode widths on the adjacent angled surfaces the trap depths and symmetry can be made close to that in platforms without the optic ports.

Examples of fabricated silica platforms with one and two optical ports are shown in Figure a8 A and B respectively. Also seen are structures for positioning a fiber and ball lens. The sample in Figure a8 B consisted of a series of platforms with opposing optical assemblies used for alignment test of the fiber ball lens pair with the trap aperture.

Designing large aperture access to the trap slot which can accommodate focal position tuning while maintain deep symmetric potential well is the focus of ongoing simulations.



Appendix B: Creation of two-dimensional coulomb crystals of ions in oblate Paul traps for quantum simulations

This Appendix discusses design and simulation results of the “UCLA oblate Paul microtrap”. This Paul microtrap was subsequently fabricated by Translume (see above). This paper is available from the ArXiv site (ArXiv 1406.5545 (2014).)

RESEARCH

Creation of two-dimensional coulomb crystals of ions in oblate Paul traps for quantum simulations

Bryce Yoshimura^{1*}, Marybeth Stork², Danilo Dadic³, Wesley C. Campbell³ and J. K. Freericks¹

*Correspondence:

bty4@georgetown.edu

¹Department of Physics,

Georgetown University, 37th and

O St. NW, 20007, Washington,

DC, USA

Full list of author information is available at the end of the article

Abstract

We develop the theory to describe the equilibrium ion positions and phonon modes for a trapped ion quantum simulator in an oblate Paul trap that creates two-dimensional Coulomb crystals in a triangular lattice. By coupling the internal states of the ions to laser beams propagating along the symmetry axis, we study the effective Ising spin-spin interactions that are mediated via the axial phonons and are less sensitive to ion micromotion. We find that the axial mode frequencies permit the programming of Ising interactions with inverse power law spin-spin couplings that can be tuned from uniform to r^{-3} with DC voltages. Such a trap could allow for interesting new geometrical configurations for quantum simulations on moderately sized systems including frustrated magnetism on triangular lattices or Aharonov-Bohm effects on ion tunneling. The trap also incorporates periodic boundary conditions around loops which could be employed to examine time crystals.

Keywords: ion trap; quantum simulation; Ising model

1 Introduction

Using a digital computer to predict the ground state of complex many-body quantum systems, such as frustrated magnets, becomes an intractable problem when the number of spins becomes too large. The constraints on the system's size become even more severe if one is interested in the (nonequilibrium) quantum dynamics of the system. Feynman proposed the use of a quantum-mechanical simulator to efficiently solve these types of quantum problems [1]. One successful platform for simulating lattice spin systems is the trapped ion quantum simulator, which have already been used to simulate a variety of scenarios [2, 3, 4, 5, 6, 7, 8, 9]. In one realization [10], ions are cooled in a trap to form a regular array known as a Coulomb crystal and the quantum state of each simulated electron spin can be encoded in the internal states of each trapped ion. Laser illumination of the entire crystal then can be used to program the simulation (spin-spin interactions, magnetic fields, etc.) via coupling to phonon modes, and readout of the internal ion states at the end of the simulation corresponds to a projective measurement of each simulated spin on the measurement basis.

To date, the largest number of spins simulated in this type of device is about 300 ions trapped in an a rotating approximately-triangular lattice in a Penning trap [11]. In that experiment, a spin-dependent optical dipole force was employed to realize an Ising-type spin-spin coupling with a tunable power law behavior. However, the Penning trap simulator was not able to perform certain desirable tasks such as the

adiabatic state preparation of the ground state of a frustrated magnet because it did not include a time-dependent transverse magnetic field. The complexity of the Penning trap apparatus also creates a barrier to adoption and therefore does not seem to be as widespread as radio-frequency (RF) Paul traps.

Experiments in linear Paul traps have already performed a wide range of different quantum simulations within a one-dimensional linear crystal [2, 3, 4, 5, 6, 7, 8, 9]. The linear Paul trap is a mature architecture for quantum information processing, and quantum simulations in linear chains of ions have benefited from a vast toolbox of techniques that have been developed over the years. Initially, the basic protocol [10] was illustrated in a two-ion trap [2], which was followed by a study of the effects of frustration in a three-ion trap [3]. These experiments were scaled up to larger systems first for the ferromagnetic case [4] and then for the antiferromagnetic case [5]. Effective spin Hamiltonians were also investigated using a Trotter-like stroboscopic approach [6]. As it became clear that the adiabatic state preparation protocol was difficult to achieve in these experiments, ion trap simulators turned to spectroscopic measurements of excited states [7] and global quench experiments to examine Lieb-Robinson bounds and how they change with long-range interactions (in both Ising and XY models) [8, 9].

It is therefore desirable to be able to use the demonstrated power of the Paul trap systems to extend access to the 2D physics that is native to the Penning trap systems. However, extension of this technology to higher dimensions is hampered by the fact that most ions in 2D and 3D Coulomb crystals no longer sit on the RF null. This leads to significant micromotion at the RF frequency and can couple to the control lasers through Doppler shifts if the micromotion is not perpendicular to the laser-illumination direction, leading to heating and the congestion of the spectrum by micromotion sidebands.

In an effort to utilize the desirable features of the Paul trap system to study the 2D physics, arrays of tiny Paul traps are being pursued [12, 13, 14, 15, 16, 17]. It has also been shown that effective higher-dimensional models may be programmed into a simulator with a linear crystal if sufficient control of the laser fields can be achieved [18]. In this article, we study an alternative approach to applying Paul traps to the simulation of frustrated 2D spin lattices. We consider a Paul trap with axial symmetry that forms an oblate potential, squeezing the ions into a 2D crystal. The micromotion in this case is purely radial due to symmetry, and lasers that propagate perpendicular to the crystal plane will therefore not be sensitive to Doppler shifts from micromotion. We study the parameter space of a particular model trap geometry to find the crystal structures, normal modes, and programmable spin-spin interactions for 2D triangular crystals in this trap. We find a wide parameter space for making such crystals, and an Ising spin-spin interaction with widely-tunable range, suitable for studying spin frustration and dynamics on triangular lattices with tens of ions.

In the future, we expect the simulation of larger systems to be made possible within either the Penning trap, or in linear Paul traps that can stably trap large numbers of ions. It is likely that spectroscopy of energy levels will continue to be examined, including new theoretical protocols [19]. Designing adiabatic fast-passage experiments along the lines of what needs to be done for the nearest-neighbor transverse field Ising model [20] might improve the ability to create complex quantum

ground states. Motional effects of the ions are also interesting, such as tunneling studies for motion in the quantum regime [21]. It is also possible that novel ideas like time crystals [22, 23] could be tested (although designing such experiments might be extremely difficult).

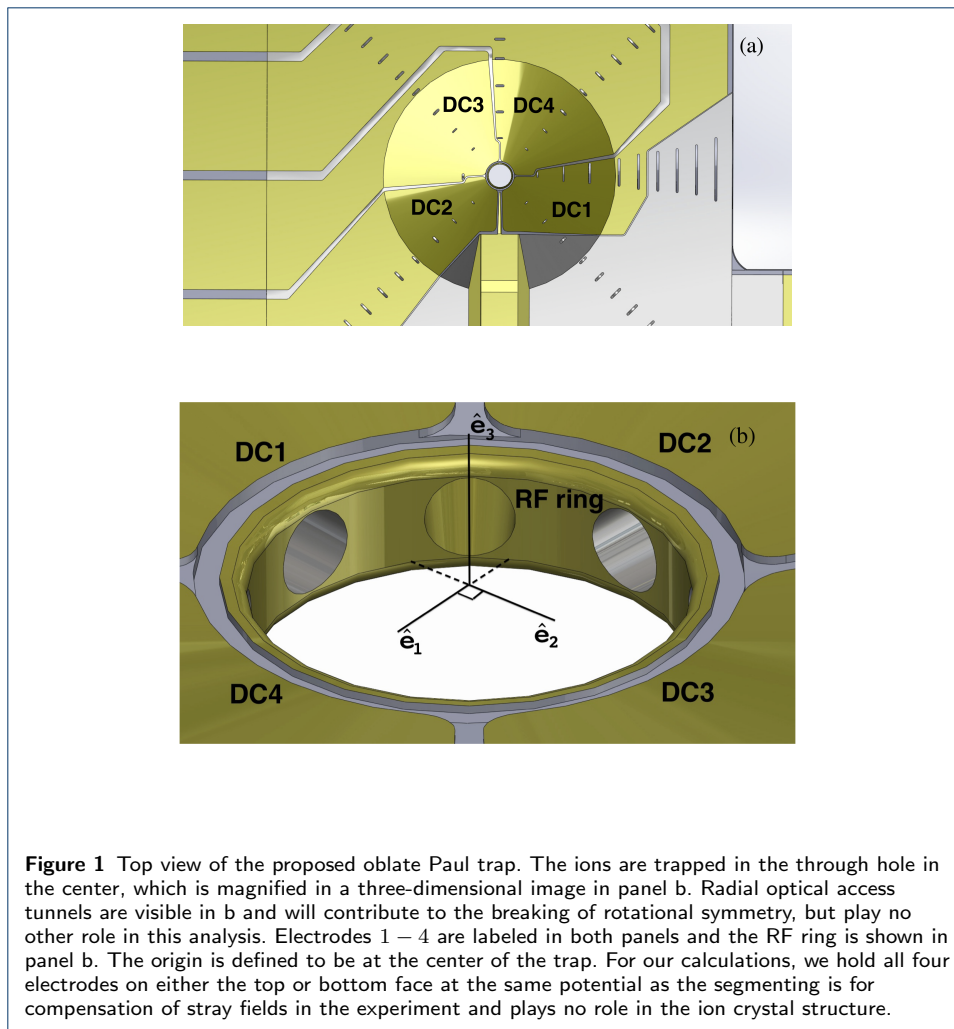
The organization of the remainder of the paper is as follows: In Sec. 2, we introduce and model the potential energy and effective trapping pseudopotential for the oblate Paul trap. In Sec. 3, we determine the equilibrium positions and the normal modes of the trapped ions, with a focus on small systems and how the geometry of the system changes as ions are added in. In Sec. 4, we show representative numerical results for the equilibrium positions and the normal modes. We then show numerical results for the effective spin-spin interactions that can be generated by a spin-dependent optical dipole force. In Sec. 5, we provide our conclusions and outlook.

2 Oblate Paul Trap

The quantum simulator architecture we study here is based on a Paul trap with an azimuthally symmetric trapping potential that has significantly stronger axial confinement than radial confinement, which we call an “oblate Paul trap” since the resulting effective potential resembles an oblate ellipsoid. As we show below, this can create a Coulomb crystal of ions that is a (finite) two-dimensional triangular lattice. 2D Coulomb crystals in oblate Paul traps have been studied since the 1980’s and were used, for instance, by the NIST Ion Storage Group [24] to study spectroscopy [25, 26], quantum jumps [27], laser absorption [28, 29] and cooling processes [30]. 2D crystals in oblate Paul traps have also been studied by other groups both experimentally [31] and theoretically [32, 33, 34, 35, 36].

The particular oblate Paul trap we study has DC “end cap” electrodes above and below a central radio-frequency (RF) ring, as depicted in Fig. 1. The trap we propose uses modern microfabrication and lithography technology (manufactured by Translume, Ann Arbor, MI) to realize the DC end cap electrodes as surface features on a monolithic fused silica substrate, providing native mechanical indexing and easier optical access to the ions than discrete end cap traps. Similar to Penning traps, oblate Paul traps can be used to study frustration effects when the lattice of ions has multiple rings. However in a Penning trap, the lattice of ions is rotating and the ions are in a strong magnetic field, which can add significant complications. In an oblate Paul trap, the lattice of ions is stationary except for the micromotion of each ion about its equilibrium positions (which is confined to the plane of the crystal by symmetry) and the qubits can be held in nearly zero magnetic field, permitting the use of the $m = 0$ “clock state” used in linear Paul trap quantum simulators [3]. For trapped ions in a crystal that is a single polygon ($N = 3, 4,$ or 5), we can study periodic boundary conditions applied to a linear chain of trapped ions in the linear Paul quantum simulators. Oblate Paul traps can also potentially be used to perform experiments that are similar to those recently exploring the Aharonov-Bohm effect [21] with more ions.

It is well known that Maxwell’s equations forbid the possibility to use a static electric field to trap charged particles in free space through Earnshaw’s theorem. However, a static electric field can create a saddle-point, which confines the charged



particles in some directions and deconfines them in the other directions. A static electric field that provides a saddle-point is

$$\mathbf{E}(\tilde{x}_1, \tilde{x}_2, \tilde{x}_3) = A(\tilde{x}_1\hat{e}_1 + \tilde{x}_2\hat{e}_2 - 2\tilde{x}_3\hat{e}_3), \quad (1)$$

where A is a constant and \hat{e}_i are the perpendicular unit vectors with $i = 1, 2, 3$. Using a static electric field with a saddle-point, both Penning and radio-frequency (RF) Paul traps have successfully trapped charged particles in free space by applying an additional field. In the Penning trap, one applies a strong uniform magnetic field, such that the charged particles are confined to a circular orbit via the Lorentz force, $q\mathbf{v} \times \mathbf{B}/c$. The RF Paul trap applies a time-varying voltage to its electrodes, which produce a saddle potential that oscillates sinusoidally as a function of time. This rapid change of sign allows for certain ions to be trapped because for particular charge to mass ratios, the effective focusing force is stronger than the defocussing force.

If the ions remain close to the nulls of the potential, then the micromotion of the ions is small, and it is a good approximation to describe the system via a

static pseudopotential that approximates the trapping effect of the time-varying potential. We use the numerical modeling software Comsol to simulate this effective pseudopotential that arises from applying a time-varying voltage to the RF ring and additional DC voltages on the other electrodes. The effective total potential energy, $\tilde{V}(\tilde{x}_1, \tilde{x}_2, \tilde{x}_3)$, of an ion in the oblate Paul trap can be approximated by

$$\tilde{V}(\tilde{x}_1, \tilde{x}_2, \tilde{x}_3) = \psi(\tilde{x}_1, \tilde{x}_2, \tilde{x}_3) + q\phi(\tilde{x}_1, \tilde{x}_2, \tilde{x}_3), \quad (2)$$

where $\psi(\tilde{x}_1, \tilde{x}_2, \tilde{x}_3)$ is the effective pseudopotential due to the RF fields and $\phi(\tilde{x}_1, \tilde{x}_2, \tilde{x}_3)$ is the additional potential due to the DC voltage applied on the top and bottom electrodes and the RF ring. The resulting pseudopotential at a certain point in space will depend upon the RF frequency, Ω_{RF} , and the RF electric field amplitude, $E_{o,RF}(\tilde{x}_1, \tilde{x}_2, \tilde{x}_3)$, at that point [37] and is given by

$$\psi(\tilde{x}_1, \tilde{x}_2, \tilde{x}_3) = \frac{q^2}{4m\Omega_{RF}^2} |\mathbf{E}_{o,RF}(\tilde{x}_1, \tilde{x}_2, \tilde{x}_3)|^2, \quad (3)$$

which depends on the charge, q , and the mass, m , of the particular ion being trapped. After simulating the field using Comsol, we find that the electric field amplitude from the RF field near the trap center can be approximated by

$$\mathbf{E}_{o,RF} \approx -\frac{2V_{o,RF}}{r_o^2} (\tilde{x}_1 \hat{e}_1 + \tilde{x}_2 \hat{e}_2 - 2\tilde{x}_3 \hat{e}_3), \quad (4)$$

where $V_{o,RF}$ is the amplitude of the RF voltage. Plugging this into Eq. (3) yields

$$\psi(\tilde{x}_1, \tilde{x}_2, \tilde{x}_3) = \frac{q^2 V_{o,RF}^2}{m\Omega_{RF}^2 r_o^4} (\tilde{x}_1^2 + \tilde{x}_2^2 + 4\tilde{x}_3^2), \quad (5)$$

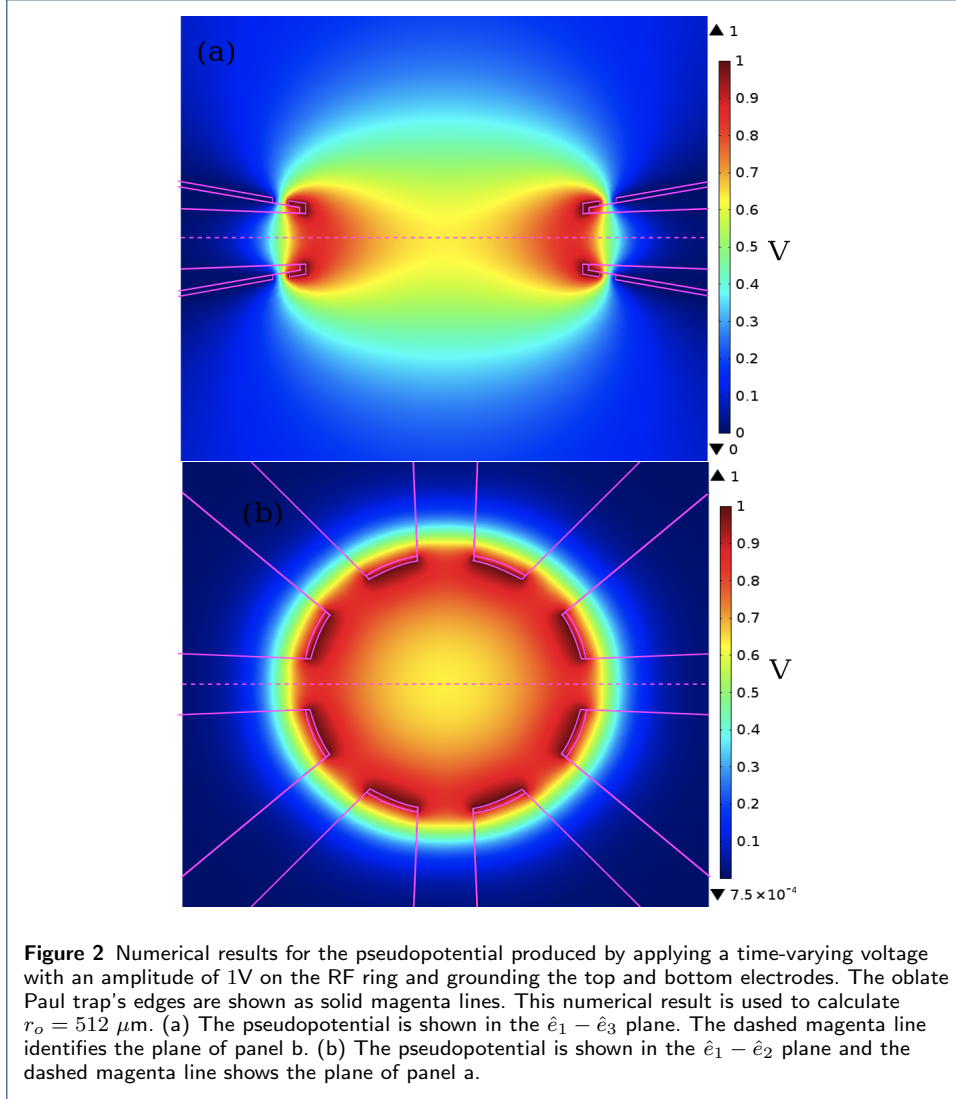
where $r_o = 512 \mu\text{m}$ is a fitting parameter, that is determined by grounding the top and bottom electrodes and numerically modeling the square of the RF electric field amplitude, as shown in Fig. 2. We calculate the DC electric field as having 3 contributions: one from the voltage applied to the RF ring, $\phi_r(\tilde{x}_1, \tilde{x}_2, \tilde{x}_3)$, one from the voltage applied to the top electrodes, $\phi_t(\tilde{x}_1, \tilde{x}_2, \tilde{x}_3)$ and one from the bottom electrodes, $\phi_b(\tilde{x}_1, \tilde{x}_2, \tilde{x}_3)$. The DC voltage on the RF ring, $\phi_r(\tilde{x}_1, \tilde{x}_2, \tilde{x}_3)$, is given by

$$\phi_r(\tilde{x}_1, \tilde{x}_2, \tilde{x}_3) = \frac{V_r}{r_o^2} (\tilde{x}_1^2 + \tilde{x}_2^2 - 2\tilde{x}_3^2) \quad (6)$$

where V_r is the DC voltage on the ring.

We numerically model the electrostatic potential due to the DC voltage applied to the either the top or bottom electrodes, as shown in Fig. 3. We find that near the trap center, the numerical results for the electrostatic potential produced by a voltage of $V_{t,b}$ the top or bottom electrodes is reasonably modeled by the polynomial

$$\phi_{t,b}(\tilde{x}_1, \tilde{x}_2, \tilde{x}_3) = V_{t,b} \left(\frac{\tilde{x}_3^2}{a^2} + \frac{\tilde{x}_3}{b_{t,b}} - \frac{\tilde{x}_1^2 + \tilde{x}_2^2}{c^2} + d \right), \quad (7)$$

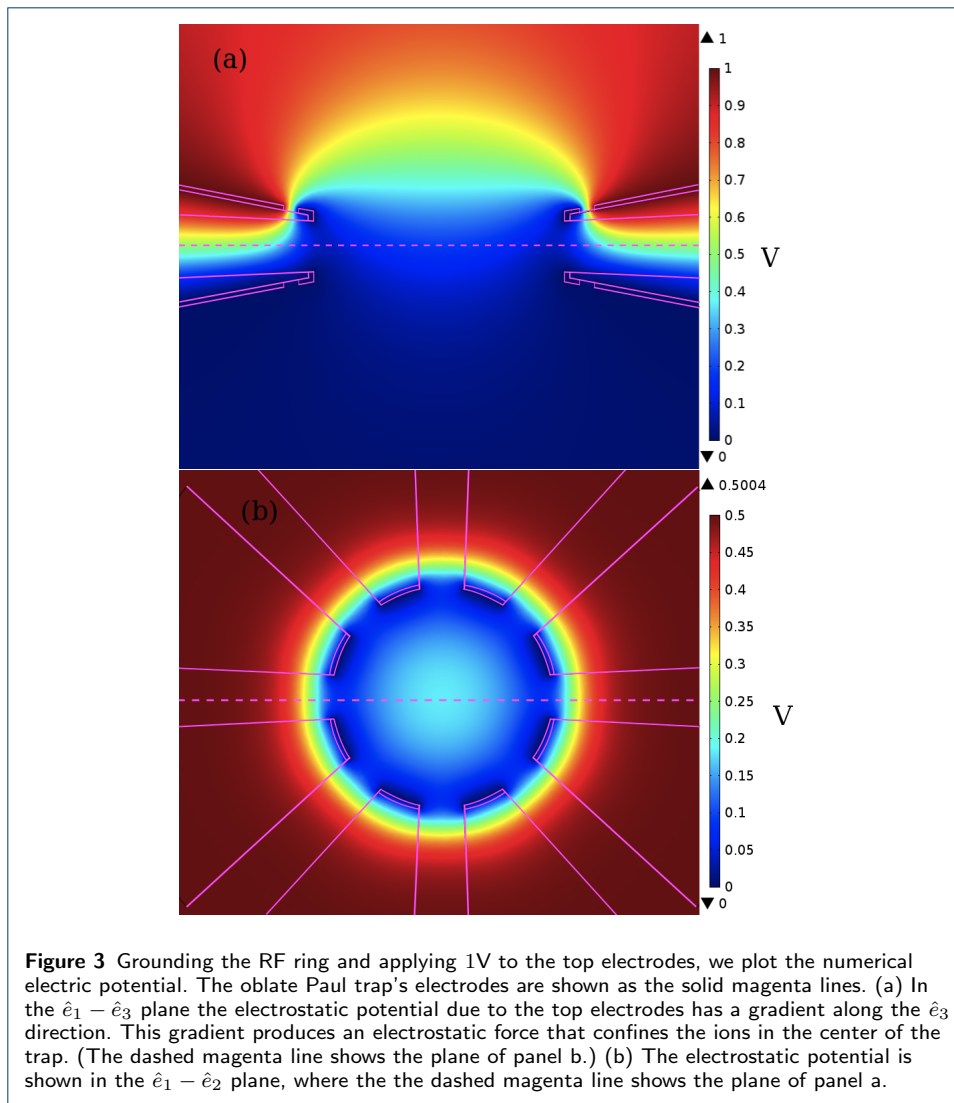


with fitting parameters $a = 524 \mu\text{m}$, $b_t = 761 \mu\text{m}$, $b_b = -761 \mu\text{m}$, $c = 704 \mu\text{m}$, $d = 0.812$. Due to the symmetry of the oblate Paul trap, the parameters satisfy $b_b = -b_t$.

We can use the results from Eqs. (5-7) in Eq. (2) to yield the final effective potential energy of an ion in this oblate Paul trap

$$\begin{aligned} \tilde{V}(\tilde{x}_1, \tilde{x}_2, \tilde{x}_3) &= \frac{q^2 V_{o,RF}^2}{m \Omega_{RF}^2 r_o^4} (\tilde{x}_1^2 + \tilde{x}_2^2 + 4\tilde{x}_3^2) + q \frac{V_r}{r_o^2} (\tilde{x}_1^2 + \tilde{x}_2^2 - 2\tilde{x}_3^2) \\ &+ qV_t \left(\frac{\tilde{x}_3^2}{a^2} + \frac{\tilde{x}_3}{b_t} - \frac{\tilde{x}_1^2 + \tilde{x}_2^2}{c^2} + d \right) + qV_b \left(\frac{\tilde{x}_3^2}{a^2} + \frac{\tilde{x}_3}{b_b} - \frac{\tilde{x}_1^2 + \tilde{x}_2^2}{c^2} + d \right). \end{aligned} \quad (8)$$

Since the effective potential energy is just a function of $\tilde{x}_1^2 + \tilde{x}_2^2$, it is rotationally symmetric around the \hat{e}_3 -axis and we would expect there to be a zero frequency rotational mode in the phonon eigenvectors. That mode can be lifted from zero by breaking the symmetry, which can occur by adding additional fields that do not



respect the cylindrical symmetry, and probably occur naturally due to imperfections in the trap, the optical access ports, stray fields, etc.

3 Equilibrium structure and normal modes

Using Eq. (8) (the calculated pseudopotential), we solve for the equilibrium structure of the crystal in the standard way. We first construct an initial trial configuration for the ions and then minimize the total potential energy of the oblate Paul trap (including the trap potential and the Coulomb repulsion between ions), as summarized in Eq. (9); MatLab is used for the nonlinear minimization with a multidimensional Newton's method. We rewrite the total potential energy of the

oblate Paul trap in a conventional form (up to a constant) via

$$\begin{aligned} \tilde{V}(\tilde{x}_1, \tilde{x}_2, \tilde{x}_3) &= \frac{1}{2}m \left[\sum_{i=1}^2 (\omega_{\psi,i}^2 + \omega_{r,i}^2 - \omega_{t,i}^2 - \omega_{b,i}^2) \tilde{x}_i^2 + \omega_{\psi,3}^2 \tilde{x}_3^2 - \omega_{r,3}^2 \tilde{x}_3^2 \right. \\ &\quad \left. + \omega_{t,3}^2 \left(\tilde{x}_3 + \frac{a^2}{2b_t} \right)^2 + \omega_{b,3}^2 \left(\tilde{x}_3 + \frac{a^2}{2b_b} \right)^2 \right] + \frac{1}{2} \sum_{\substack{m,n=1 \\ m \neq n}}^N \frac{k_e e^2}{\tilde{r}_{nm}}, \end{aligned} \quad (9)$$

where $k_e = 1/4\pi\epsilon_0$. Here \tilde{x}_{in} is the i^{th} component of the n^{th} ion's location and $\tilde{r}_{nm} = \sqrt{(\tilde{x}_{1n} - \tilde{x}_{1m})^2 + (\tilde{x}_{2n} - \tilde{x}_{2m})^2 + (\tilde{x}_{3n} - \tilde{x}_{3m})^2}$. The frequencies in Eq. (9) are defined via

$$\omega_{\psi,1} = \frac{\sqrt{2q}V_{0,RF}}{m\Omega_{RF}r_0^2}, \quad \omega_{\psi,1} = \omega_{\psi,2} = \frac{\omega_{\psi,3}}{2} \quad (10)$$

$$\omega_{r,1} = \sqrt{\frac{2qV_r}{mr_0^2}}, \quad \omega_{r,1} = \omega_{r,2} = \frac{\omega_{r,3}}{\sqrt{2}} \quad (11)$$

$$\omega_{t,1} = \sqrt{\frac{2qV_t}{mc^2}}, \quad \omega_{et,1} = \omega_{t,2} = \frac{a}{c}\omega_{t,3}. \quad (12)$$

We will express all distances in terms of a characteristic length, l_o , which satisfies

$$l_o^3 = \frac{k_e e^2}{m\omega_{\psi,3}^2} \quad (13)$$

and we will work with dimensionless coordinates $x = \tilde{x}/l_o$ when calculating the equilibrium positions. Furthermore, we measure all frequencies relative to $\omega_{\psi,3}$. The normalized frequencies are

$$\beta_i = \sqrt{(\omega_{\psi,i}^2 + \omega_{r,i}^2 - \omega_{t,i}^2 - \omega_{b,i}^2)/\omega_{\psi,3}} \quad (14)$$

for $i = 1, 2$, $\beta_{r,3} = \omega_{r,3}/\omega_{\psi,3}$, $\beta_{t,3} = \omega_{t,3}/\omega_{\psi,3}$, and $\beta_{b,3} = \omega_{b,3}/\omega_{\psi,3}$. The dimensionless total potential energy becomes

$$V = \frac{\tilde{V}}{k_e e^2/l_o} = \frac{1}{2} \sum_{n=1}^N [\beta_1^2 x_{1n}^2 + \beta_2^2 x_{2n}^2 + x_{3n}^2 - \beta_{r,3}^2 x_{3n}^2 + \quad (15)$$

$$\beta_{t,3}^2 (x_{3n} + x_{o,t})^2 + \beta_{b,3}^2 (x_{3n} + x_{o,b})^2] + \frac{1}{2} \sum_{\substack{m,n=1 \\ m \neq n}}^N \frac{1}{r_{nm}}, \quad (16)$$

where we have defined $x_{o,t} = a^2/(2l_o b_t)$ and $x_{o,b} = a^2/(2l_o b_r)$.

To find the equilibrium positions, we use the gradient of the total potential energy and numerically minimize the total potential energy using a multidimensional

Newton's method. The gradient of Eq. (9) is

$$\vec{\nabla}V = \sum_{i=1}^3 \sum_{m=1}^N \frac{\partial V}{\partial x_{im}} \hat{e}_{im} = \sum_{m=1}^N \left[\sum_{i=1}^2 \hat{e}_{im} \beta_i^2 x_{im} + \hat{e}_{3m} [x_{3m} - \beta_{r,3}^2 x_{3m} + \beta_{t,3}^2 (x_{3m} + x_{o,t}) + \beta_{b,3}^2 (x_{3m} + x_{o,b})] + \sum_{\substack{n=1 \\ n \neq m}}^N \sum_{i=1}^3 \hat{e}_{im} \frac{x_{in} - x_{im}}{r_{nm}^3} \right]. \quad (17)$$

The force on ion m in the \hat{i} direction will be $-\vec{\nabla}V \cdot \hat{e}_{im}$. We seek the solution in which all ions lie in a plane parallel to the $\hat{e}_1 - \hat{e}_2$ plane, such that $x_{3m} = \bar{x}_3$ for all $m \in [1, N]$. As a result of this condition, $x_{3n} = x_{3m}$, and there is no x_3 contribution to the Coulomb potential term. The value of \bar{x}_3 is determined by setting the \hat{e}_{3m} term equal to zero in Eq. (17) and is given by the condition

$$\bar{x}_3 = \frac{-\beta_{t,3}^2 x_{o,t} - \beta_{b,3}^2 x_{o,b}}{1 - \beta_{r,3}^2 + \beta_{t,3}^2 + \beta_{b,3}^2}, \quad (18)$$

Using \bar{x}_3 , the ion equilibrium positions are numerically obtained when all $3N$ components of the force on each ion are zero, which is given by $\vec{\nabla}V|_{equilib.} = 0$.

After the equilibrium positions $\{\bar{x}_{in}, n = 1, \dots, N, i = 1, 2, 3\}$ are found, we expand the total potential about the equilibrium positions up to quadratic order

$$V = V^{(0)} + \sum_{i=1}^3 \sum_{m=1}^N q_{im} \frac{\partial}{\partial x_{im}} V|_{eq} + \frac{1}{2} \sum_{i,j=1}^3 \sum_{n=1}^N q_{im} q_{jn} \frac{\partial^2 V}{\partial x_{im} \partial x_{jn}}|_{eq}. \quad (19)$$

The nonzero terms of the expansion are the zeroth order and the quadratic terms; the first order term is zero because the equilibrium position is defined to be where the gradient of the total potential is zero, however the zeroth term is also neglected since it is a constant. We calculate the Lagrangian of the trapped ions using the quadratic term of the Taylor expanded total potential, with q_{in} being the dimensionless displacement from the equilibrium position for the n^{th} ion in the i^{th} direction. The expanded Lagrangian becomes

$$L = \frac{1}{2\omega_{\psi,3}^2} \sum_{i=1}^3 \sum_{m=1}^N \dot{q}_{im}^2 - \frac{1}{2} \sum_{i,j=1}^3 \sum_{m,n=1}^N q_{im} K_{mn}^{ij} q_{jn}, \quad (20)$$

where K_{mn}^{ij} represents the elements of the effective spring constant matrices which are given by

$$(i = 1, 2) K_{mn}^{ii} = \begin{cases} \beta_i^2 - \sum_{\substack{n'=1 \\ n' \neq m}}^N \left[\frac{1}{\bar{r}_{n'm}^3} - 3 \frac{(\bar{x}_{in'} - \bar{x}_{im})^2}{\bar{r}_{n'm}^5} \right] & \text{if } m = n \\ \frac{1}{\bar{r}_{mn}^3} - 3 \frac{(\bar{x}_{in} - \bar{x}_{im})^2}{\bar{r}_{mn}^5} & \text{if } m \neq n \end{cases} \quad (21)$$

$$K_{mn}^{12} = K_{mn}^{21} = \begin{cases} 3 \sum_{\substack{n'=1 \\ n' \neq m}}^N \frac{(\bar{x}_{1n'} - \bar{x}_{1m})(\bar{x}_{2n'} - \bar{x}_{2m})}{\bar{r}_{n'm}^5} & \text{if } m = n \\ -3 \frac{(\bar{x}_{1n} - \bar{x}_{1m})(\bar{x}_{2n} - \bar{x}_{2m})}{\bar{r}_{mn}^5} & \text{if } m \neq n \end{cases} \quad (22)$$

$$K_{mn}^{33} = \begin{cases} \beta_3^2 - \sum_{\substack{n'=1 \\ n' \neq m}}^N \frac{1}{\bar{r}_{n'm}^3} & \text{if } m = n \\ \frac{1}{\bar{r}_{mn}^3} & \text{if } m \neq n \end{cases} \quad (23)$$

where $\beta_3 = \sqrt{1 - \beta_{p,3}^2 + \beta_{et,3}^2 + \beta_{eb,3}^2}$ and $\bar{r}_{mn} = \sqrt{(\bar{x}_{1m} - \bar{x}_{1n})^2 + (\bar{x}_{2m} - \bar{x}_{2n})^2}$ is the planar interparticle distance between ions n and m . Note that motion in the 3-direction (axial direction) is decoupled from motion in the $\hat{e}_1 - \hat{e}_2$ plane.

After applying the Euler-Lagrange equation to Eq. (20) and substituting the eigenvector solution $q_{im} = \text{Re}(b_{im}^\alpha e^{i\omega_\alpha t})$, we are left to solve the standard eigenvalue equation

$$-b_{im}^\alpha \left(\frac{\omega_\alpha}{\omega_{\psi,3}} \right)^2 + \sum_{j=1}^3 \sum_{n=1}^N K_{mj}^{ij} b_{jn}^\alpha = 0. \quad (24)$$

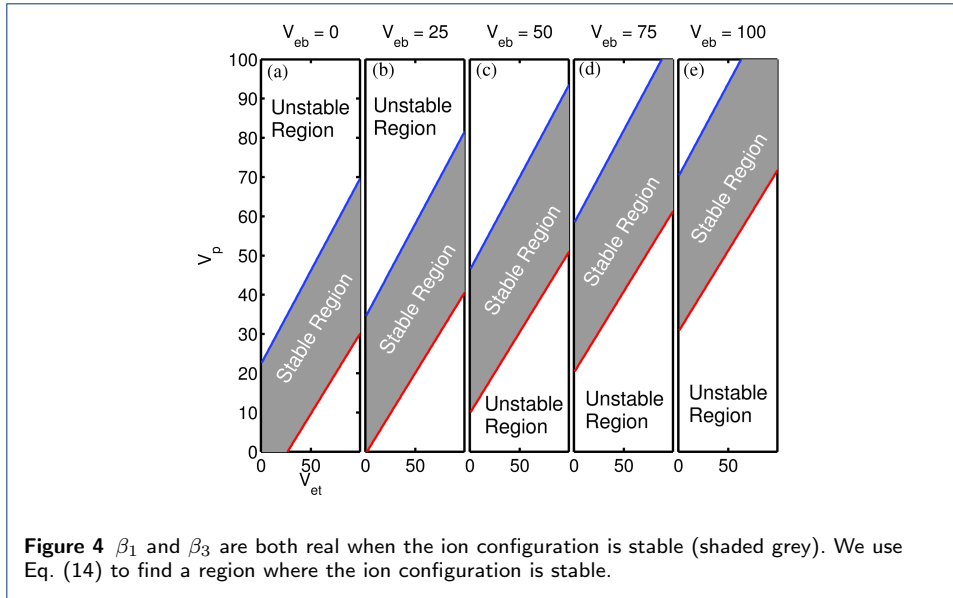
There are two sets of normal modes: eigenvectors of the $N \times N$ matrix K^{33} yield the ‘‘axial’’ modes (those corresponding to motion perpendicular to the crystal plane) and eigenvectors of the $2N \times 2N$ matrix K^{ij} , $i, j \in [1, 2]$, yield the ‘‘planar’’ modes (those corresponding to ion motion in the crystal plane).

4 Results

Now that we have constructed the formal structure to determine the equilibrium positions, phonon eigenvectors, and phonon frequencies, and we have determined the total pseudopotential of the trap, we are ready to solve these systems of equations to determine the expected behavior of the trapped ions. We present several numerical examples to illustrate the equilibrium structure, eigenvalues of the normal modes, and the effective spin-spin interaction J_{mn} for the axial modes with a detuning of the spin-dependent optical dipole force above the axial center-of-mass phonon frequency, ω_{CM} . We use an ytterbium ion with mass $m = 171u$, where u is the atomic mass unit, and a positive charge $q = e$. For the frequency of the RF voltage, we use $\Omega_{RF} = 2\pi \times 35\text{MHz}$ and the amplitude of the potential applied to the RF ring is $V_{o,RF} \approx 500\text{V}$. The DC voltage applied to the RF ring and to the top and bottom electrodes will be $|V_{DC}| \leq 100\text{V}$. We work in a region where the trapped ion configurations are stable. The ion crystal is stable only when both β_1 and β_2 are real and nonzero, as defined in Eq. (14) and this region is shown in Fig. 4, which depends on the voltages applied to the RF ring and to the top and bottom electrodes. We work with ion crystals that contain up to 20 ions.

4.1 Equilibrium configurations

A single ion will sit in the center of the trap. As more ions are added, because the ions repel each other, a ‘‘hard core’’ like structure will form, starting with rings of ions until it becomes energetically more stable to have one ion in the center of the ring, and then additional shells surrounding it, and so on. We find that as we increase the number of ions, the single ring is stable for $N = 3, 4$, and 5. Increasing N further creates more complex structures. We show the common equilibrium configurations for $N = 5, 10, 15, 20$ with DC voltages of $V_r = 46.3\text{V}$ and $V_t = V_b = 50\text{V}$, in Fig. 5. As mentioned above, $N = 5$ is the last configuration that is comprised of a single ring of ions, as depicted in Fig. 5(a). The $N = 5$

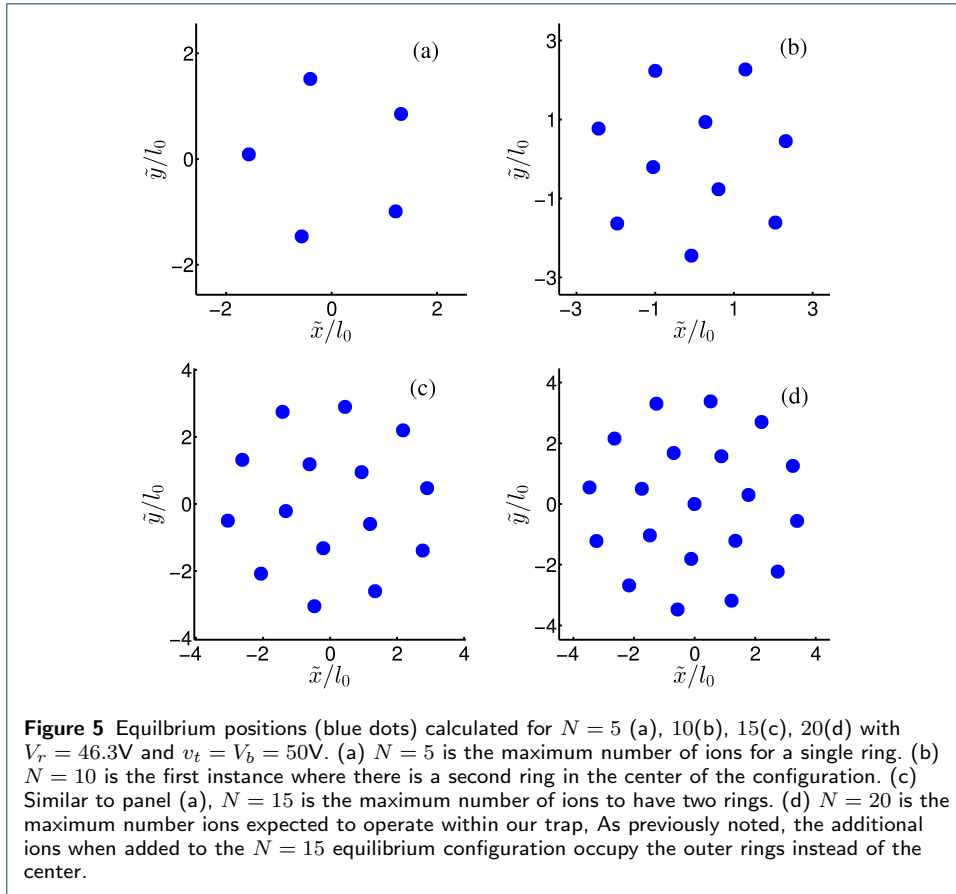


configuration is ideal to use in order to study when periodic boundary conditions are applied to the linear chain, this is due to the configuration being in a single ring. For configurations with $N = 6$ through 8, the additional ions are added to an outer ring. When $N = 9$ the additional ions are added to the center. In Fig. 5(b), $N = 10$ is the first configuration the forms a ring in the center, with three ions. The equilibrium configuration of $N = 15$ is the maximum number to have two rings, as shown in Fig. 5(c). Ion configurations with $N > 15$ have a single ion at the center, as an example of this, we show $N = 20$ in Fig. 5(d). The common configurations for $N > 5$ are nearly formed from triangular lattices (up to nearest neighbor) and this could be used to study frustration in the effective spin models (except, of course, that due to the finite number of ions there are many cases where the coordination number of an interior ion is not equal to 6, as seen in Fig. 5). The shape of all of these clusters for small N agree with those found in Ref. [33], except for $N = 10$, 12, and 14, which have small differences due to the different potential that describes the oblate Paul trap from the potential used in [33].

We next show the dependence of the equilibrium positions on the DC voltages applied to the RF ring and independently applied to the top and bottom electrodes. We fix $N = 5$. As each DC voltage is independently varied, the shape of the equilibrium configuration for $N = 5$ remains the same and only the distances between ions change, as shown in the four cases in Fig. 6.

4.2 Normal modes

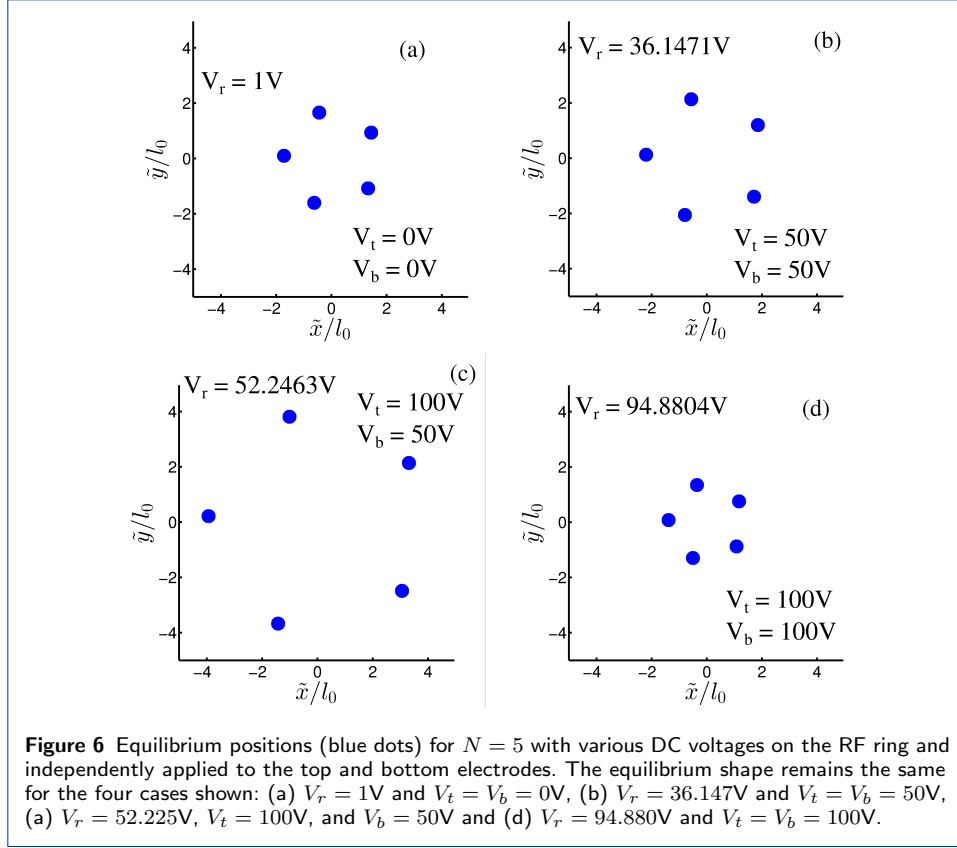
After determining the equilibrium positions, we can find the spring constants and then solve the eigenvalue problem to find the normal modes. Note that due to rotational symmetry, there always is a zero frequency planar mode corresponding to the free rotation of the crystal. In an actual experiment, however, we expect that the rotational symmetry of the trap will be broken by stray fields, the radial optical access tunnels, imperfections in the electrodes, etc., so that mode will be lifted from zero.



We show the eigenvalues of the normal modes for $N = 5$ in Fig. 7. The axial phonon frequencies decrease as the DC voltage on the RF ring increases and the planar phonon frequencies decrease as the DC voltage on the RF ring decreases. For the majority of the combinations of V_t and V_b the axial phonon frequencies lie in a narrow band that is separated from the planar mode frequencies, which also lie in a narrow band. As V_r increases the axial band broadens and eventually overlaps the planar band, which is also broadening. When the axial band has an eigenvalue that goes soft, the system is no longer stable within one plane (which is the equivalent of the zig-zag transition in the linear Paul trap). When $V_t = V_b = 0$ the initial clustering of the axial modes and planar modes is not present, as shown in Fig. 7(a).

4.3 Ising spin-spin interaction

The ions in our trap have two hyperfine states that are separated by a frequency ω_0 . Three laser beams with two beatnotes at frequencies $\omega_0 \pm \mu$ will illuminate the ions, selectively exciting phonon modes as described in [3]. In this case, we choose the laser beams to propagate along the $\pm \hat{e}_3$ direction, as defined in Fig. 1b, such that the laser beams are insensitive to the micromotion which is entirely radial. The phonon modes are excited in a spin-dependent way to generate effective spin-spin



interactions which can be described by the Ising spin coupling matrix, J_{mn}

$$\mathcal{H} = \sum_{mn}^N J_{mn} \sigma_m^z \sigma_n^z, \quad (25)$$

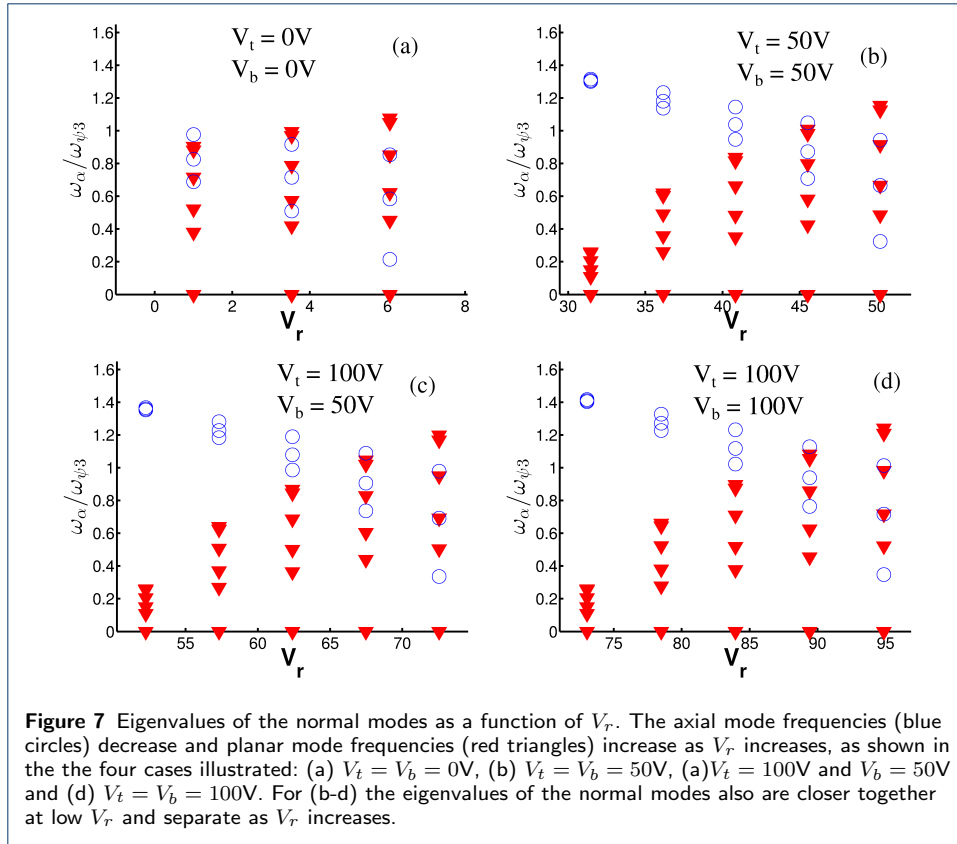
where σ_i^z is the Pauli spin matrix of ion i in the \hat{e}_3 -direction and we have neglected the time-dependent terms of the spin couplings J_{mn} . The explicit formula for J_{mn} is [38]

$$J_{m,n} = J_0 \sum_{\alpha} \frac{b_{m,\alpha}^* b_{n,\alpha}}{(\frac{\mu}{\omega_{CM}})^2 - (\frac{\omega_m}{\omega_{CM}})^2}, \quad (26)$$

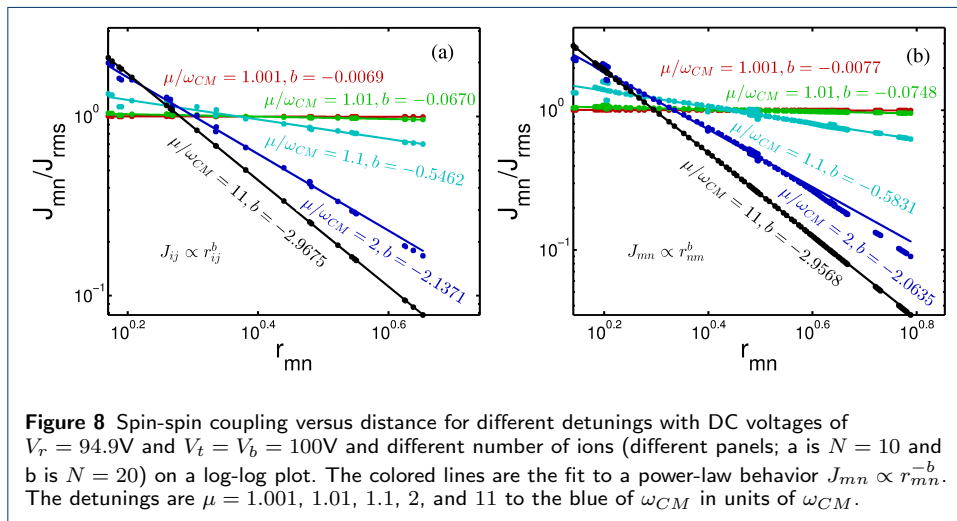
where the coefficient J_0 , depends on the carrier transition Rabi frequency (Ω), the difference in wavevector between the laser beams (δk), the ion mass (m), and the frequency of the center-of-mass mode, (ω_{CM}), and is given by

$$J_0 = \frac{\Omega^2 \hbar (\delta k)^2}{2m\omega_{CM}^2}.$$

It is expected that if one detunes, μ , to be larger than the center-of-mass mode frequency, then one can generate long-range spin-spin couplings that vary as a power law from 0 to 3, as they decay with distance. Hence, we fit the spin-spin couplings to a power law in distance as a function of detuning in Fig. 8 for $N = 10$ and 20.



Note that our system is still rather small, so there are likely to be finite size effects that modify the simple power law behavior.



4.4 Quantum motional effects

The trap could also be used to examine different types of quantum motional effects of ions, similar to the recent work on the Aharonov-Bohm effect [21]. In order to examine such effects, one would need to cool the system to nearly the ground state.

This can be accomplished by including Raman side-band cooling after Doppler cooling the system for all modes except the soft rotational mode, at least when the potential is large enough that the mode frequencies are sizeable. To cool the rotational mode, one would need to add a perturbation to the system that lifts the phonon mode frequency, side-band cool it, and then adiabatically reduce the frequency by removing the perturbation. This procedure will cool off that phonon mode, which can yield quite small quanta in it [21]. Once the system has been prepared in this state, then quantum tunneling effects, or coherent motional effects could be studied in the trap for a range of different ion configurations. It might also be interesting to extend these types of studies to cases where the ions no longer lie completely in one plane, but have deformed into a full three-dimensional structure (as long as the larger micromotion does not cause problems). Finally, many of these ideas would need to be used if one tried to examine time crystals, especially the cooling of the rotational mode to be able to see quantum effects.

5 Conclusion

In this work, we have studied 2D ion crystals in an oblate Paul trap for use in quantum simulations. With this system, one can trap a modest number of ions in 2D planar structures that are likely to be highly frustrated without needing a Penning trap, providing a controlled way to study the onset of frustration effects in quantum simulations. We calculated the equilibrium positions and the phonon frequencies for the proposed oblate Paul trap over its stable region. The equilibrium positions with $N \leq 5$ form a single ring configuration and could potentially be used to study periodic boundary conditions and the Aharonov-Bohm effect when $N = 4$ or 5 (and possibly time crystals). Once $N > 5$, the equilibrium configurations have multiple rings that are nearly formed from triangular lattices. One can generate an effective Ising Hamiltonian by driving axial modes with a spin-dependent optical dipole force. When detuning is to the blue of the axial center-of-mass mode, the spin-spin coupling, J_{mn} , has an approximate power law that is within the expected range of 0 to 3. In the future, as this trap is tested and performs simulations of spin models with ions, the work presented here will be critical to determining the parameters of the Hamiltonian and for selecting the appropriate configurations to use in the different simulations.

Competing interests

The authors declare that they have no competing interests.

Author's contributions

The idea from this work came from Wes Campbell and Jim Freericks. Danilo Dadic and Wes Campbell developed the electric field potentials for the pseudopotential description of the trap as well as designing the trap parameters. Bryce Yoshimura, Marybeth Stork and Jim Freericks performed all of the theoretical calculations. The paper manuscript was first drafted by Bryce Yoshimura and then all authors contributed to revisions.

Acknowledgements

We thank Dr. Philippe Bado, Dr. Mark Dugan and Dr. Christopher Schenck of Translume (Ann Arbor, MI) for valuable discussions. B. Y. acknowledges the Achievement Rewards for College Scientists Foundation for supporting this work. M. S. acknowledges the National Science Foundation under grant number DMR-1004268 for support. J. K. F. and B. Y. acknowledge the National Science Foundation under grant number PHY-1314295 for support. D.D. and W.C.C. acknowledge support from the U.S. Air Force Office of Scientific Research Young Investigator Program under grant number FA9550-13-1-0167 and support from the AFOSR STTR Program. J. K. F. also acknowledges support from the McDevitt bequest at Georgetown University.

Author details

¹Department of Physics, Georgetown University, 37th and O St. NW, 20007, Washington, DC, USA. ²Department of Physics and Astronomy, Washington University, Campus Box 1105, One Brookings Dr., 63130, St. Louis, Missouri, USA. ³ University of California Los Angeles, 475 Portola Plaza, 90095, Los Angeles, CA, USA.

References

- Feynman RP: **Simulating physics with computers.** *Int J Theor Phys* 1982, **21**(6/7): 467–488.
- Friedenauer A, Schmitz H, Glueckert JT, Porras D, Schaetz T: **Simulating a quantum magnet with trapped ions.** *Nature Phys* 2008, **4**(10): 757–761.
- Kim K, Chang M-S, Korenblit S, Islam R, Edwards EE, Freericks JK, Lin G-D, Duan L-M, Monroe C: **Quantum simulation of frustrated Ising spins with trapped ions.** *Nature* 2010, **465**(7268): 590–593.
- Islam R, Edwards EE, Kim K, Korenblit S, Noh C, Carmichael H, Lin G-D, Duan L-M, Wang C-CJ, Freericks JK, Monroe C: **Onset of a Quantum Phase Transition with a Trapped Ion Quantum Simulator.** *Nature Commun* 2011, **2**, 377.
- Islam R, Senko C, Campbell WC, Korenblit S, Smith J, Lee A, Edwards EE, Wang C-CJ, Freericks JK, Monroe C: **Emergence and Frustration of Magnetism with Variable-Range Interactions in a Quantum Simulator.** *Science* 2013, **340**(6132), 583–587.
- Lanyon BP, Hempel C, Nigg D, Müller M, Gerritsma R, Zähringer F, Schindler P, Barreiro JT, Rambach M, Kirchmair G, Hennrich M, Zoller P, Blatt R, Roos CF: **Universal digital quantum simulation with trapped ions.** *Science* 2011, **334**(6052): 57–61.
- Senko C, Smith J, Richerme P, Lee A, Campbell WC, Monroe C: **Coherent imaging spectroscopy of a quantum many-body spin system.** *Science (submitted)* 2014.
- Richerme P, Gong Z-X, Lee A, Senko C, Smith J Foss-Feig M, Michalakakis S, Gorshkov AV, Monroe C: **Non-local propagation of correlations in long-range interacting quantum systems.** *Nature (submitted)* 2014.
- Jurcevic P, Lanyon BP, Hauke P, Hempel C, Zoller P, Blatt R, Roos CF: **Observation of entanglement propagation in a quantum many-body system.** *Nature (submitted)* 2014.
- Porras D, Cirac JI: **Effective quantum spin systems with trapped ions.** *Phys Rev Lett* 2004, **92**(20): 207901.
- Britton JW, Sawyer BC, Keith A, Wang C-CJ, Freericks JK, Uys H, Biercuk MJ, Bollinger JJ: **Engineered two dimensional Ising interactions in a trapped-ion quantum simulator with hundreds of spins.** *Nature* 2012, **484**(7395): 489–492.
- Clark RJ, Lin T, Brown KR, Chuang IL: **A two-dimensional lattice ion trap for quantum simulation.** *J Appl Phys* 2009, **105**(1): 013114.
- Sterling RC, Rattanasonti H, Weidt S, Lake K, Srinivasan P, Webster SC Kraft M, Hensinger WK: **Fabrication and operation of a two-dimensional ion-trap lattice on a high-voltage microchip.** *Nature Commun* 2014, **5**: 3637.
- Chiaverini J, Lybarger WE: **Laserless trapped-ion quantum simulations without spontaneous scattering using microtrap arrays.** *Phys Rev A* 2008, **77**(2): 022324.
- Kumph M, Brownnutt M, Blatt R: **Two-dimensional arrays of radio-frequency ion traps with addressable interactions.** *New J Phys* 2011, **13**: 073043.
- Siverns JD, Weidt S, Lake K, Lekitsch B, Hughes MD, Hensinger WK: **Optimization of two-dimensional ion trap arrays for quantum simulation.** *New J Phys* 2012, **14**: 085009.
- Schmied R, Wesenberg JH, Leibfried D: **Optimal surface-electrode trap lattices for quantum simulation with trapped ions.** *Phys Rev Lett* 2009, **102**(23): 233002.
- Korenblit S, Kafri D, Campbell WC, Islam R, Edwards EE, Gong Z-X, Lin G-D, Duan L-M, Kim J, Kim K, Monroe C: **Quantum simulation of spin models on an arbitrary lattice with trapped ions.** *New J Phys* 2012, **14**: 095024.
- Yoshimura B, Campbell WC, Freericks JK: **Diabatic ramping spectroscopy of many-body excited states for trapped-ion quantum simulators.** *Phys Rev A (submitted)* 2014.
- del Campo A, Rams MM, Zurek WH: **Assisted finite-rate adiabatic passage across a quantum critical point: Exact solution for the quantum Ising model.** *Phys Rev Lett* 2012, **109**(11): 115703.
- Noguchi A, Shikano Y, Toyoda K, Urabe S: **Aharonov–Bohm effect in the tunnelling of a quantum rotor in a linear Paul trap.** *Nature Commun* 2014, **5**: 3868.
- Wilcek F: **Quantum time crystals.** *Phys Rev Lett* 2012, **109**(16): 160401.
- Li T, Gong Z-X, Yin Z-Q, Quan HT, Yin X, Zhang P, Duan L-M, Zhang X: **Space-time crystals of trapped ions.** *Phys Rev Lett* 2012, **109**(16): 163001.
- Itano WM, Bergquist JC, Wineland DJ: **Coulomb Clusters of Ions in a Paul Trap.** *Proceedings of the Workshop on Crystalline Ion Beams*, edited by Hasse R. W., (GSI, Wertheim, 1989).
- Bergquist JC, Wineland DJ, Itano WM, Hemmati H, Daniel HU, Leuchs G: **Energy and Radiative Lifetime of the $Sd^{9}6s^{2} \ ^{2}D_{5/2}$ State in Hg II by Doppler-Free Two-Photon Laser Spectroscopy.** *Phys Rev Lett* 1985, **55**(15): 1567–1570.
- Wineland DJ, Itano WM, Bergquist JC, Hulet RG: **Laser-cooling limits and single-ion spectroscopy.** *Phys Rev A* 1987, **36**(5): 2220–2231.
- Bergquist JC, Hulet RG, Itano W.M, Wineland DJ: **Observation of Quantum Jumps in a Single Atom.** *Phys Rev Lett* 1986, **57**(14): 1699–1702.
- Wineland DJ, Itano WM, Bergquist JC: **Absorption spectroscopy at the limit: detection of a single atom.** *Opt Lett* 1987 **12**(6): 389–391.
- Bergquist JC, Itano WM, Wineland DJ: **Recoilless optical absorption and Doppler sidebands of a single trapped ion.** *Phys Rev A* 1987 **36**(1): 428–431(R).

30. Heinzen DJ, Wineland DJ: **Quantum-limited cooling and detection of radio-frequency oscillations by laser-cooled ions.** *Phys Rev A* 1990, **42**(5): 2977–3004.
31. Block M, Drakoudis A, Leuthner H, Seibert P, Werth G: **Crystalline ion structures in a Paul trap.** *J Phys B* 2000, **33**(11): L375–L382.
32. Schiffer JP: **Phase transitions in anisotropically confined ionic crystals.** *Phys Rev Lett* 1993, **70**(6): 818.
33. Bedanov VM, Peeters FM: **Ordering and phase transitions of charged particles in a classical finite two-dimensional system.** *Phys Rev B* 1994, **49**(4): 2667–2676.
34. Buluta IM, Kitaoka M, Georgescu S, Hasegawa S: **Investigation of planar Coulomb crystals for quantum simulation and computation.** *Phys Rev A* 2008, **77**(6): 062320.
35. Buluta IM, Hasegawa S: **The structure of planar Coulomb crystals in RF traps.** *J Phys B: At. Mol Opt Phys* 2009, **42**(15): 154004.
36. Clossen TLL, Roussel MR: **The flattening phase transition in systems of trapped ions.** *Can J Chem* 2009, **87**(10): 1425–1435.
37. Dehmelt HG: **Radiofrequency spectroscopy of stored ions I: storage.** *Advances in Atomic and Molecular Physics*, edited by Bates DR, Estermann I, (Academic Press, New York, 1967) **3**: 53–72.
38. Zhu S-L, Monroe C, Duan L-M: **Trapped ion quantum computation with transverse phonon modes.** *Phys Rev Lett* 2006, **97**(5): 050505.